5-2019

Development and Testing of Additively Manufactured Aerospike Nozzles for Small Satellite Propulsion

Isaac W. Armstrong
Utah State University

DEVELOPMENT AND TESTING OF ADDITIVELY MANUFACTURED AEROSPIKE NOZZLES FOR SMALL SATELLITE PROPULSION

by

Isaac W. Armstrong

A thesis submitted in partial fulfillment
of the requirements for the degree

of

MASTER OF SCIENCE

in

Aerospace Engineering

Approved:

_____	_____
Stephen Whitmore, Ph.D. Major Professor	David Geller, Ph.D. Committee Member
_____	_____
Douglas Hunsaker, Ph.D. Committee Member	Laurens H. Smith, Ph.D. Interim Vice President for Research and Dean of the School of Graduate Studies

UTAH STATE UNIVERSITY
Logan, Utah

2019

ABSTRACT

Development and Testing of Additively Manufactured Aerospike Nozzles for Small Satellite Propulsion

by

Isaac W. Armstrong, Master of Science

Utah State University, 2019

Major Professor: Dr. Stephen A. Whitmore
Department: Mechanical and Aerospace Engineering

Altitude compensating aerospike nozzles have been built and tested at a small scale, where the benefits of modern 3D-printing technology can be brought to bear. Widespread utility of the aerospike nozzle has been limited by thermal degradation issues, fabrication difficulty, and a lack of experimental data. A need exists for small, reliable propulsion systems to propel small satellites below the NanoSat size of 10kg. In particular, the rise in popularity of CubeSats is flooding orbits with small spacecraft, many of which rely on reaction wheels for limited maneuvering capabilities. Chemical rockets, used to propel many existing spacecraft, see proportionally large gains from small gains in nozzle performance. Aerospike nozzles provide two major advantages of interest over existing state-of-the-art bell nozzles. First, they have superior over-expanded performance that does not lead to normal shockwaves that plague bell nozzles. Second, for in-space vacuum conditions, aerospikes have the potential to be lighter and shorter than bell nozzles with corresponding throat area, exit area, and expansion ratio. Two aerospike nozzles were tested during the course of this thesis testing. Both nozzles had an

exit diameter of 0.5 inches and an expansion ratio of 8.5:1. Utilizing 3D metal printing, one of the nozzles was printed as one piece out of Inconel 718 superalloy. The aerospikes integrated into an existing USU arc-ignited ABS/GOX hybrid motor. Vacuum testing results indicated a specific impulse (I_{SP}) gain of ~6% when using an aerospike nozzle over a corresponding bell nozzle. In testing at higher back pressure, in the over-expanded regime, the aerospike adjusted and functioned as expected, but was outperformed in I_{SP} by a tested cone nozzle. The cone nozzle is believed to have outperformed the aerospike via pressure increase over a normal shockwave, a phenomenon only seen in short nozzles. One test aerospike was survived over 8 seconds of 1 second-pulsed burns, while the printed Inconel aerospike was prematurely affected by thermal degradation. Degradation, likely avoidable, is thought to have been enhanced by the propellant system, support arm design, and choice of printed material. Further testing to determine thermal limits of additively manufactured aerospike designs is deemed necessary.

(134 pages)

PUBLIC ABSTRACT

Development and Testing of Additively Manufactured Aerospike Nozzles for Small Satellite Propulsion

Isaac W. Armstrong

Automatic altitude compensation has been a holy grail of rocket propulsion for decades. Current state-of-the-art bell nozzles see large performance decreases at low altitudes, limiting rocket designs, shrinking payloads, and overall increasing costs. Aerospike nozzles are an old idea from the 1960's that provide superior altitude-compensating performance and enhanced performance in vacuum, but have survivability issues that have stopped their application in satellite propulsion systems. A growing need for CubeSat propulsion systems provides the impetus to study aerospike nozzles in this application. This study built two aerospike nozzles using modern 3D metal printing techniques to test aerospikes at a size small enough to be potentially used on a CubeSat. Results indicated promising in-space performance, but further testing to determine thermal limits is deemed necessary.

ACKNOWLEDGMENTS

Numerous friends and family members have unwaveringly supported me throughout the writing of this thesis, but a few names stand out above the rest.

Dr. Stephen Whitmore, whose unending energy and incredible work ethic has built the USU hybrid rocket program into the accomplished research lab it is today, and who has shown me incredible generosity and guidance during my time at USU and in Huntsville.

Mr. Daniel Cavender, of ER23 of NASA Marshall Space Flight Center, of whom without his support, contacts, and interest this study would have been impossible.

Mr. Terry Zollinger, MAE machinist, who actually did the leg work in machining the test article.

My fellow graduate students, Britany Chamberlain, Mark Heiner, and Spencer Matthias, who were patient with me and let me learn and assist in their projects.

And finally, Dr. William David Armstrong, who made engineering fun in the first place.

Isaac W. Armstrong

CONTENTS

Page

LIST OF TABLES

Table Page

LIST OF FIGURES

ACRONYMS

ABS	Acrylonitrile Butadiene Styrene
CAD	Computer Aided Design
CAN	Cooperative Agreement Notice
CEA	Chemical Equilibrium with Applications
CFD	Computational Fluid Dynamics
CNC	Computerized Numerical Control
DAQ	Data Acquisition Unit
GH2	Gaseous Hydrogen
GN2	Gaseous Nitrogen
GOX	Gaseous Oxygen
HIPS	High Impact Polystyrene
HTPB	Hydroxyl-Terminated Polybutadiene
ICBM	Inter-Continental Ballistic Missile
ISP	Specific Impulse
LOX	Liquid Oxygen
MSFC	Marshall Space Flight Center
N2O	Nitrous Oxide
NanoSat	Nano-Satellite
NASA	National Aeronautics and Space Administration
NPR	Nozzle Pressure Ratio
O/F	Oxidizer-to-Fuel Ratio
P&ID	Piping and Instrumentation Diagram
RTV	Room-Temperature-Vulcanizing
USU	Utah State University
VI	Virtual Instrument

NOMENCLATURE

$\dot{m}_{exit}$	Nozzle Exit Mass Flow Rate
$\dot{m}_{fuel}$	Fuel Mass Flow Rate
$\dot{m}_{ox}$	Oxidizer Mass Flow Rate
$\dot{m}_{total}$	Total Mass Flow Rate
$\dot{r}_{hybrid}$	Hybrid Rocket Fuel Regression Rate
$\dot{r}_{solid}$	Solid Rocket Fuel Regression Rate
$h_{convection}$	Convective Heat Transfer Coefficient
h_v	Enthalpy of Formation
A_{exit}	Cross-Sectional Nozzle Exit Area
A_t	Cross-Sectional Nozzle Throat Area
C^*	Characteristic Velocity
C_d	Venturi Discharge Coefficient
C_f	Skin Friction Coefficient
D_0	Fuel Port Diameter at Start of Burn
D_H	Hydraulic Diameter
D_{in}	Inner Annulus Diameter
D_{out}	Outer Annulus Diameter
I_{SP}	Specific Impulse
$K\_$	Negative Sloped Characteristic Line Constant
M_{exit}	Nozzle Exit Mach Number
$\|\|N\|\|$	Measurement Variance
$\|\|P_{00}\|\|$	Measured Pressure Variance
O/F_{mean}	Mean Oxidizer-to-Fuel Ratio
P_0	Combustion Chamber Pressure, Stagnation Pressure
Re_D	Dimensionless Reynolds Number, Based on Diameter
R_g	Specific Gas Constant
T_0	Stagnation Temperature
V_{exit}	Fluid Velocity at Nozzle Exit
c_p	Specific Heat Capacity
g_0	Acceleration due to Earth's Gravity
n^*	Combustion Efficiency
p_∞	Ambient Pressure
p_{exit}	Fluid Pressure at Nozzle Exit
λ_d	Nozzle Discharge Coefficient
$\tau_{combustor}$	Combustion Chamber Depressurization Time
υ_{conv}	Time-Domain Convolution Function
υ_{exit}	Vertical Component of Fluid Velocity at Nozzle Exit
ω_n	Natural Frequency of a Second Order Dynamic System
μ	Dynamic Viscosity of a Fluid
ϒ	Frequency-Domain Convolution Function
ς	Damping Ratio of a Second Order Dynamic System
A	Cross-sectional Nozzle Area
B	Blowing Coefficient
D	Diameter
E	Error Function
F	Thrust Force
G	Mass Flux

I	Impulse
J	Cost Functional
L	Motor Length
M	Dimensionless Mach Number
O/F	Oxidizer-to-Fuel Ratio
P	Static Pressure
Pr	Dimensionless Prandtl Number
R	Radial Coordinate of Nozzle Contour
St	Dimensionless Stanton Number
T	Static Temperature
V	Fluid Velocity
Vol	Volume
c	Speed of Sound
dA	Infinitesimal Change in Cross-Sectional Area
dV	Infinitesimal Change in Fluid Velocity
i	Complex Constant, $(-1)^{1/2}$
t	Time Variable
x	Longitudinal Nozzle Coordinate
Δh_{flame}	Change in Enthalpy of Motor Chamber Gas During Combustion
ΔM_{fuel}	Fuel Mass Consumed During Burn
A	Thermal Absorptivity
γ	Ratio of Specific Heats
η	Noise Function
θ	Angle to Central Axis of Nozzle
ξ	Polytropic Exponent
ϵ	Thermal Emissivity
ρ	Fluid Density
σ	Stefan-Boltzmann Constant
υ	Vertical Component of Fluid Velocity
ω	Frequency of a Pressure Wave

CHAPTER I

INTRODUCTION

Aerospike nozzles are an old idea in rocketry that have never quite found their mission. While theoretically holding merit over current state-of-the-art rocket nozzles, lack of flight test data and a need for better materials has held back utilization of aerospike nozzles. This thesis proposes to revisit the geometric design of the aerospike with new materials manufacturing that enables a smaller scale than tested previously. Rocket propulsion small enough to propel a CubeSat, which is required to weigh under 3 lbs., is a growing area of research interest. The potential gains of an aerospike nozzle would apply well to this scenario if a feasible design can be constructed. Experimental testing conducted for this study is intended to be a starting point for aerospikes in the CubeSat propulsion application and provide some of the first experimental data at this scale. The following sections of the introduction outline this research motivation.

1.1 Chemical Rocket Propulsion

Chemical propulsion systems are a critical component of many space vehicles, and their development was one of the greatest achievements of humankind's extraordinary technological surge in the 20th century. Building off the study of fluid dynamics, early designs were pioneered in the late 1800's, but the true breakthroughs came with wartime inventions in World War II. Offering significantly greater thrust, capable of propelling airplanes to higher speeds than had been previously capable with piston engine aircraft, the development of the jet engine was a natural military choice and was independently conceived of in both wartime Britain and Germany. The Germans also

applied rockets, a centuries-old weapon, to propulsion of military planes and missiles. Although these innovations failed to make a serious impact on the war, their further development in the famed “space race” of the Cold War directly led to our modern world of interconnected continents and near-instant satellite communications. [1]

Although similar conceptually, rocket propulsion fundamentally differs from jet propulsion in how the propulsion system harnesses a combustion oxidizer. The combustion reaction that supplies the chemical propulsion system’s source of energy requires an initial input of heat in the presence of fuel and a chemical oxidizer in order to be initiated. The goal of this process is the sustained production of heat, and as an example the exothermic combustion of hydrogen and oxygen is shown below in Fig. 1.1. [2]. In a rocket, fuel and oxidizer are stored on board as propellants, with an ignition system providing the initial heat input required to start the chemical reaction. Jet engines instead ingest atmospheric air, which is around 21% usable oxidizer, and pressurize it to high enough levels to sustain combustion upon ignition. Once started, the compressor that provides air pressurization can be powered from the fuel’s combustion by harnessing a percentage of the energy generated with a turbine. Both systems have their advantages, and their strengths are reflected in the vehicles that utilize them. Despite added complexity, jet engines can be made very efficient with extraordinarily high fuel-to-air ratios, making them the system of choice for jet airliners [3]. A rocket must always carry the oxidizer with it, which hurts performance through added weight, but in the vacuum of space this becomes necessary as jet engines cannot operate. Capable of extremely high thrust, rocket propulsion has powered the vast majority of in-space vehicles, and space-launch vehicles are universally rocket powered. To date, every man-made satellite has

been put into orbit on the back of a chemical rocket. [3]

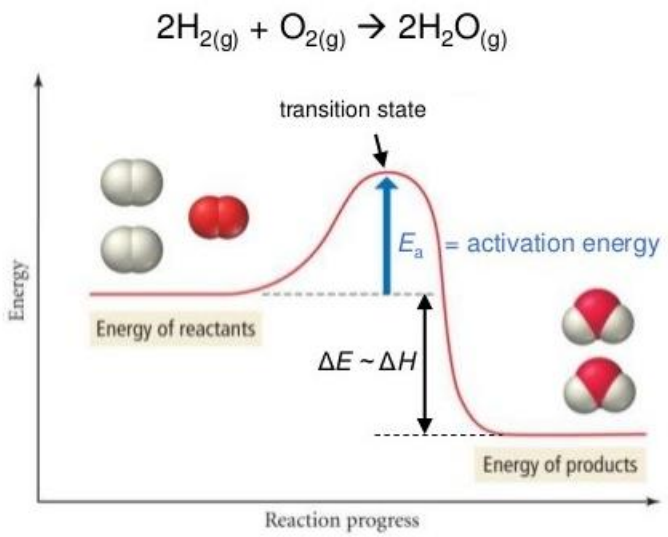

Figure 1.1. Activation energy plot and combustion reaction. [3]

At its simplest, a propulsion rocket's purpose can be boiled down to providing a force, thrust, to a vehicle with the purpose of propelling that vehicle. However, a propulsion rocket must generate this thrust without hampering other aspects of the vehicle's mission. For a launch vehicle, overcoming the tremendous pull of gravity means the ability to shed weight quickly is paramount, and therefore volumetrically efficient solid fueled "booster" rockets are often utilized. An ICBM or other endo-atmospheric rockets will experience drag throughout the entirety of their flight, and propulsion designs must take this into account. In orbit, neither drag nor escaping gravitational pull are of concern, and therefore low thrust schemes such as electrical propulsion become competitive.

Chemical propulsion systems produce thrust through two fundamental mechanisms, the ejected momentum of fluid particles and a net pressure force [1]. This is described in the conventional 1-dimensional rocket thrust equation:

$$F = \dot{m}_{exit} V_{exit} + (p_{exit} A_{exit} - p_{\infty} A_{exit}) \quad (1.1)$$
$$= F_{Momentum} + F_{Pressure}$$

where $\dot{m}_{exit}$ is the mass flow rate of gas out the exit of the motor, V_{exit} is the exit velocity of those gas particles, p_{exit} is the fluid pressure of the exit gas, p_{∞} is the fluid pressure of the surrounding, "ambient" gas, and A_{exit} is the area of the exit plane of the engine. [1] Although simplified by neglecting sources of losses and assuming steady, inviscid flow that only varies down the length of the motor, this expression provides valuable insight into the source of a rocket's thrust. The accompanying geometry of a conventional rocket bell nozzle is illustrated in Fig. 1.2.

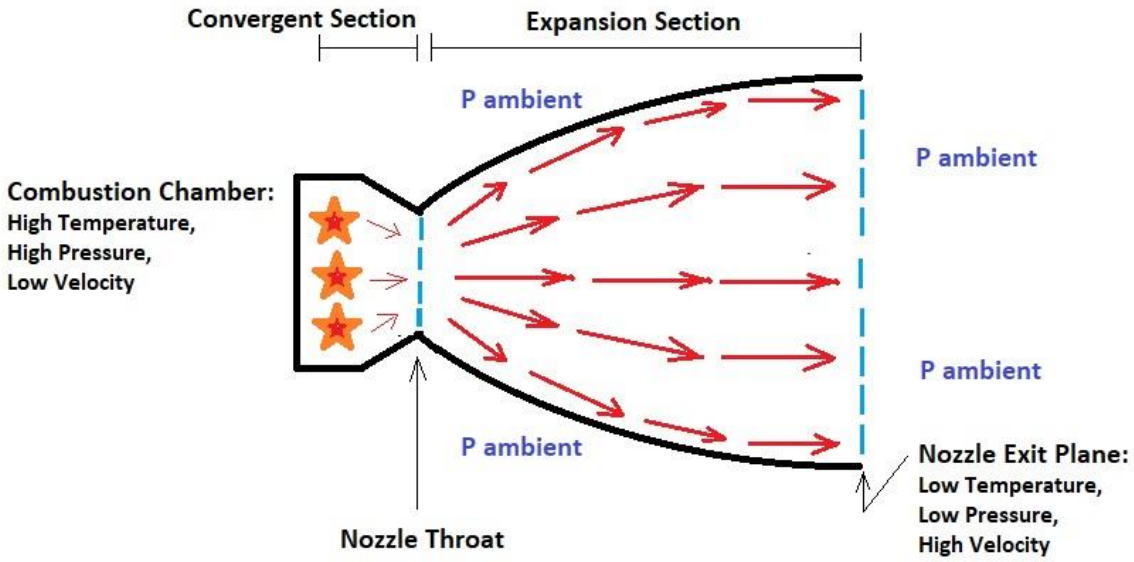

Figure 1.2. Diagram of fluid flow in a bell nozzle.

Fuel combustion in the combustion chamber creates high temperature gas at high pressure, which in a rocket system is immediately channeled into a rocket nozzle. To understand why the constrictive nozzle throat is necessary requires description of a non-dimensionless quantity known as the Mach number (M), which is defined as the ratio of a

fluid's velocity (V) compared to the speed of sound (c) in that fluid [1]:

$$M = \frac{V}{\sqrt{TR_g\gamma}} = \frac{V}{c} \tag{1.2}$$

Sonic flow (M=1) is attained at the nozzle throat by shrinking the cross-sectional area until the gas speed equals the speed of sound in the gas. As discovered by Swedish engineer Gustaf de Laval in the late 1800's, to further accelerate the flow the area must expand again, a seemingly counter-intuitive phenomenon [3]. Following a formulation that begins with the conservation of energy, momentum, and mass in a closed fluid tube, a description of the differential relation between fluid velocity (V) and motor cross-sectional area (A) can be written, using similar assumptions as Eq. (1.1):

$$\frac{dV}{dA} = \frac{1}{(M^2 - 1)}\rho\frac{V^2}{A} \tag{1.3}$$

with ρ being local fluid density and M the aforementioned fluid Mach number. Since V, A, and ρ are by necessity positive values, it is seen that the derivative $\frac{dV}{dA}$ is negative for Mach numbers less than unity and positive for Mach numbers greater than unity. Therefore, shrinking cross-sectional area ($-dA$) to increase velocity flow only works at subsonic speeds (M <1) when the right hand side of Eq. (1.3) is negative, and to further accelerate the flow past sonic velocity the area must widen again [1]. All functional rocket nozzles produce sonic flow at a constricted throat. If the fluid flow is indeed at sonic velocity, the flow is described as "choked", where the maximum mass flow rate has been achieved for upstream conditions, an important consideration when designing a rocket motor [1].

The rocket nozzle's expansion section then further accelerates the flow, converting the internal energy of the gaseous combustion products into kinetic energy. A

high velocity, low pressure flow emerges from the nozzle, with particles directed into a useful direction. Conservation of momentum and Newtonian physics dictate that the momentum ejected out the rear of a propulsion system will cause a forward thrust force, and shows up as the first product in the rocket thrust equation, Eq. (1.1). The velocity increase is largely dependent on the nozzle's expansion ratio, the ratio of exit area to inlet area, a measure of the nozzles ability to depressurize and speed up the supersonic flow particles [1].

No less significant is the pressure exerted on the interior walls of the nozzle, the second term of thrust in Eq. (1.1). Since earthly atmospheric conditions are at far less pressure than generated by chemical propellants, the nozzle feels less pressure on its atmospheric sides, producing a net force in the same direction as the momentum thrust force. This effect lessens as the pressure in the motor drops towards the rear of the nozzle, until ideally the exit pressure of the rocket flow matches the surrounding atmospheric pressure [1].

As mentioned above, thrust is not the whole picture when quantifying rocket motor properties, and to simplify comparison between rocket systems engineers often use a quantity known as specific impulse (I_{SP}) [3]. Impulse (I) is a physical parameter defined as the product of force (F) and time ($t_2 - t_1$), shown in Eq. (1.4).

$$I = \int_{t_1}^{t_2} F \, dt \tag{1.4}$$

An impulse imparted onto an object will produce an equivalent change in that object's momentum, and a rocket will continually produce an impulse for the duration of its burn length. However, as mentioned above, system weight is of critical concern. Specific impulse takes this into account by dividing by the motor's mass flow, and in the U.S. is

commonly reported in units of time [3]:

$$I_{SP_{instantaneous}} = \frac{F}{g_0 \dot{m}_{exit}} \tag{1.5}$$

$$I_{SP} = \frac{\int_{t_1}^{t_2} F(t)\, dt}{g_0 \int_{t_1}^{t_2} \dot{m}_{exit}(t) dt} \tag{1.6}$$

In both equations it is necessary to divide by the acceleration due to gravity, g_0. Mean I_{SP}, shown in Eq. (1.6), is generally more useful than $I_{SP_{instantaneous}}$ because specific impulse can vary significantly over a rocket's burn time. Specific impulse is useful as a comparator because it takes into account a rocket system's combustion properties, fuel utilization, nozzle characteristics, and fluid losses in one parameter. As an example to further illustrate the concept, consider an analogy where thrust is compared to a car engine's horsepower. When pulling heavy loads, a high horsepower vehicle such as a pickup truck is desirable, even though its gas mileage (comparable to specific impulse) may suffer. When expected to transport a small load regularly, gas mileage becomes a more important factor, and small commuter cars often lack high engine horsepower. For a non-rigorous comparison, thrust and specific impulse provide a similar characterization for rockets. The five F-1 engines that propelled the first stage of NASA moon missions in the 1960's needed incredibly large thrust to get the fully loaded weight of the Saturn V off the ground, and each had a thrust of 1.5 million pounds with an I_{SP} of 263 seconds. The upper stage J-2 engines, however, needed far less thrust as they would only fire high in the atmosphere, and generated a thrust of 232,000 pounds with an I_{SP} of 420 seconds. In summary, although possessing different units and representing different physical parameters, thrust and I_{SP} are both needed to characterize the performance of a chemical rocket much as in the way engine power and gas mileage apply to a car.

Thrust and I_{SP} are directly linked, but not all motor improvements increase both of these performance parameters. The molecular weight of propellants, essentially a user-determined choice in rocket motor design, is a primary contributor to performance. Lighter propellants, such as hydrogen, require less energy to accelerate, which results in a high I_{SP}. Conversely, the low mass of propellant leaving the nozzle reduces momentum thrust, so a tradeoff of sorts exists when choosing a propellant and its corresponding molecular weight. Past the nozzle throat however, improvements to reduce losses improve both thrust and I_{SP}. Nozzle losses will negatively impact fluid particle velocity, hampering thrust, and subsequently cutting into specific impulse. Therefore, the nozzle is one of the most critical areas for a chemical rocket propulsion, and improvements in nozzle performance have benefits across the entire vehicle [4].

1.2 Rocket Nozzle Performance

Bell nozzles are a mature technology and well understood. Test data is extensive as the vast majority of historical rockets have been equipped with bell nozzles or closely related conical nozzles. The nozzle was originally introduced in the late 1800's by Gustaf de Laval, and its subsequent success in Robert Goddard's groundbreaking rocketry has ensured its usage to this day. As of 2018, every orbital launch vehicle, regardless of country of origin or size, has used a de Laval style bell nozzle [4].

Numerous analytical tools exist to simulate bell nozzle flow. Building off of basic conservation laws of energy, continuity, and momentum, the method of characteristics developed in the 1960's is a common technique used to design bell nozzles. The method of characteristics is a numerical technique that uses characteristic lines, or fluid lines

along which Mach number remains constant, to determine properties of downstream particles. Details of this method are common classroom material; at Utah State University the text used is Modern Compressible Flow by John D. Anderson [1]. Additionally, newer technology such as CFD programs can handle compressible flow problems such as this one. A discussion of the method of characteristics model developed to verify the results of this experimental study will be outlined later in Section 3.4.

Atmospheric flight intrinsically presents a pressure thrust generation problem due to the dependence of atmospheric pressure upon altitude. The pressure drop due to fluid expansion in a nozzle is directly set by propellant properties and by the nozzle's physical geometry [1]. That is to say, for a chosen rocket propellant and rocket nozzle, the flow will always expand to the same exit pressure in vacuum conditions. The atmosphere is, of course, constantly changing with weather patterns, but in general atmospheric pressure decreases with increasing altitude, eventually opening up to the vacuum of space. Therefore, a fixed-geometry nozzle will only expand ideally to a specific ambient pressure, which only matches atmospheric conditions at one specific altitude. This altitude is referred to as the design altitude, where a rocket motor will be functioning at peak performance [1]. A vehicle will want to maximize time spent at the design altitude, but it is important for many propulsion systems to function in off-design conditions. In particular, launch vehicles ascend through a particularly severe atmospheric pressure decrease [1].

Off-design exit pressures experienced at most altitudes adversely affect conventional bell nozzles particularly severely when the nozzle is over-expanded. An over-expanded nozzle has an exit pressure that is less than the surrounding atmosphere,

and a local negative pressure gradient develops [4]. The atmospheric pressure is physically pushing back into the nozzle in this case, and backflow occurs. Backflow is particularly damaging to a supersonic flow field because of the formation of shockwaves, walls of pressure that severely inhibit fluid movement [1]. An entrained shockwave can vary in strength and location in a nozzle, and the shock's presence is often visible outside the nozzle exit via a chain of generated oblique shocks- commonly called shock diamonds. The motor experiences a drastic reduction in thrust, which can be catastrophic. The opposite effect, under-expansion, is somewhat less harmful. Here the nozzle has not allowed the flow to expand sufficiently at its exit, and high pressure gas pushes out radially into the surrounding atmosphere, at the cost of some performance. Both conditions are contrasted with the design condition in Fig. 1.3.

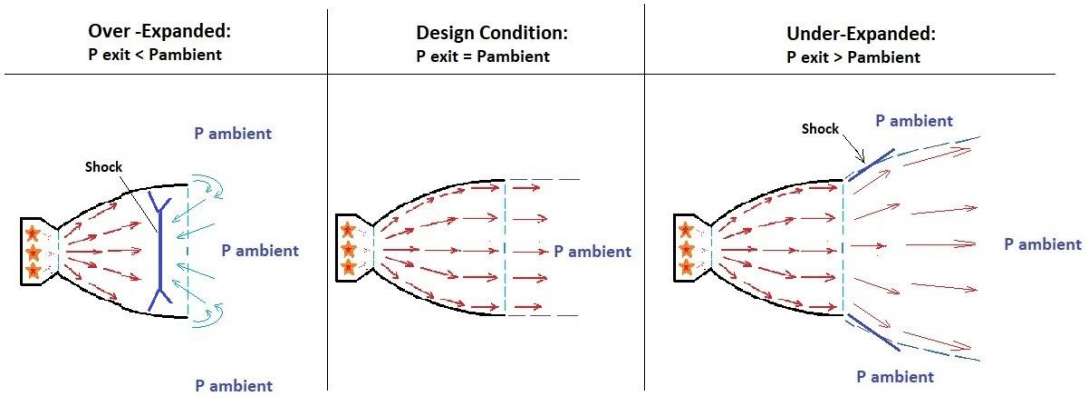

Figure 1.3. Diagram of pressure regimes in a bell nozzle.

Although inefficient, the under-expanded nozzle condition does not result in the high-loss interior shockwaves of the over-expanded nozzle condition. Therefore, from a design perspective, it is often advantageous to specify the design altitude as close to the launch altitude. As the vehicle climbs, ambient pressure reduces and the nozzle slips into an increasingly under-expanded state, but starting at the design altitude ensures that the

motor never experiences crippling over-expanded shockwaves. For instance, the space shuttle main engines, which burned for eight minutes to place it in orbit at an altitude of 250 miles, had a design altitude of 11 miles [5]. At launch, near sea level, the nozzle was slightly over-expanded, but within half a minute the engines were safely into the under-expanded regime.

It is apparent that active avoidance of operating in the over-expanded regime is a far from ideal scenario that restricts vehicle design, and many possible improvements have been considered over the years. A variable geometry "telescoping" nozzle configuration that could change its length and expansion ratio at will would be ideal, but current material limits hamstring the feasibility of such schemes [3]. Maintaining internal pressure while having nozzle components shift over each other to adopt a new geometry is exceptionally difficult, especially with weight considerations limiting the complexity of any such systems [4].

In the 1960's engineers at Rocketdyne introduced a novel possible answer to the variable-geometry altitude-compensation problem, which they coined as the aerospike nozzle [6]. Resembling an inside-out bell nozzle, Fig. 14 shows the design condition, over-expansion, and under-expansion regimes of the aerospike nozzle. Aerospike nozzles expand supersonic fluid like a bell nozzle, but past the sonic throat the flow is contained by atmospheric pressure on one boundary. It is this feature that allows for the aerospike nozzle to be inherently altitude compensating, as the plume will always adapt to current atmospheric pressure [7]. At the aerospike design condition, the plume exits the nozzle uniformly and peak efficiency is achieved. However, it is in the off-design conditions that the aerospike nozzle truly shines. For under-expanded conditions at altitudes greater than

the design condition, the plume pushes out against the surrounding atmosphere for a minor loss in efficiency similar to the bell nozzle. But at lower altitudes, the over-expanded aerospike plume constricts without the crippling lack of thrust that develops in a bell nozzle [7]. Instead, a chain of compression and expansion waves develop inside the aerospike plume, which do not disrupt the fluid flow with nearly as large of an entropy increase as that associated with normal shockwaves seen in bell nozzles [3].

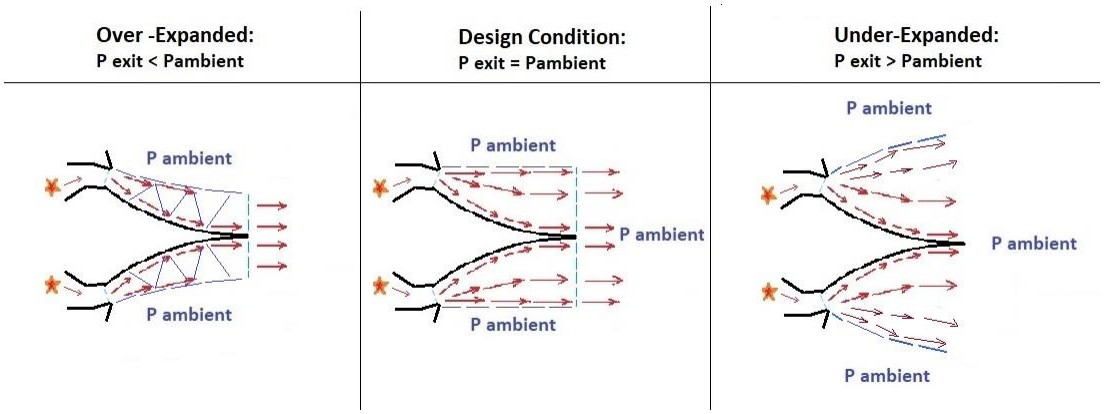

Figure 1.4. Diagram of pressure regimes in an aerospike nozzle.

In addition to their superior over-expanded performance, aerospike nozzles provide several other advantages. Since pressure steeply drops off in a second-order decay as fluid expands down the spike contour, the majority of pressure thrust is being produced in the upstream half of the nozzle [7]. An aerospike can therefore be shortened to resemble a truncated cone without losing significant performance. Truncating can significantly reduce weight and allows a higher performance nozzle for similar length when compared to a bell [8]. The performance loss from the recirculation region that forms behind the nozzle truncation can also be mitigated by the ejection of a central gas flow to build back pressure. A truncated linear aerospike, used on the NASA X-33, is shown in Fig. 1.5. Aerospike nozzles also have the potential for thrust vectoring directly

from the nozzle without gimbals [7]. This idea has been explored for bell nozzles, but the vectoring flows introduce shockwaves inside the bell that produce a loss of thrust. The aerospike is less hampered by these shockwaves as well because of the adaptive nature of their fluid boundary with the atmosphere [7].

Figure 1.5. Images of successfully tested aerospike nozzles.

The previous advantages listed are significant for endo-atmospheric flight, but a large focus of this research will be for in-space applications, where their altitude compensation features are irrelevant. Previous work indicates significant in-space thrust advantage when compared to a conventional nozzle of the same size and weight. Testing conducted by T. Bui et al. in 2005 concluded that switching to a comparable aerospike nozzle can result in mass savings of up to 8-9% [9]. On a spacecraft where every last gram translates as money spent to get into orbit, the aerospike becomes attractive if it's disadvantages can be overcome (to be discussed in chapter II).

1.3 Application of Aerospike Nozzles to Small Spacecraft

Small spacecraft propulsion is a growing field largely due to the popularity of CubeSats. Since their introduction in 1999, CubeSats have standardized experimental

orbital packages. Falling into the category of nano-satellites (NanoSats) at under 10 kg, part of the standard is a maximum weight of 1.33 kg (3 lbs.) for a 1U CubeSat. This standardization has drastically lowered the costs of such systems and their launches. As a result, their popularity has soared and by 2017 over 650 have been launched [10]. Many of these CubeSats come from institutions with small budget constraints and have little control over their destination orbits. Cost saving solutions such as ride sharing and low-cost momentum wheels have sufficed so far, but greatly limit where a small satellite can place itself in orbit. The lack of a sophisticated, on-board propulsion system not only limits mission capability, but also adds to the growing orbital debris problem. A 2014 study by Lewis et al. predicts up to 10% of potential orbit collision conjunctions will involve a CubeSat, a number only expected to grow [11]. Fig 1.6 illustrates this growing popularity by showing CubeSat launches per year since their introduction [10].

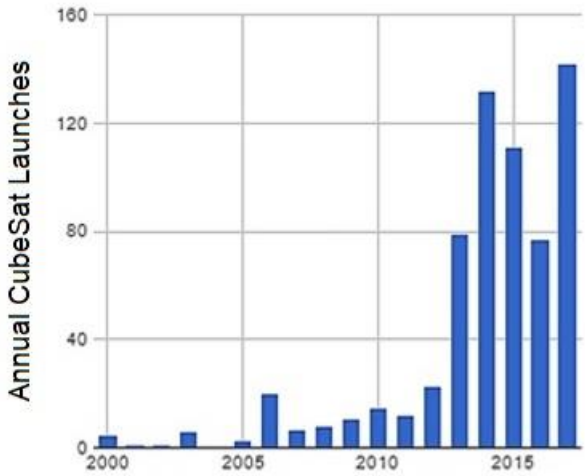

Figure 1.6. Increase in yearly CubeSat launches, 2000-2018. [10]

1.4 Statement of Thesis

This study seeks to fabricate an aerospike nozzle using new manufacturing

methods, namely 3D printing. The aerospike will integrate into an existing Utah State University (USU) arc-ignited ABS/GOX hybrid motor sized for the NanoSat level. Previous aerospike testing in literature has been done at larger scale using conventional fabrication methods, and this study seeks to provide aerospike hot fire data for an expansion ratio of 8.5 in both over-expanded and under-expanded pressure regimes. Testing of cone nozzles, which perform to within 98% of bell nozzle performance [3], will be contrasted with aerospike results in the two regimes to see if changes occur in nozzle survivability and specific impulse of the hybrid motor. The aerospike is hypothesized to have superior I_{SP} performance in both pressure regimes. Potentially destructive shockwave behavior is expected to be seen in the cone nozzle in the over-expanded regime. Durability of aerospike nozzles is explored through the use of new construction techniques.

CHAPTER II

OVERVIEW OF PREVIOUS WORK

2.1 Thermal Degradation of Aerospike Nozzles

The need for small effective space propulsion could potentially be addressed in part by aerospike nozzles if further work can be done to address their primary disadvantage of thermal degradation [7]. The cantilevered central structure of an aerospike changes the nozzle throat profile from a circular hole to an annulus. A rough cut at a thermal heating model that illustrates the fundamental thermal weakness of the aerospike can be shown using established skin-friction models for pipes [12]:

$$C_{f_{laminar}} = \frac{16}{Re_D} \quad (Laminar, Re_D < 2000) \tag{2.1}$$

$$C_{f_{turbulent}} = \frac{0.0791}{{Re_D}^{0.25}} \quad (Turbulent, Re_D \geq 2000) \tag{2.2}$$

where C_f is a non-dimensionalized coefficient that captures the relative strength of viscous skin friction in a flow. Taking note that the Reynold's number Re_D, a dimensionless flow parameter defined as the ratio of inertial forces to viscous forces in a fluid, is in the denominator for both laminar and turbulent flow regimes, examine its mathematical definition as given in Eq. (2.3). Directly dependent on pipe diameter, to calculate flow through non-circular pipes a parameter known as hydraulic diameter, D_H, is commonly used. This parameter is shown in Eq. (2.4) for the geometry of an annulus with outer diameter D_{out}, inner diameter D_{in}, and cross-sectional area at the nozzle throat of A_t. μ is the fluid's dynamic viscosity, which along with the other fluid properties will not change Re_D when comparing the flow between a bell nozzle's circular throat and an aerospike's annulus [12].

$$Re_D = \frac{\rho * V * D_H}{\mu} \tag{2.3}$$

$$D_H = \frac{4 * A_t}{Perimeter} = 4 * \frac{4 * \frac{\pi\left({D_{out}}^2 - {D_{in}}^2\right)}{4}}{\pi * (D_{out} + D_{in})} \tag{2.4}$$

$$= D_{out} - D_{in}$$

Hydraulic diameter for an annulus is smaller by D_{in} than a corresponding circular diameter for the equivalent throat area. Thus, the change in throat geometry by switching to an aerospike will result in a lower flow Re_D. For laminar, transitional and turbulent flow regimes at the throat, the skin friction coefficient C_f of Eqs. (2.1) and (2.2) will be larger with an aerospike's annular geometry. As an estimate where the annulus's inner diameter D_{in} is 98% of the outer diameter, matching the physical aerospike geometry used later in the experimental study, C_f rises by a factor of 1.7 in laminar flow, which fundamentally alters heating in the nozzle. Although the effect is lessened in turbulent flow, 1-dimensional nozzle flow models often assume laminar flow for a rocket nozzle and the flow is often characterized as such. The significance in the rise of C_f to heating is illustrated using the Reynolds-Colburn analogy, which is proven to hold well for gaseous flows without form drag [12]. The analogy utilizes several more dimensionless parameters, and is outlined below:

$$St = \frac{h_{convection}}{\rho * c_p * V} \tag{2.5}$$

$$St \approx \frac{C_f}{2 * \mathrm{Pr}^{\frac{2}{3}}} \; (0.6 < Pr < 5) \tag{2.6}$$

Stanton number, St, defined as the ratio of heat transferred to a fluid versus the thermal capacity of that fluid ($\rho * c_p * V$), is directly proportional to the convective heat transfer coefficient, $h_{convection}$. By taking note of the similarity of momentum and heat flux, Eq. (2.6) is a simplified assumption that exists in various forms across different fluid regimes. This particular form assumes a Prandtl number, Pr, greater than 0.6. Pr is a fluid parameter that will not change across different geometries, but may be lower than the range specified above, leading to a slightly different formulation of Eq. (2.6) [3]. The general form of the analogy remains similar, however, and for demonstration purposes shows the link between skin friction and convective heating. Following the above equations, we see that convective heating is substantially enhanced in an aerospike nozzle. Via the change to annular hydraulic diameter, an aerospike nozzle experiencing laminar flow will see a roughly 1.7 multiplication factor in skin friction, Stanton number, and ultimately the convective heat transfer coefficient.

Although adapted from pipe-flow models through various assumptions, the conclusion of the above convective heating calculation has important ramifications for the feasibility of aerospikes as a nozzle technology. The heating problem with aerospikes goes beyond the increase in convective heat transfer rate as the unique cantilevered geometry creates several thermal problems as well. Various schemes exist for cooling a bell nozzle, where ample space is available on the outside of the bell to run cold fluid to counteract the extreme heat experienced near the nozzle throat. An aerospike simply doesn't have as much geometric space to cool the central spike down, as coolant channels would need access through the central spike's support structures. These support structures, shown in Fig. 2.1, are unnecessary in a bell nozzle, and further exacerbate the

convective heating issue by creating stagnation in the flow.

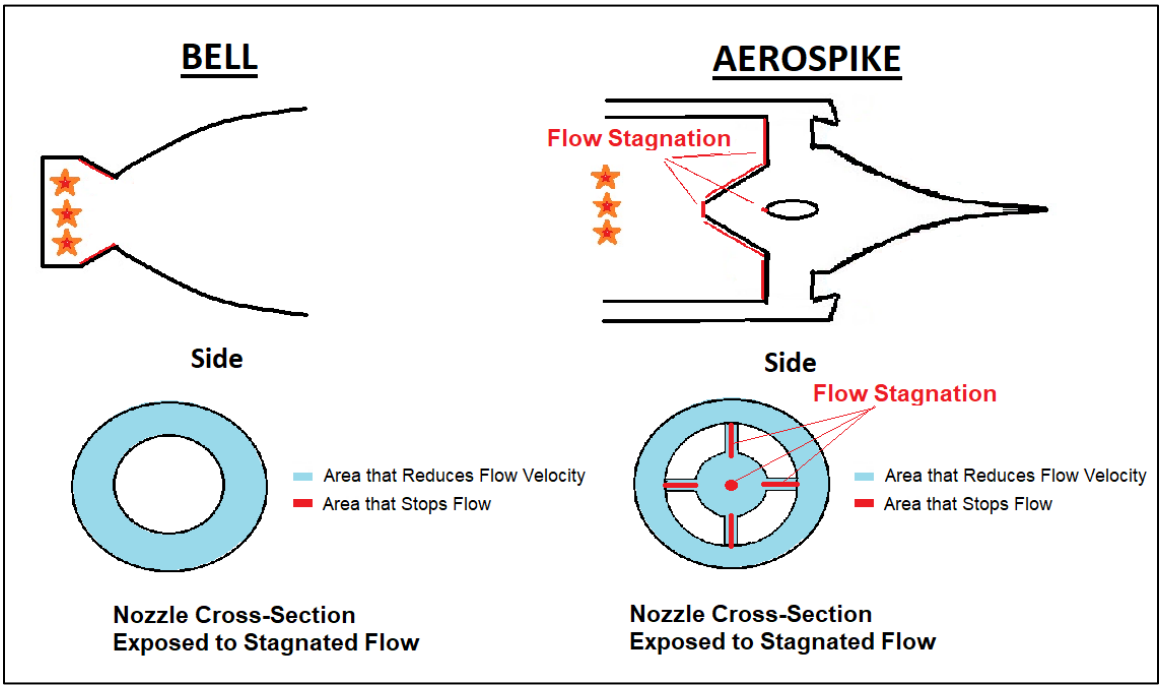

Figure 2.1. Diagram of flow stagnation points in nozzles.

Moving at near Mach 1 speeds in the throat, stagnation points appear along the needed support structures which are the sites of the most severe thermal degradation. Stagnation temperature, T_0, is proportional to fluid velocity, and its effects become more and more severe with an exponential relationship, with C_p as the specific heat capacity:

$$T_0 = T + \frac{V^2}{2C_p} \tag{2.7}$$

At the elevated fluid velocity seen near the nozzle throat, the structural material will experience a temperature significantly above the static temperature, T, which is near the combustion temperature, and can cause degradation if the material's melting point is locally exceeded. Heat degradation can cause enough damage to cause critical failure of internal components and result in the destruction of the propulsion system. A linear aerospike has a larger surface area to introduce cooling in comparison to the conical

aerospike, and larger vehicles such as the X-33 have been driven to the linear aerospike for this reason [13]. Coupled with the lack of flight data and fabrication difficulties, the vast majority of vehicles have opted for conventional bell nozzles rather than attempting to eke out more performance with a thermally vulnerable aerospike nozzle [7].

2.2 Literature Review

Currently, there is a lack of widespread flight test data for aerospike nozzles. This is partially due to the aerospike's particular novelty, and the general expense and risk of experimentally testing chemical rockets. During the aerospike's initial theorization and conceptual development in the early 1960's, their altitude compensating capabilities were explored for use on major launch vehicles. Rocketdyne proposed an aerospike design for the space shuttle, which was ultimately shelved for the more conventional RS-25. The RS-25, still one of the best rocket engines ever built, was a huge success, and aerospike research stagnated. Interest was renewed in the 1990's with NASA's X-33 program. A "space-plane" designed to attempt a single stage to orbit, the X-33 had a particular need for altitude compensation [13]. An aerospike nozzle was chosen for the X-33's propulsion system and was built in a linear design to handle the heating issue. The X-33's linear aerospike remains the largest aerospike engine ever tested, undergoing fourteen hot fire tests in 1997 that produced 412,000 lbs. of thrust at sea level with an I_{SP} of 339 seconds [13]. Interest in the X-33 inspired new research, and aerospike studies were conducted across the globe in the U.S, Europe, Japan, China, and Russia [14]. Somewhat controversially, the X-33 program was canceled due to failure of the liquid hydrogen tanks, and the nearly completed X-plane never got to see flight. This doomed the success of the largest and most heavily researched aerospike, one that was to provide thrust from

sea level to orbit and steer the X-33 via differential throttling. Since the program's cancellation, development efforts have been mostly small scale at the university level, although some studies have been able to utilize new techniques such as CFD software to provide more insight into aerospike behavior.

The numerical method of characteristics model used in the design of this experimental study was based on a technique adapted from a NASA technical memorandum from 1964. Titled "Fortran Program for Plug Nozzle Design," NASA TM X-53019, this original FORTRAN code adapted the known method of characteristics formulation to the aerospike geometry [15]. Other studies have built off of other design techniques developed in this same time period, such G. Angelino's 1964 journal paper detailing an approximate method for plug nozzle design [16]. In short, the conceptual design methods for determining the contour design of an aerospike nozzle have not changed significantly since their inception, and this study certainly leans heavily on their work to construct a physical model.

Several examples of studies from the post-X-33 era were examined, with particular emphasis on those who had conducted live tests. Most notably, a 2005 NASA study conducted at Dryden Flight Research Center in Edwards, CA, conducted Mach 1.6 solid rocket tests at 30,000 ft with aerospike nozzles [9]. However, the aerospike-equipped rockets saw reduced chamber pressure and thrust when compared to the conventional version of the rockets. The discrepancy was attributed to an erosive opening of the aerospike nozzle throats as the burns progressed, effectively lowering the nozzle expansion ratios. Although a success in "separat[ing] the real from the imagined, and making known the overlooked and unexpected problems," the research team wished for

follow-on design development and flight tests to correct the expansion ratio problem, of which records appear to be unobtainable [9]. These tests were the first flight tests of an aerospike using solid rocket motors, and their nozzle design is shown as the third panel of Fig 1.5. [9] Outside of NASA, a 2006 study from California State University, titled "Aerospike Engines for Nanosat and Small Launch Vehicles (NLV/SLV)" by Eric Besnard and John Garvey, designed and flew a 1000 lbf LOX/ethanol aerospike engine to 4,500 ft as part of a student design class [17]. After suffering engine destruction via central plug thermal failure, a successful redesign incorporated a titanium rod to carry the majority of the load upstream of the heat-concentrating throat. The study showed survivability for 20 seconds of burn time and that a successful aerospike flight could be demonstrated. The study also indicated that fuel savings could see an increase in payload of 23% if an aerospike could be fitted to a nano-launch size vehicle [17]. Future work recommended construction of a higher expansion ratio nozzle to show greater performance, as the thin annulus throat was unable to be made smaller with the machinery they had at their disposal. Tied to the same program, a 2009 California State University thesis by Temitayo A. Ladeinde investigated the effect of truncating the aerospike by 20% to reduce weight [8]. The experimental study found that truncating to this level resulted in near identical thrust performance to an error of 0.2%, making truncation a very attractive option to reduce weight. Not designed to be anything more than a comparison nozzle, the author wished for future work to improve nozzle inefficiency and fully characterize how far a spike can be truncated before major performance loss occurs [8].

Several overseas programs produced experimental aerospike results during this

time. A 1999 Japanese study did an experimental study on a truncated 14 kN aerospike using LOX/Methane as propellants [18]. The ground tests saw systematic disagreement with the method of characteristics model implemented, and it was concluded that liquid injector design was causing a cell-to-cell interaction between injection zones that hampered performance. Similar to the X-33, the combustor cells were included to drop the pressure to required entry levels for the larger aerospike engine, and resemble miniature bell nozzles. The study also included a CFD model of the truncation losses, and overall results indicated good clustered combustor design was critical to avoid oblique shockwaves and hamper downstream performance. A more recent Indian National Aerospace Laboratories study in 2009 by S.B. Verma built a small-scale conical aerospike [19], and confirmed known method of characteristics gains in fully contouring the aerospike to resemble a bell contour instead of a straight cone. Interestingly, this study also tested the effect of freestream motion via a wind tunnel to better simulate chaotic flight conditions. This freestream effect essentially decreases local pressure due to ambient motion, and translated to a performance loss of around 4%. On a separate note, the loss due to their 40% spike truncation amounted to about 3% of total performance, agreeing well with other results in literature [19]. Takeaways from these studies are that a thorough method-of-characteristics contour design without upstream shockwave interference from injection are critical to good aerospike performance, while spike truncation is a good option for reducing system weight.

The most relatable previous work comes from the Beijing University of Aeronautics and Astronautics with a 2003 study by Wang et al. that conducted small scale aerospike testing using GOX/GH2 propellants [14]**.** The study's primary focus was

to develop and test what they call a “tile-shaped aerospike configuration”, which consisted of adding combustion cells, similar to the aforementioned Japanese study. Unlike other experimental studies this one actively compared a bell nozzle to an aerospike over different nozzle pressure ratios (NPR). Although too large for most CubeSats at 4.5” across, this study is nevertheless the smallest experimental aerospike data found. Good agreement was found between their numerical method, following G. Angelino’s work, and the experimental tests, especially at high NPR. Their main tests were to incrementally increase the NPR across the nozzles via chamber pressure, and see which had better performance. At NPRs above 600, the Chinese aerospike did not appear to have significant gains over the bell, but the advantage became apparent at NPRs below 360. These tests were all done in the over-expanded regime, as the design point of the nozzle dictated an NPR of 1046. Figure 2.2 shows these results. No significant erosion was seen, and nozzle efficiency of 92% was reported at the heavily over-expanded NPR of 50. [14]These results favorably indicate that a CubeSat sized motor at lower thrust level could be made without running into scaling problems for the aerospike plume physics.

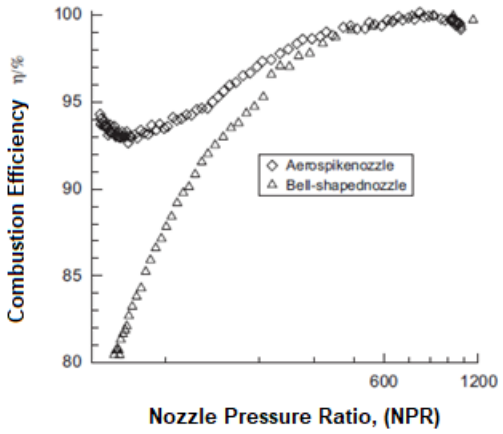

Figure 2.2. Altitude compensation results reported by Wang et al. [14]

This USU study will lean heavily on previous work done in the USU propulsion research lab, but of particular inspiration was an experimental study on a larger NanoSat sized aerospike, the MuPHyN [7]. Conventionally machined to a 10 cm size diameter, Eilers' experimental aerospike was of comparable size to the Chinese studies, but utilized a novel hybrid fuel design and N2O/HTPB as propellants. A multi-year project, much of the focus was on the further development of ongoing hybrid rocket technologies, such as spark ignition and helical fuel grains, that this study will be concerned with but not necessarily develop further. A thorough aerospike heating model, incorporating regenerative cooling, was developed as part of this study and was especially informative. Modeling of the aerospike plume through a CFD study was also conducted and included the thrust differential generated by side injection of nitrous oxide. An accelerated fuel regression rate, coupled with poor motor combustion, limited the success of the motor, although the regenerative cooling scheme worked admirably, as well as thrust vectoring through side ports. Further discussion of USU's work on hybrid motors that were utilized to build the test articles of this study will be outlined in more detail in later Chapters.

Aside from experimental results, many conceptual and simulative models have been developed over the years. Several were investigated for theoretical guidance, although this study's numerical technique is to be based off of Lee and Thompson's technical memorandum [15]. The most recent CFD simulation found was a 2017 study done by Swathi et al. at the Institute of Aeronautical Engineering in Hyderabad, India where the effect of truncating was investigated with modern ANSYS CFX software [20]. They found that the loss in thrust due to truncation was proportional to the truncation percentage, with more shockwaves being encountered at low pressure ratios and higher truncation.

Several NASA studies have been published detailing the plume physics. Ruf and McConnaughey summarize much of what was discovered in later university studies in their 1997 findings, titled "The Plume Physics Behind Aerospike Nozzle Altitude Compensation and Slipstream Effect" [21]. Included is a good discussion on the altitude adjusting characteristics of the aerospike, and a very similar curve to Fig. 2.2 is shown demonstrating superior characteristics to the bell nozzle in the over-expanded regime. This document was the basis of much of the theoretical descriptions discussed previously in the chapter, although much of the document then deals with the "Base-bleed" losses incorporated when the spike is truncated. Another NASA document of interest is "Analysis of Linear Aerospike Plume-Induced X-33 Base Heating Environment" by Ten-See Wang, which developed several numerical techniques to describe the freestream-body interaction [22]. The primary concern was plume-induced flow separation, and subsequent changes to the base-heating environment of the X-33. These and other theoretical studies give credence to experimental findings of smaller studies and provide

a level of feasibility for the testing of a small, CubeSat sized propulsion system.

2.3 Advances in Additive Manufacturing

None of the above studies have used the recently developed techniques of additive manufacturing. The annular throat of an aerospike nozzle is particularly difficult to construct by conventional methods, as the surrounding "cowl" and central spike are offset at the throat (see Fig. 3.3 of section 3.4). Additive manufacturing of metallic components did not exist during the X-33 era, and potentially makes fabrication of aerospike nozzles more feasible. 3D printing metal through laser sintering and electron beam melting greatly expands the potential to create internal cooling channels to address the aerospike's greatest deficiency. Internal cooling channels could never be made by a conventional machinist with the kind of curvature the aerospike demands, and this technology could make the launch vehicle sized, altitude-compensating aerospike possible. High temperature alloys such as Inconel and Niobium based alloys are capable of surviving the combustion chambers of chemical rockets [23]. 3D printing and computerized numerical control (CNC) machining can ease the manufacture of the aerospike architecture as well. Interior cantilevered joints were particularly difficult to make previously, but a 3D printer prints these with ease at small scale. These cantilevered points often slow the flow and experience degradation, and high melting point materials such as ceramics could be ideal for aerospike construction.

Metals currently available for 3D printing purposes include tungsten, which possesses the highest known melting point of any metal, and Inconel 718, a nickel-chromium superalloy known for its extraordinary strength at high temperatures. Both of these metals are available in powdered form, necessary for their utilization through

additive manufacturing. Size of parts is limited to the bed size of the printer, and depending on the print can take a week or more to produce a part. Once finished, the metal piece must be cut off from the build plate, which part designs must incorporate. [24]

Due to a cooperative agreement (CAN) with NASA In-Space Propulsion Engineer Daniel P. Cavender of Marshall Space Flight Center in Huntsville, Alabama, the USU Propulsion Research Laboratory has gained access to a high quality metal 3D printer, the M290. Built by the German company EOS, the M290 has a build plate of 250x250x325 mm, and is capable of printing Aluminum, Cobalt-Chrome, Inconel, Stainless Steel, and Titanium with its 400W Ytterbium fiber laser [24]. CAD models drawn up at USU are available to be printed in any of these materials using NASA Marshall's additive manufacturing branch (primary contact: Omar Mireles). Inconel was the material chosen for the following study due to its aforementioned formidable heating features. Inconel forms a thick, stable, passivating oxide layer when heated, protecting the metal from thermal attack [24]. Inconel 718, a particular composition of Inconel with 55% nickel, has a melting point of ~1330 ºC, nearly double that of most aluminum alloys. Stainless steel exhibits a higher melting point of ~1450 ºC, but experiences a steeper degradation in strength than Inconel with rising temperature. [24] Tungsten outshines the competition with a melting point of 3422 ºC, but was unavailable to be printed through the NASA CAN at the time of this study [24].

Ceramics manufacturing has also expanded with increased machinability and the beginning of additive manufacturing through the use of slurries. Several companies, such as Robocasting Enterprises LLC in Albuquerque, offer custom ceramics manufacturing

through additive slurries, although currently capabilities are limited [25]. Universities are attacking the problem as well; Dr. Emre Gunduz of Purdue's Zucrow Labs is developing a technique of micro-vibrations to ease out viscous slurries through printer head orifices in a precise manner [26]. It seems likely that within a few years additive ceramic manufacturing could advance to a level high enough to produce geometries as complex as a cantilevered aerospike. Even within current bounds, the potential for ceramic components in aerospike nozzles has become increasingly feasible. Ceramics offer some of the highest known melting temperatures of engineering materials known to man, but have historically suffered from being severely brittle, which limits their use in applications that will be subject to force loads. Another option is machinable ceramics, which via CNC and other techniques could potentially be crafted into an aerospike nozzle configuration. These, however, would suffer similar limitations to current metal designs such as producing the annular throat at high expansion ratios. Macor®, a proprietary ceramic composition emblematic of machinable varieties, also suffers from a reduced melting point in comparison to other ceramics [27]. With significant challenges to the machining process, an aerospike nozzle crafted from machinable ceramic seems like an option that would require extensive development before useful utilization.

CHAPTER III

MODELING AND ANALYSIS

An aerospike nozzle, being downstream of all combustion components, can be integrated into most propellant schemes. Due to availability, this study will integrate an aerospike into an ABS/GOX hybrid rocket motor of the type commonly tested at USU under the direction of Dr. Stephen Whitmore. These are fairly novel motors that exhibit certain unique characteristics. As such, an understanding of ABS/GOX hybrid motor characteristics is important to deciphering and understanding the later results of this study.

Distinct from both solid rockets and liquid rockets, but carrying attributes of both, hybrid rockets carry solid fuel but store oxidizer as a fluid. Volumetrically, a hybrid system is often inefficient as both a tank, a primary source of weight in liquid systems, and a solid fuel grain, a primary source of weight in solid rockets, have to be included. However, this separation makes hybrid rockets intrinsically safe, as both propellants are inert. Combustion only occurs when the fuel is converted to gaseous state, a high energy process that has historically made hybrid rockets difficult to ignite. Numerous safety features, such as check valves to prevent backflow, make stopping combustion a fairly straightforward process of cutting off the oxidizer. This gives hybrids an operational advantage over solid rockets in their inherent ability to be throttled, stopped, and restarted. Solid rockets offer extremely high volumetric efficiency and will always have their application in certain scenarios, so hybrids are mainly attempting to compete in more complex applications that require multiple motor pulses. Currently, most of these multiple start systems, including those that propel small spacecraft, are liquid systems. To make hybrids competitive, current research areas include improving hybrid's

characteristically low regression rate, ignition reliability issues, and I_{SP} performance [3].

A large percentage of rocket launch failures are due to malfunctions in the propulsion system, and the safety of hybrid systems has potential cost-saving benefits [3]. Hybrid fuels are generally made from polymers, cheap materials that currently undergo large production volumes. Choice of fluid oxidizer is touchier, since many good oxidizers are highly flammable or incompatible with many common materials. However, many existing liquid systems use highly toxic chemicals as well. In particular, mono-methyl hydrazine, commonly used as a hypergolic with nitrogen tetroxide oxidizer, is carcinogenic, explosive, and burns upon contact. One of the most reliable and widely-used propulsion systems, hydrazine thrusters have been used on everything from the voyager probes to roll control for the space shuttle. The cost due to the danger of this propellant is exorbitant and has become increasingly prohibitive in recent years. During hydrazine fueling, entire launch complexes are shut down except for handling personnel, which require full Self Contained Atmospheric Protective Ensemble (SCAPE) suits [28]. Transportation and storing of hydrazine is heavily regulated, with good reason. Hybrids represent a potential option in the slew of proposed "green" propellant options to replace hydrazine and avoid operational hazards and their subsequent costs. As a benchmark for competition, hydrazine systems have an I_{SP} of 220 seconds and nearly unlimited restarts, freeze at 1 ˚C, and are capable of cold restarts [28]**.**

The USU hybrid program has the green propulsion market in mind, and is enabled by a novel arc-ignition system that has had significantly reliable performance. 3D printed Acrylonitrile Butadiene Styrene (ABS) fuel gasifies when subjected to a high voltage spark, etching a charred path across its surface. The heated gaseous volume produced is

enough to initiate combustion in the presence of gaseous oxidizer. While the spark "cap" is required to be ABS for the repeatable pyrolyzation effect, several different hydrocarbon fuels have been investigated for use in the solid grain, including HTPB and HIPS. The primary oxidizers investigated have been Gaseous Oxygen (GOX), Nitrous Oxide (N2O), and Hydrogen Peroxide (H2O2). The simplest and most mature of these technologies is the ABS/GOX configuration, which was chosen for this study because of ready availability, wealth of archived test results, and generally reliable behavior. The successes of these developing technologies is detailed in several publications, including Whitmore and Peterson [29], and Whitmore and Merkley [30]. The physical components used are shown later in Chapter IV, including the arc-ignition spark hardware.

3.1 ABS/GOX Hybrid Rocket Combustion Characteristics

Hybrid rocket combustion has been historically difficult to model for several reasons. Unlike solid rockets, hybrid motors are not pressure coupled with respect to fuel regression rate [4]. This can make it difficult to raise fuel regression rate, and corresponding mass flow and thrust. Saint Robert's law is the conventionally used expression to predict solid rocket fuel regression [3]:

$$\dot{r}_{solid} = a\, P_0^n \tag{3.1}$$

with $\dot{r}$ as the fuel regression rate, P_0 as the motor chamber pressure, and a, n are empirically derived parameters. An instantaneous change in P_0causes a proportional response in fuel regression. Incidentally, this model has been proven highly inaccurate for hybrid motors, and illustrates another source of the safe characteristics of hybrids. Pressure spikes can occur in a solid motor for a variety of reasons, such as grain fracture, which cause a positive feedback interaction that results in rapid pressurization and the

destruction of the motor. This rapid pressurization will never occur in a hybrid. The classical Marxman-Gilbert model, outlined in 1963, was the first attempt at characterizing hybrid fuel regression [4]. This model was made with the assumptions that hybrid fuel regression ($\dot{r}_{hybrid}$) is dominated by diffusion and not chemical kinetics, and that turbulent flow is experienced along the entire fuel grain due to the vaporizing mass [4]:

$$\dot{r}_{hybrid} = \frac{0.36}{\rho_{fuel}} * \left(\frac{\mu_\infty}{x}\right)^{0.2} * \frac{G^{0.8} * B^{0.23}}{Pr^{0.7}} \tag{3.2}$$

$$G = \frac{\dot{m}}{A_t} \tag{3.3}$$

$$B = \frac{\dot{m}_{fuel} * U_e}{\tau * A_{wall}} \tag{3.4}$$

$$B \approx \frac{\Delta h_{flame}}{h_v} \tag{3.5}$$

Clearly, this model is significantly more complicated than the solid motor model, and many different parameters contribute. Fuel density (ρ_{fuel}), flow viscosity (μ_∞), and Prandtl number are all resultant of propellant choices. G, total mass flux, and B, a parameter unique to hybrid models known as the "blowing coefficient," contribute strongly as well [4]. Total mass flux can be difficult to measure experimentally since the fuel portion of the flow is generated internally and flowmeters cannot be place on the nozzle outlet due to the extreme temperature environment. The incorporation of the blowing coefficient is needed for the model due to the fact that formation of the boundary layer is accentuated in a hybrid motor because of the radial flow generation, via pyrolyzing fuel, that runs down the length of the motor. This effect can be captured by adding a radial component to the boundary layer flow, the strength of which is accounted

for by the blowing coefficient. The continuous growth of the boundary layer down the motor, seen in Fig. 3.1, is in fact analogous to boundary layer formation across a flat plate [31]. This flat plate analogy allows the Reynold's analogy and Blasius skin friction approximation to be applied, leading to the more convenient definition of B seen in Eq. (3.5). Approximations can be made for the net enthalpy change Δh_{flame}, and the heat of vaporization, h_v, remains a fairly constant parameter.

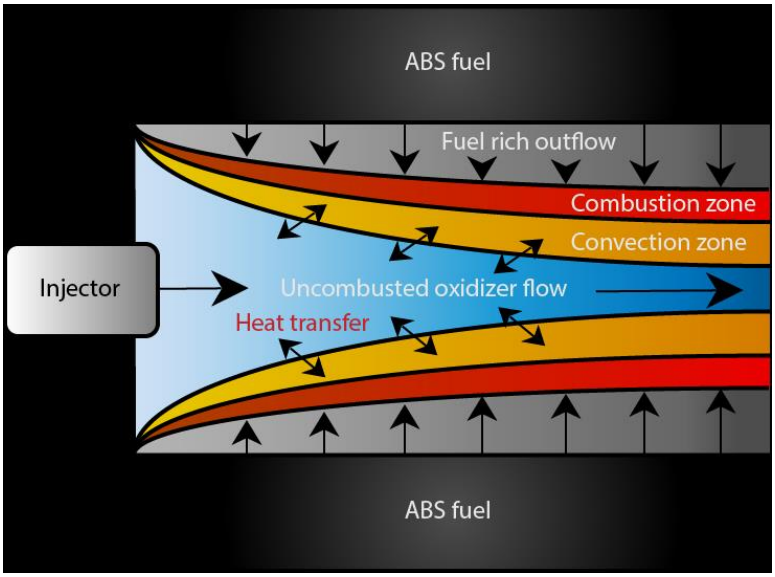

Figure 3.1. Boundary layer development in a hybrid rocket motor. [31]

An interesting ramification of hybrid combustion that is illustrated in the Marxman model is a shift in the instantaneous Oxidizer-to-Fuel Ratio, (O/F), as a hybrid motor burns. For a cylindrical port through a cylindrical fuel grain, the port diameter $D(t)$ will open up over time $(0 - t)$ from initial diameter D_0 according to the following relation [3]:

$$D(t) = D_0 + 2\int_0^t \dot{r}_{hybrid} * dt \tag{3.6}$$

Rearranging from the Marxman regression formulation, the positive mean O/F shift

intrinsic to hybrid rockets is shown as Eq. (3.7), with L representing fuel grain length [3]:

$$O/F_{mean}(t) = 5.58244 * Pr^{\frac{2}{3}} * \left(\frac{h_v}{\Delta h_{flame}}\right)^{0.23} * \left(\frac{\dot{m}_{ox}}{\mu * L}\right)^{0.2} * \left(\frac{D(t)}{L}\right)^{0.6} \quad (3.7)$$

For constant oxidizer mass flow rate, dictated by system components upstream of the oxidizer injection, and fluid parameters that remain relatively constant, we can see that the O/F ratio will increase over time as a cylindrical port opens up. In other words, a typical hybrid rocket will burn leaner over time. This is perhaps not intuitive, especially to those familiar with solid rocket combustion, where extensive research has been conducted in cross-sectional patterns to address the increase in pressure that comes with cylindrical solid motor port burning. From a design standpoint, this expression also shows that key geometric aspects of hybrid motor design include length of the rocket and the diameter of its initial port.

Hybrid rocket propellant combustion performance is highly tied to O/F ratio. An ideal O/F ratio is tied to stoichiometric combustion, where all reactants (fuel and oxidizer) are consumed. In practice, true stoichiometric combustion down to the last molecule is never achievable, but control of reactant proportions is much more easily attainable in solid rockets where fuel and oxidizer are proportionally mixed together. Liquid rockets can inject at stoichiometrically proportional rates as well, so the O/F shift in hybrid rockets represents a fundamental inefficiency that engineers have been trying to counteract since the advent of hybrid rocketry [30].

An illuminating metric that helps characterize burn efficiency is characteristic velocity, or C^*: [4]

$$C^* = \left(\frac{P_0 * A_t}{\dot{m}_{exit}}\right) \tag{3.8}$$

Characteristic velocity is not directly dependent on gas combustion properties such as heat released during reaction, but it is indicative of combustion efficiency. P_0 rises with efficient combustion (i.e. the closer to the stoichiometric point), so for a fixed nozzle predicting C^* with the Marxman model will show a variance in combustion efficiency. Equilibrium combustion parameters for the model were calculated using Chemical Equilibrium with Applications (CEA), an extensive free software developed by NASA. Using CEA with a fixed nozzle geometry, the associated prediction in characteristic velocity for ABS/GOX propellants is shown in Fig. 3.2.

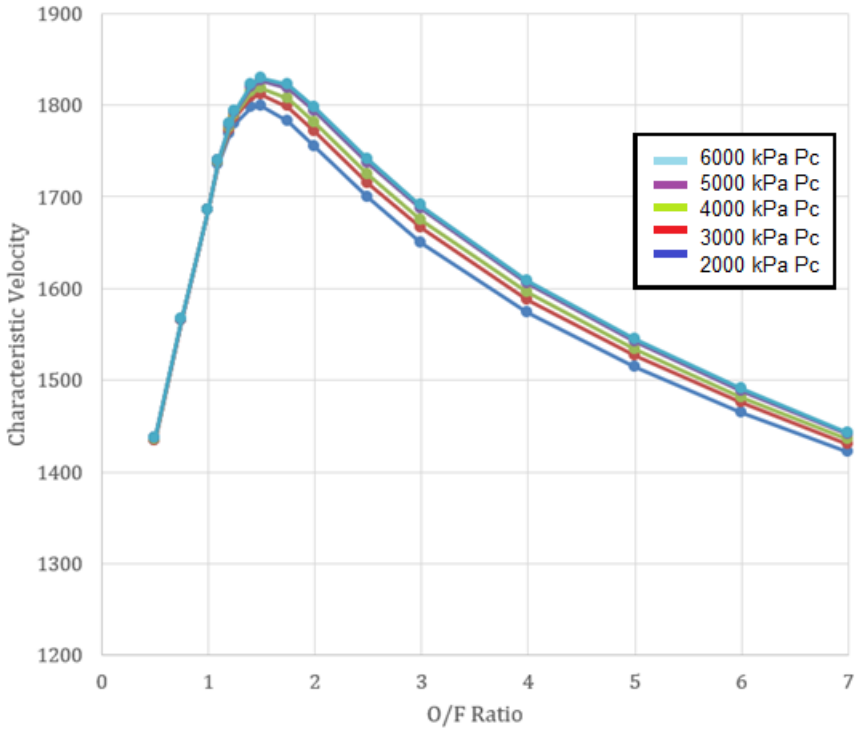

Figure 3.2. ABS/GOX Hybrid rocket performance dependence on mean oxidizer-to-fuel ratio. *Shown for various motor chamber pressures (Pc).*

For ABS/GOX hybrid propellants, the stoichiometric burn condition that leads to

maximum C^* lies around a macroscopic O/F ratio ~1.6, with a sharp drop in performance at "fuel rich" O/F ratios below 1. However, due to intrinsic O/F shift, a hybrid motor cannot be made to a specific length and initial port diameter to optimize C^*. Design alignments can be made for a mean O/F to lie at 1.6, but the thrust and I_{SP} performance will need to be averaged across the motor burn life as well.

The C^* trend shown in Fig. 3.2 will scale accordingly for different combustion parameters. A fair degree of unavoidable uncertainty comes into play from the CEA chemistry calculations. The chemical solver is set up to accept input scenarios that mimic a rocket's combustion chamber, but these results are highly dependent on equilibrium assumptions and precise knowledge of propellant composition. Equilibrium parameters are calculated in CEA using an algorithm that minimizes Gibb's free energy, G, by reacting intermittent species produced by initial combustion. G is a measure of the relative stability of a chemical system, and physical reactions have been proven to minimize G [3]. The Gibb's free energy analysis carries out intermediate reactions until chemical equilibrium is achieved with the ratio of reactants and products constant. Reaching chemical equilibrium may take some time depending on reaction rates of the chemicals in question. For hybrid combustion, formation of the central boundary layer indicates the flow has significant axial velocity. Intermittent reactant species, including some percentage of unreacted oxidizer, may still exist in the flow before entering the nozzle. At the nozzle throat, acceleration to Mach 1 nullifies the equilibrium assumption completely, and for the remainder of the CEA calculation the reaction is considered *frozen,* with no new reactions commencing. The change to frozen flow is generally a good assumption within a small rocket nozzle since flow exits the nozzle within fractions

of a second. However, the presence of some percentage of intermediate species in hybrid flow casts a degree of uncertainty on any Gibb's free energy equilibrium analysis.

Although GOX is a common gas that can be purified to exceedingly high levels, ABS plastic can vary significantly between manufacturers, further complicating the CEA calculation. ABS is a thermoplastic polymer consisting of a mix of three monomers, Acrylonitrile (C_3H_3N), Butadiene (C_4H_6), and Styrene (C_8H_8) [29]. Polymerization usually results in a composition of roughly 1/3 contribution from each monomer, but this can vary widely from different manufacturers and production techniques. In particular, ABS blends intended to be created for 3D printing can vary substantially from higher density, conventionally produced extruded ABS. The ABS fuel used in this study consisted of uniform-geometry extruded stock for the majority of its length, with a small section near the igniter required to be made from 3D printed ABS for ignition purposes.

Unfortunately, manufacturers are often unwilling to provide exact composition details of their product, and best guess values for extruded ABS were taken from a previous study by Whitmore and Petersen [29]. Ultimately, further model uncertainty was introduced by best-guess approximations for extruded ABS fuel, and by using this extruded ABS composition across the entire fuel grain when a small percentage was known to be 3D printed ABS. Statistical variance in the results of chapter V could easily have been affected by uncertainty in assumptions used by the chemical analysis.

Although the Marxman model is generally applicable and useful for understanding hybrid combustion, recent research developments have added refinement to the classical formulation. Significantly, a recent USU study by Whitmore and Merkley challenges the conventional O/F shift from rich to lean in the case of small hybrids [30].

In fact, due to a normally negligible radiative energy transfer, Merkley's correction actually anticipates a negative O/F shift due to radiation becoming the primary mechanism of inducing fuel regression. This effect was found to progressively become more pronounced as motor diameter shrank, and a proposed correction to the Marxman model was proven to match with experimental testing. The existing CubeSat-sized ABS/GOX hybrid proposed for testing fits into the size category of this correction. This model greatly resembles the classical formulation, with the added radiative term, $\dot{r}_{rad}$, included: [30]

$$\dot{r}_{conv} = \frac{0.635 * \tau * G_{ox}^{n}}{n_{hybrid} * \rho_{fuel} * Pr^{\frac{2}{3}} * B^{0.77}} * \left(\frac{\Delta h_{flame}}{h_v}\right) * \left(\frac{\mu}{L}\right)^{1-n_{hybrid}} \tag{3.9}$$

$$\dot{r}_{rad} = \frac{\sigma * (\epsilon T_{t1}^{4} - \alpha T_{t2}^{4})}{\rho_f h_v} \tag{3.10}$$

$$\dot{r}_{hybrid} = \dot{r}_{conv} + \dot{r}_{rad} \tag{3.11}$$

In addition to new radiative parameters of optical absorptivity α, optical emissivity ϵ, and the Stefan-Boltzmann constant σ, the radiative model incorporates an empirically determined burn exponent n_{hybrid}. Therefore, this model needs tailoring to experimental results to be meaningful. Its primary use here is as a theoretical explanation for the negative O/F shift from lean to rich seen in USU's small motors. These guiding models provide validity to experimental tests and enable performance gains from nozzle improvements to be identified and understood.

3.2 Experimental Determination of Hybrid Motor Performance

To experimentally determine the change in O/F ratio over a test burn, and ultimately the performance parameters of I_{SP} and thrust, a chain of calculations must be done on raw instrumentation measurements. This process is well established in the USU hybrid rocketry program [7] [28] [30], and this study will utilize prior computational resources and instrumentation systems to determine any possible improvements from an aerospike nozzle.

First, total mass flow rate through the nozzle throat must be determined. Total mass flow rate, $\dot{m}_{total}$, can be assumed to be the simple sum of reaction products:

$$\dot{m}_{total} = \dot{m}_f + \dot{m}_{ox} \tag{3.12}$$

As mentioned before, fuel mass flow rate, $\dot{m}_f$, is nigh impossible to measure directly due to the hostility of the nozzle exit environment, and therefore must be calculated. Physical mass measurements of the fuel grain give an indication of the total amount of fuel burned, and provide an anchor point for the fuel mass calculation to match. Oxidizer mass flow rate, $\dot{m}_{ox}$, can luckily be readily determined via a venturi flowmeter located upstream of the oxidizer injection. Forced through a venturi duct with known area change, the compressible form of the venturi equation can be used to calculate mass flow rate from two sensed pressures ($P1, P2$). This historical equation is well known and widely used, and was also taken from Anderson's text [1]:

$$\dot{m}_{ox} = C_d * A1 * P_0 * \sqrt{\left(\frac{2\gamma}{\gamma - 1}\right) * \frac{1}{R_g * T}\left[\left(\frac{P1}{P_0}\right)^{\frac{2}{\gamma}} - \left(\frac{P1}{P_0}\right)^{\frac{\gamma+1}{\gamma}}\right]} \tag{3.13}$$

$$P_0 = \left[\frac{\left(\frac{A1}{A2}\right)^2 * (P1)^{\frac{\gamma+1}{\gamma}} - (P2)^{\frac{\gamma+1}{\gamma}}}{\left(\frac{A1}{A2}\right)^2 * (P1)^{\frac{2}{\gamma}} - (P2)^{\frac{2}{\gamma}}}\right] \tag{3.14}$$

Physical cross-sectional areas $A1$ and $A2$ are known by design, and an attached thermocouple gives a temperature measurement T. Stagnation pressure P_0 can then be found with knowledge of γ, the ratio of specific heats of the fluid passing through the venturi, and R_g, that fluid's specific gas constant. One of the most important thermal parameters in compressible flow, γ has a minor dependence on temperature but always stays close to a value of 1.4 for GOX (similar to air) [3]. To obtain $\dot{m}_{ox}$ from the compressible venturi equation, the only other parameter needed is the discharge coefficient, C_d, a measure of losses through the venturi which can be experimentally determined for specific flowmeter setups.

Next, total mass flow rate is calculated off of obtained pressure measurements in the combustion chamber. Unlike a temperature probe that must be in direct contact with the combustion zone, a pressure transducer can be placed a safe length away while still making an accurate measurement. Assuming choked nozzle flow at the throat, the choking mass flow equation can be used to obtain total mass flow rate [28]:

$$\dot{m}_{total} = A_t * P_0 * \sqrt{\frac{\gamma}{R_g * T_0} * \left(\frac{2}{\gamma+1}\right)^{\frac{\gamma+1}{\gamma-1}}} \tag{3.15}$$

with stagnation pressure assumed to be near the measured chamber pressure, and CEA chemical analysis providing the flame temperature T_0. Important ramifications of the chamber pressure, P_0, measurement are discussed later in this chapter, but are considered exact for the remainder of this analysis. The choked nozzle assumption can be easily verified with a flat chamber pressure profile, and this calculation provides high accuracy

[28]. With Eq. (3.12), $\dot{m}_{total}$ allows calculation of the fuel mass flow rate $\dot{m}_f$, and an instantaneous O/F can be calculated at each point in time.

$$O/F(t) = \frac{\dot{m}_{ox}(t)}{\dot{m}_{total}(t) - \dot{m}_{ox}(t)} \tag{3.16}$$

To verify the calculation, total fuel mass is weighed on a scale prior to and after a burn, to see if agreement is found with the calculated consumed mass:

$$\Delta M_{fuel} = \int_0^t (\dot{m}_{total} - \dot{m}_{ox})dt \tag{3.17}$$

The above calculations are dependent on the chemical parameters obtained from CEA, such as γ, R_g and T_0. These have to be recalculated for each instance in time due to variations in the measured values. These values are calculated for an ideal combustion reaction at equilibrium, which rarely happens in practice due to losses and inefficiencies in the combustion chamber [28]. However, a multiplicative factor called the combustion efficiency, n^*, can help capture the main effect of these losses by scaling the equilibrium flame temperature:

$$T_{0_{actual}} = n^{*2} * T_{0_{ideal}} \tag{3.18}$$

Although this scaling correction does not account for temperature dependence of γ and R_g, these are usually negligible in the face of systematic errors that arise from the difficulty of measuring all parameters in hybrid combustion. $n^*$is an experimentally determined tailorable parameter, and is iterated through Eqs. (3.13-3.17) until agreement matches between the calculated consumed fuel and the measured fuel mass lost.

After this iteration and comparison process has honed in on a trustworthy $\dot{m}_{total}$, determination of the critical parameters of thrust and I_{SP} is possible. Thrust is capable of being measured directly on a properly constructed test stands trough use of a load cell.

The load cell inevitably does not capture all the force produced by the rocket nozzle, as piping and other structural elements take a small proportion of the load (see Fig. 4.9.1 for load cell location) [32]. To back up the load cell thrust reading, further calculations are conducted to align model parameters with calculated thrust. The thrust calculations are nozzle dependent, however, so a different thrust calculation must be done for bell nozzles and the aerospikes. These thrust calculations, and their issues, are outlined in the next sections. The thrust calculations are based off measured chamber pressure, CEA chemical parameters affected by n^*, and known nozzle geometry parameters. Matching the thrust prediction with the load cell refines the experimental data. Looking back to Eq. (1.5) in section 1.2, with the inclusion of thrust all parameters needed to calculate the I_{SP} over the burn have been calculated. The calculation methods outlined in this section can therefore identify I_{SP} differences between experimental tests, and are used to quantify potential gains from utilization of an aerospike nozzle.

3.3 Quasi 1D Thrust Model for Bell Nozzles

Thrust models for bell nozzles are well understood and readily described in literature. For this study, the model chosen was a quasi 1D approximation taken from Anderson's book [1]. This calculation technique was the one utilized by previous ABS/GOX motor testing at USU [32]. Quasi 1-dimensional refers to the assumption that model parameters only vary along the length of the nozzle and remain constant across the cross-sectional area at any point. Higher fidelity models such as the method of characteristics can provide flight-worthy predictions of model thrust, but for this study the 1-D approximation was chosen for simplicity and general reliability. Once again rooted in the fundamental conservation equations of energy, momentum, and mass, the

nozzle is treated as an isentropic expansion (adiabatic and reversible). These assumptions provide high agreement for nozzles behaving at the design condition, although real-world losses often contribute a penalty of around 3% on an isentropic nozzle. [3]

For a given nozzle, the Mach number at any point along the profile can be solved for using a famous relation, where x is lengthwise location: [1]

$$\frac{A(x)}{A_t} = \frac{1}{M(x)} * \left[\left(\frac{2}{\gamma+1}\right) * \left(1 + \frac{\gamma-1}{2} * M(x)^2\right)\right]^{\frac{\gamma+1}{2*(\gamma-1)}} \tag{3.19}$$

Conditions at the throat, including pressure, area, and the choked Mach number condition of M =1 are all known. Eq. (3.19) can therefore be used to solve for the exit Mach number, M_e, when the nozzle expansion ratio is known. An isentropic expansion will maintain stagnation temperature and stagnation pressure, and can be used to calculate the temperature and pressure profiles through the nozzle: [1]

$$T(x) = \frac{T_0}{\left(1 + \frac{(\gamma-1)}{2} * M(x)^2\right)} \tag{3.20}$$

$$P(x) = \frac{P_0}{\left(1 + \frac{(\gamma-1)}{2} * M(x)^2\right)^{\frac{\gamma}{\gamma-1}}} \tag{3.21}$$

$$V(x) = M(x) * \sqrt{R_g * T * \gamma} \tag{3.22}$$

Calculation of the above profiles from Eqs. (3.20-3.22) include exit conditions, and substituting into the rocket thrust Eq. (1.1) yields the thrust generated from the bell nozzle. At the design condition, the pressure difference ($p_{exit} - p_\infty$) is equal to zero, and thrust is solely generated from the momentum thrust term.

3.4 Method of Characteristics Aerospike Thrust Model

Unlike the conical bell nozzles produced for this study, the full aerospike contour was fabricated. This was primarily because the CNC machining utilized was capable of creating the curved aerospike contour, but would have been needed even for an un-contoured conical aerospike. To specify the aerospike contour, a numerical method adapted from Thompson and Lee's 1964 NASA technical memorandum on plug nozzle design was followed [15]. Aerospike nozzles exhibit significantly different thrust profiles when in the over-expanded flow regime, and this model only applies to the design condition and under-expanded flow regimes. [15]

The method of characteristics was first used to develop minimum length bell nozzle contours by Ludwig Prandtl and Adolf Busemann in 1929. [1]Anderson's classroom text provides a brief history of the historical theory of characteristics, which had been pioneered by French mathematician Jacques Salomon Hadamard. The method builds off of identifying "characteristic lines" in a flow field in which flow derivatives are discontinuous, and then constructing flow relations from the fundamental conservation equations of momentum, energy, and mass that remain constant along the characteristic lines. A solvable system of algebraic equations can then be written with unknown flow field parameters along a specified number of grid points along the lines. [1]

The method of characteristics formulation of the aerospike contour follows a similar process. The flow is assumed to be two-dimensional and irrotational. [1] Rotational flow arises from non-isentropic losses, so this method is once again assuming an isentropic expansion in the nozzle. First, the exit Mach number is determined from Eq. (3.19), using quasi 1D assumptions. Eqs. (3.23) and (3.24) can then be used to solve for the throat angle, δ, between the central spike plug and the surrounding cowl, as shown in

Fig. 3.3: [15]

$$v_{exit} = \sqrt{\frac{\gamma+1}{\gamma-1}}\tan^{-1}\left\{\sqrt{\frac{\gamma-1}{\gamma+1}\left({M_{exit}}^2-1\right)}\right\} - \tan^{-1}\left\{\sqrt{\left({M_{exit}}^2-1\right)}\right\} \quad (3.23)$$

$$\delta = 90^{\circ} - v_{exit} \quad (3.24)$$

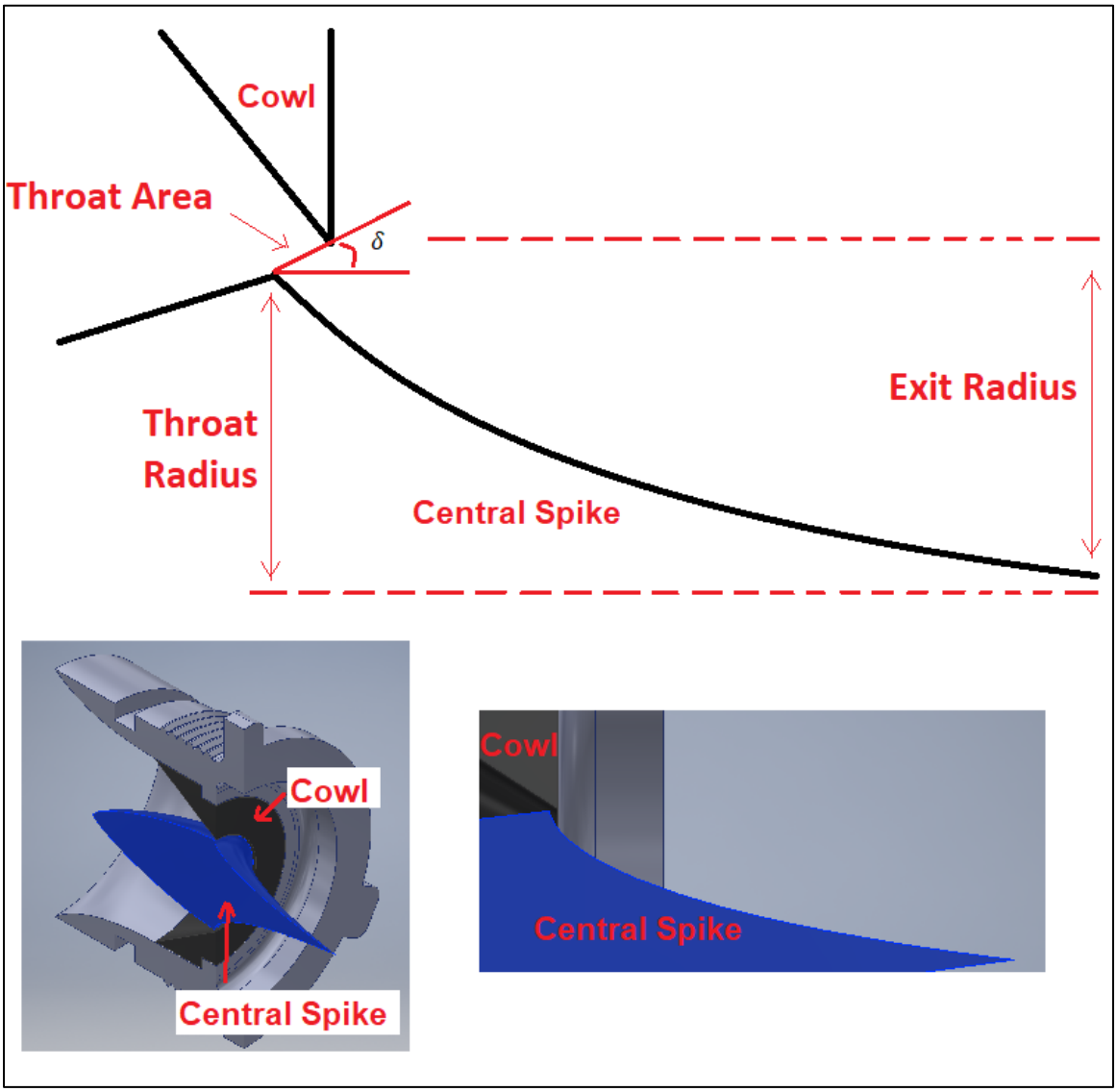

Figure 3.3. Detail of aerospike throat geometry.

Eq. (3.24) is derived from an equality made along a characteristic line for a specified

nozzle exit angle, which is zero for an untruncated spike. Physically, υ_{exit} is the component of vertical velocity at the exit, with υ varying along the length of the nozzle as seen in Eq. (3.25) [1]. Eq (3.26) shows the derived compatibility equation for negative-sloped characteristic lines in the nozzle flow, where K_{-} is a constant:

$$\upsilon(x) = V(x) * \sin(\theta(x)) \tag{3.25}$$

$$\theta(x) + \upsilon\big(M(x)\big) = K_{-} \tag{3.26}$$

By dividing the spike contour lengthwise into n different points, n characteristic lines can be drawn as expansion lines from the nozzle throat. The following equations can then be iterated n times until a spike radius, R_n, is known for each characteristic line, fully defining the aerospike geometry: [15]

$$M_{n+1} = M_n + \frac{M_{exit} - 1}{n} \tag{3.27}$$

$$\upsilon_{n+1} = \sqrt{\frac{\gamma+1}{\gamma-1}}\, tan^{-1}\left\{\sqrt{\frac{\gamma-1}{\gamma+1}\left({M_{n+1}}^2 - 1\right)}\right\} - tan^{-1}\left\{\sqrt{\left({M_{n+1}}^2 - 1\right)}\right\} \tag{3.28}$$

$$\mu_{n+1} = sin^{-1}\left(\frac{1}{M_{n+1}}\right) \tag{3.29}$$

$$x_{n+1} = \frac{R_{exit} - R_{n+1}}{\tan(\upsilon_{exit} - \upsilon_{n+1} + \mu_{n+1})} \tag{3.30}$$

$$R_{n+1} = R_{exit}\sqrt{1 - \frac{\sin(\upsilon_{exit} - \upsilon_{n+1} + \mu_{n+1})}{\varepsilon} * \left[\left(\frac{2}{\gamma+1}\right) * \left(1 + \frac{\gamma-1}{2} * {M_{n+1}}^2\right)\right]^{\frac{\gamma+1}{2*(\gamma-1)}}} \tag{3.31}$$

Unlike the thrust equations shown previously for the bell nozzle that separate thrust into

momentum and pressure terms, for aerospike thrust modeling it makes more sense to split the aerospike nozzle's thrust terms into thrust generated at the throat and along the spike. Eqs. (3.27-3.31) solved for enough parameters to determine the pressure profile, $P(x)$, along the spike, which allows for a summed force, F_{Spike}, to be calculated. At the throat, both momentum and pressure thrust terms are included, and Eq. (3.33) subsequently greatly resembles the previous bell nozzle thrust equations: [15]

$$P(x) = \frac{P_0}{\left(\left(1 + \frac{\gamma - 1}{2} M(x)^2\right)^{\frac{\gamma}{\gamma - 1}}\right)} \tag{3.32}$$

$$F_{Throat} = [\dot{m}_{exit} V_t + (p_t A_t - p_\infty A_t)] * \sin(\delta) \tag{3.33}$$

$$F_{Spike} = \sum_{j=0}^{N} \left(\frac{p_j + p_{j+1}}{2} - p_\infty\right) * \pi * (R_j^2 - R_{j+1}^2) \tag{3.34}$$

$$F_{Aerospike} = F_{Throat} + F_{Spike} \tag{3.35}$$

Experimental thrust and I_{SP} can be obtained using the process outlined above, but not for the over-expanded aerospike regime. Unfortunately, no simple algorithm exists for modeling the chain of entrained shock waves in the literature. Visible indications of shock diamonds, accompanied by a performance loss, can be used to determine over-expansion. In these cases, the above model cannot be used. [4]

The spike contour downstream of the nozzle throat is ideally determined by characteristics of compressible flow, however, the geometry upstream of the throat can be more arbitrary. So long as a convergence on the nozzle throat produces choked flow the nozzle will function. In an effort to reduce stagnation points on the front end of the central spike, an aerodynamic Von Karman ogive profile was chosen [33], shown in Fig. 3.4. The profile chosen belongs to a series of functions known as Haack series, and

literature provides a well-established function to determine the profile: [33]

$$R_{Haack} = \frac{R_{exit}}{\sqrt{\pi}} \sqrt{\theta_{Haack} - \frac{\sin(2 * \theta_{Haack})}{2}} \tag{3.36}$$

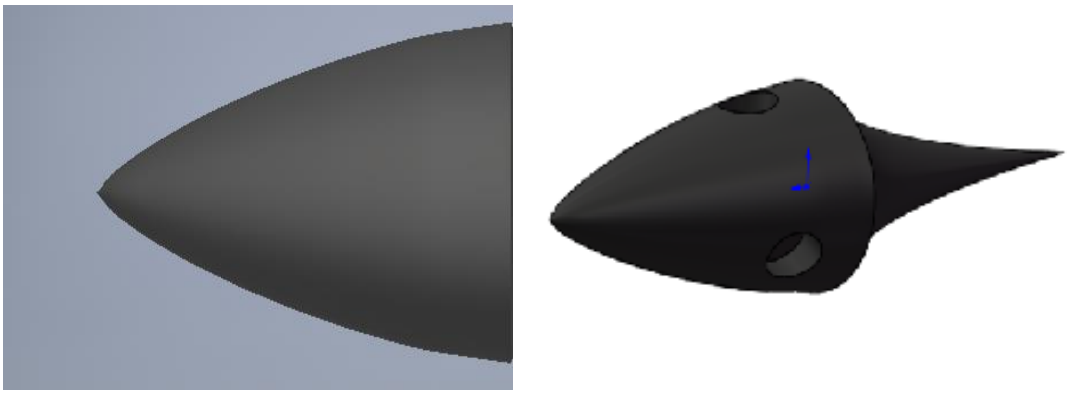

Figure 3.4. Aerodynamic profile of the Von Karman Haack profile and interface to aerospike plug. [33]

3.5 Analysis Methods

The above models provide a means of determining motor performance metrics from experimentally determined inputs. Sampled in real time, the performance over an entire burn sequence can be reconstructed. Some aspects of real motor performance, not fully captured in the idealized models above, were determined to be significantly skewing the results of the above models when applied to the data sets generated by this study. The following sections outline several analytical techniques used to properly apply the above thrust models.

3.5.1 Addition of Normal Shockwave Model to Bell Nozzle Model

Previous experience in literature shows that the isentropic bell nozzle

approximation breaks down in the over-expanded case, where a shockwave can be formed that interrupts nozzle flow [1]. Shockwaves are a decidedly non-isentropic phenomenon that are associated with a drop in stagnation pressure and Mach number, with an increase in temperature, pressure, and entropy across a very short length. The following relations dictate the change in key parameters across a normal shockwave, with the subscripts B.S. and A.S. referring to before shock, and after shock, respectively: [1]

$$M_{A.S.} = \sqrt{\frac{\left(1 + \frac{(\gamma - 1)}{2} * M_{B.S.}^2\right)}{\gamma * M_{B.S.}^2 - \frac{(\gamma - 1)}{2}}} \tag{3.37}$$

$$\frac{P_{A.S.}}{P_{B.S.}} = 1 + \frac{2 * \gamma}{(\gamma + 1)} * (M_{B.S.}^2 - 1) \tag{3.38}$$

$$\frac{T_{A.S.}}{T_{B.S.}} = \left[1 + \frac{2 * \gamma}{(\gamma + 1)} * (M_{B.S.}^2 - 1)\right]\left[\frac{(2 + (\gamma - 1) * M_{B.S.}^2)}{(\gamma + 1) * M_{B.S.}^2}\right] \tag{3.39}$$

$$\frac{P_{0A.S.}}{P_{0B.S.}} = \frac{2}{(\gamma + 1) * \left(\gamma M_{B.S.}^2 - \frac{(\gamma - 1)}{2}\right)^{\left(\frac{1}{\gamma - 1}\right)}} * \left(\frac{\left[\frac{(\gamma + 1)}{2} * M_{B.S.}\right]^2}{\left(1 + \frac{(\gamma - 1)}{2} * M_{B.S.}^2\right)}\right)^{\frac{\gamma}{\gamma - 1}} \tag{3.40}$$

Normal shocks are assumed to be completely perpendicular to flow down the nozzle, and Eqs. (3.37-3.40) are easy to incorporate into the quasi 1-D nozzle approximation at a given longitudinal coordinate. After calculating the step displacements in pressure and the other parameters, the remainder of the nozzle is treated as a second isentropic expansion, which ends at updated nozzle outlet conditions [3]. Determination of the shock location, however, has no simple expression and can occur within a range of lengthwise locations. For the experimental testing carried out by this study, bell nozzle

tests that were identified as over-expanded with shockwave losses had the shock location specified to match the thrust output recorded by the load cell. While this approach puts a lot of stock in the load cell measurement, similarity over several tests in the specified shockwave location indicates some consistency and supports validity of the specified location.

3.5.2 Cone Nozzle Correction via Nozzle Discharge Coefficient

For ease of construction, USU bell nozzles are often constructed as conical nozzles, which have a linear area change from throat to exit. Idealized conical nozzles will have the same performance as a 1-D contoured bell nozzle with the same expansion ratio, but losses and reversibility result in reduced performance in practice. Established literature indicates a cone nozzle efficiency factor of 98% can be increased to 99.2% with a proper nozzle bell [3]. The nozzle discharge coefficient correction factor, λ_d, captures this loss based on the exit angle of the nozzle, θ_e: [3]

$$\lambda_d = \frac{1}{2} * (1 + \cos(\theta_e)) \tag{3.41}$$

$$F_{Cone\ Nozzle} = \lambda_d * \dot{m}_{exit} V_{exit} + (p_{exit} A_{exit} - p_\infty A_{exit}) \tag{3.42}$$

This nozzle correction is applied to the momentum thrust term of the rocket thrust equation, and can be used to reconcile the gains a bell nozzle would have over an experimental thrust generated by a conical nozzle.

3.5.3 Start-Up Transient Ignition Delay in Hybrid Motors

The thrust calculations of sections 3.3-3.4 can be made on an experimental data set for the total duration of a motor test. However, the models are only truly

representative of a fully ignited motor, with input chemical parameters assuming full combustion and nozzle calculations assuming a fully choked nozzle. These assumptions are accurate for a steady state motor, but may break down in the transient periods of motor start-up and tail-off. Usually, motor transients are exceedingly short and do little to affect mean calculations of thrust and I_{SP}. [30]

However, even a small ignition delay can affect mean properties if the motor burn time is short. For this study, test burns were conducted at a length of 1 second to avoid thermal degradation of the aerospike nozzle. Premature degradation of the aerospike could fundamentally alter the aerospike geometry and mask nozzle performance enhancement. While largely successful at avoiding premature nozzle destruction, the short burns were affected by an uncharacteristically slow ignition time in comparison to previous burns. Fig. 3.5 shows a chamber pressure comparison of the start-up time of this motor in comparison to a previous USU test: [31]

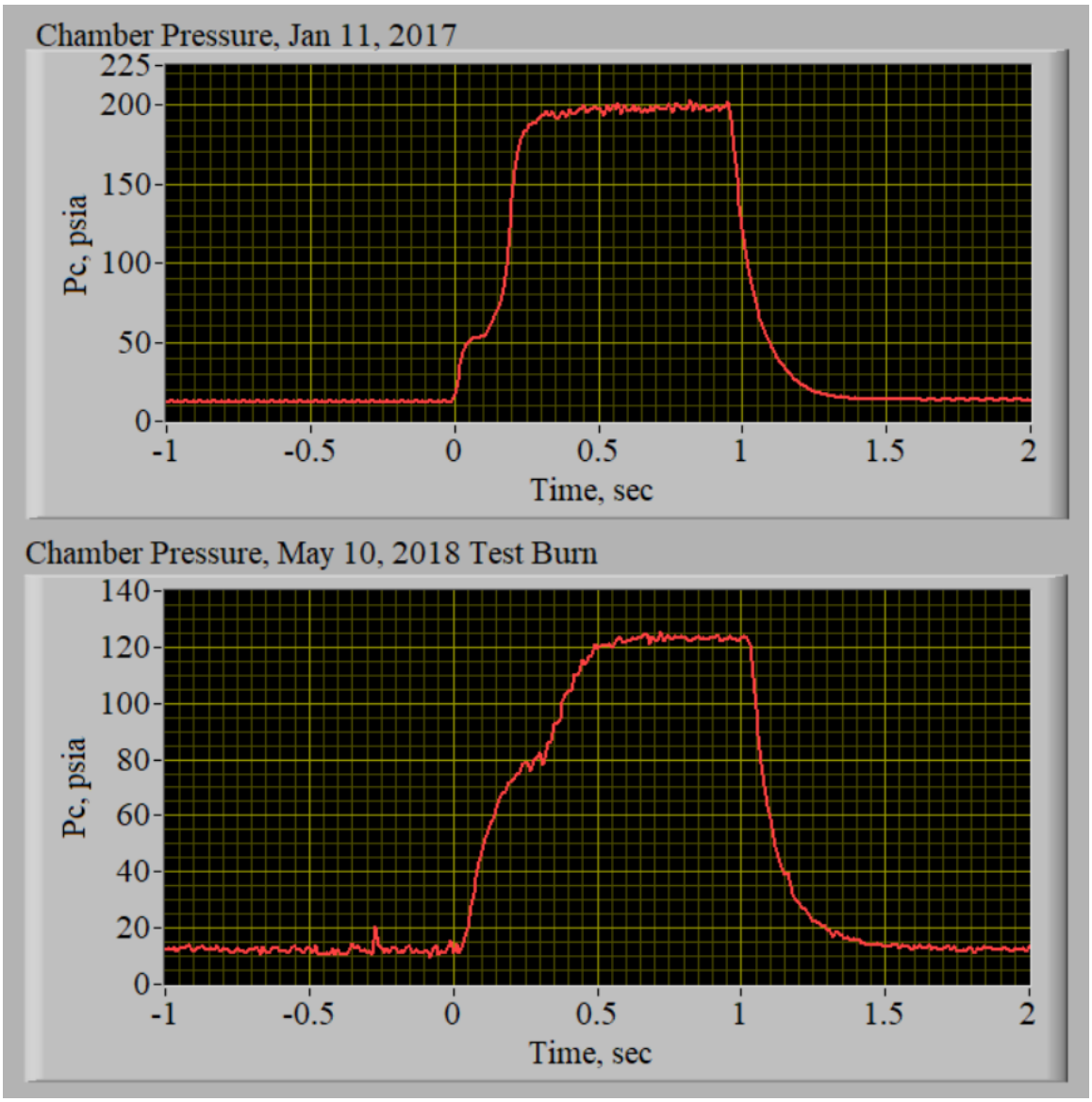

Figure 3.5. Typical chamber pressure (Pc) ignition transients. [31]

Both panels of Fig. 3.5 above attempted to initiate pyrolysis at 0 seconds, with the oxidizer run valve opening to allow GOX flow. In the top panel, the GOX successfully lights, reaching a steady state burn condition at around 195 psi chamber pressure within 0.2 seconds [31]. The motor configuration tested in this study, however, had intrinsic ignition delay. Steady state combustion is not achieved until nearly 0.5 seconds into the burn, with unlit GOX briefly driving the chamber pressure up to an intermediate cold-

flow pressure of around 80 psi. With nearly half the burn time exhibiting transient behavior, a mean I_{SP} calculation in the fashion of Eq. (1.6) would be indicative of the ignition behavior, as thrust will follow a similar profile to the chamber pressure. The cause of the ignition latency can be conjectured to be attributed to several factors that were changed in this study, namely the long length of the motor and higher pressure loss through the oxidizer injector.

In effect, more subtle I_{SP} changes brought on by switching nozzle geometry were found to be nearly negligible, or at least skewed, in the face of the large loss in performance due to the integrated transient thrust loss. Therefore, I_{SP} calculations were taken at a representative single point in time to capture the steady state performance. The time was selected to best represent thrust, which varies due to O/F shift and other irregularities, as a mean steady state value. Mass flow was obtained at the same instant, and an instantaneous value for I_{SP} was calculated via Eq. (1.5), providing an $I_{SP_{instantaneous}}$ value more representative of the steady state of the motor than a mean I_{SP} calculation.

3.5.4 Deconvolution of Chamber Pressure Signals

The above analyses are highly dependent on several precise experimental measurements. Previous testing has shown strong consistency in the differential venturi readings of $(P1, P2)$, but latency has been shown to be a known issue in the transducer measurements of chamber pressure, P_0 [34]. Using the deconvolution method of Whitmore, Wilson, and Eilers [34], an accurate reconstruction can be made to reflect true transient pressure behavior. The method is outlined completely in their 2010 journal

paper [34], and will be briefly summarized in the context of this study. Without this reconstruction, mean calculations of O/F were found to be divergent from measured experimental values.

Chamber pressure is a primary parameter of importance in chemical rocket performance. For hybrids, inspection of Eqs. (3.13-3.17), (3.21), and (3.32) shows that chamber pressure varies the motor mass flow, $\dot{m}_{total}$, O/F ratio, and thrust for both bell and aerospike nozzle configurations. All conclusions about motor performance rely on the accurate measurement of chamber pressure.

Due to complications arising from the hostile environment of the measured combustion chamber, pressure transducers are not commonly connected directly into the combustion chamber [34]. The motor case undergoes significant heat and forces loading during firing, both of which strain the motor and can physically deform a pressure transducer. Although temperature-adjusted pressure transducers are available, they are often expensive and distortion of sensed signals is still possible. Therefore, a common installation solution is to tap the motor with a small diameter port and connect the transducer with a small length of tubing. This has the effect of removing the transducer to a controlled temperature, and is easy to integrate into a variety of motor geometries. [34]

Although the installation scheme successfully avoids strain errors, separation of the transducer via tubing does bring in a small amount of acoustical distortion into play. Depending on the geometry of the tubing, pressure waves can be frictionally damped, resonate walls, and be reflected before being read by the transducer. A combination of these factors can result in false higher order harmonics, a time latency, and increased "noise" in the read pressure signal. When chamber pressure data was obtained for the test

burns of this study, many data sets exhibited a severe latency in the pressure signal. This latency was particularly visible in the tail-off of the motor depressurizing after GOX cutoff. Figure 3.6 shows a detailed time history of the motor tail-off. This feature is also highly visible in the chamber pressure time history traces presented by Figure 3.5.

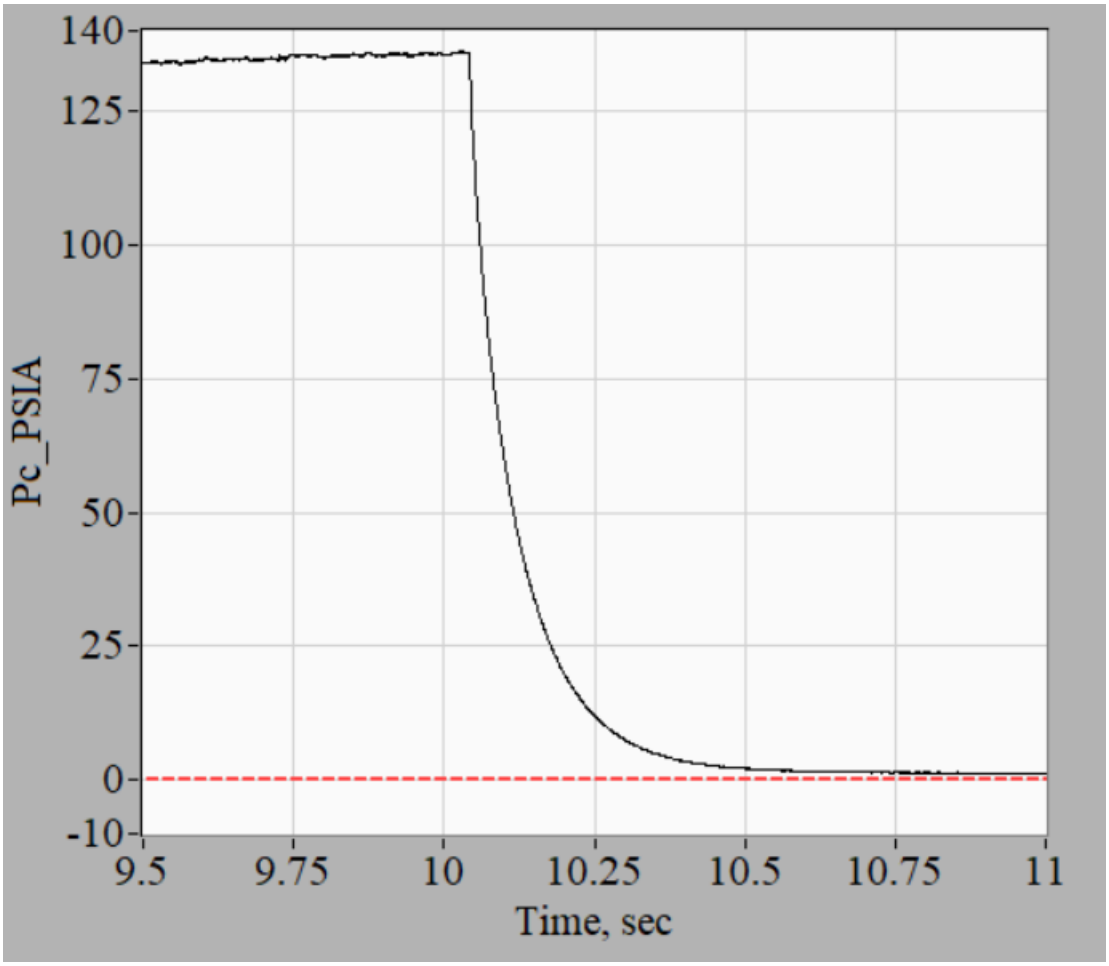

Figure 3.6. Hybrid motor depressurization tail-off.

Intuition suspected that the ~0.65 second depressurization of the motor was artificially long, and to confirm a theoretical approximation of the motor tail-off time was made. Depressurization of rocket combustion chambers is well established and studied, and the following method was taken from established literature [4]. A commonly used time constant, $\tau_{combustor}$, was calculated for the transient tail-off for each data set:

$$\tau_{combustor} = \frac{Vol_{combustor}}{A_t} * \frac{1}{\sqrt{\left(\gamma R_g T_0\right) * \left(\frac{2}{\gamma+1}\right)^{\frac{\gamma+1}{\gamma-1}}}} \tag{3.43}$$

$$P_0(t)_{tail\ off} = P_{0_{ss}} * e^{-\frac{(t_2-t_1)}{\tau_{combustor}}} \tag{3.44}$$

The combustor volume, $Vol_{combustor}$, was assumed to be a straight cylinder with averaged circular end areas, which were separately measured after each test. As summarized later in Tables 5.3 and 5.6, the time constant model showed quicker depressurization (on the scale of 1 millisecond) than any corresponding data sets tail-off time. This led credence to the suspicion that the recorded motor chamber pressure tail-off was artificially long, but as an additional check a quick calculation of pressure transducer delay was done to ensure natural damping in the tubing was not the sole cause of the delay. Previous studies at USU [35] made implementation of a simple transducer model straightforward.

The following second-order response model, developed by Whitmore and Fox, is a simplification of the commonly used method of Berg and Tijdeman for calculating the frequency response of pressure-sensing systems [35]. The method is outlined completely in their 2009 journal paper, and will be summarized in brief here [35]. Starting with writing boundary-value equations derived from the Navier-Stokes equations for unsteady flow, the solution of these equations describes the dynamics of the simplified cylindrical pressure transducer geometry shown in Fig. 3.7. The physical setup of the chamber pressure transducer, seen in Fig. 3.8, was adapted into this simplified model for the remainder of these reconstruction calculations.

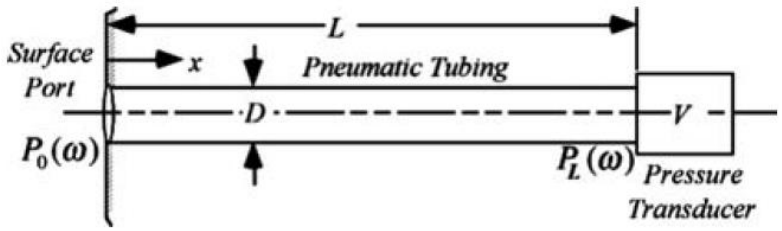

Figure 3.7. Schematic of idealized pressure sensor configuration. [35]

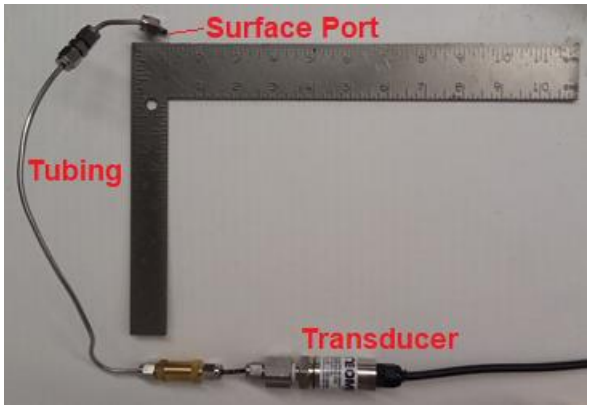

Figure 3.8. Physical chamber pressure transducer pneumatic tubing.

Table 3.1. Physical Chamber Pressure Transducer Geometry.

Geometry of Chamber Pressure Transducer	
Tubing Diameter, cm	0.175
Tubing Length, cm	45.0
Transducer cross-section, cm^2	0.312
Transducer Volume, cm^3	0.203

Analysis of the frequency response of the simplified geometry shows that a dominant harmonic exists that represents the primary pressure signal of interest, and thus Whitmore and Fox's reduction to a second-order time domain model comes about from truncation of higher order terms. The transfer function of the dominant harmonic, relating sensed pressure, $P_L(\omega)$, to input chamber pressure, $P_0(\omega)$, is written in the frequency domain in typical second order fashion with natural frequency, ω_n, and damping ratio, ς: [35]

$$\frac{P_L(\omega)}{P_0(\omega)} = \frac{\omega_n^2}{s^2 + 2\varsigma\omega_n + \omega_n^2} \tag{3.45}$$

The second order parameters of (ω_n, ς) are geometry dependent and can be determined for a specific system [35]. By manipulating the transfer function and applying the assumption of an isothermal expansion through the tube, the following time constant for delay in sensor response, τ_{Sensor}, can be written:

$$\tau_{Sensor} = \frac{128}{\xi} * \frac{\mu L_{Sensor}}{\pi D_{Sensor}^4 P_0}\left(Vol_{Sensor} + \frac{L_{Sensor} * A_{Sensor}}{2}\right) D_{Sensor} \tag{3.46}$$

Primarily obtained from sensor geometry parameters (Vol_{Sensor}, L_{Sensor}, A_{Sensor}, D_{Sensor}), the time lag is also dependent on the chamber pressure at time of motor cutoff, and fluid parameters (ξ, μ). Calculated time constants showed near instantaneous transducer response times for the experimentally determined data sets, on the scale of 1E-5 seconds for the test burn chamber pressure measurements. This further confirmed the existence of the artificial delay time present in the chamber pressure data, skewing all further calculations, and warranted reconstruction of the chamber pressure signals.

Reconstruction of latent pressure signals using a deconvolution algorithm has aligned well with experimental tests in previous studies [35]. The pressure measurement is modeled by a convolution equation which incorporates the simplified second order transducer model above:

$$P_L(t) = \int_0^t \upsilon_{conv}(t - \tau) * P_0(\tau) d\tau + \eta(t) \tag{3.47}$$

$$v_{conv}(t) = F^{-1}\left[\frac{\omega_n^2}{2i * \varsigma\omega_n * \omega + (\omega_n^2 - \omega^2)}\right] = F^{-1}(\Upsilon(\omega)) \tag{3.48}$$

where $F^{-1}$is the inverse Fourier transform operator. $\eta(t)$ represents the measurement noise function that accompanies physical measurements, and critical to the method is deconvoluting Eq. (3.47) without amplifying the system noise. This is done via an optimized filter of the form:

$$\hat{P}_0(\omega) = g(\omega)P_L(\omega) \tag{3.49}$$

$$J = E\left[\left\{\hat{P}_0(\omega) - P_0(\omega)\right\} * \left\{\hat{P}_0(\omega) - P_0(\omega)\right\}\right] \tag{3.50}$$

where $g(\omega)$ is calculated to minimize the cost functional J, which overall minimizes the effects of sensed pressure noise on the reconstructed pressure measurement [35]. For a specific data set, statistical parameters of sensed pressure variance, $\|P_{00}\|$, and pressure noise variance, $\|N\|$, can be calculated and after lengthy calculations the deconvoluted pressure model can be written:

$$\hat{P}_0(\omega) = \left\{\frac{\Upsilon(\omega) * \left(\frac{\|P_{00}\|^2}{\|N\|^2}\right)_\omega}{\|\Upsilon(\omega)\|^2 * \left(\frac{\|P_{00}\|^2}{\|N\|^2}\right)_\omega + 1}\right\} * P_L(\omega) \tag{3.51}$$

The deconvolution model can only be used to reconstruct a true pressure signal with knowledge of the second order parameters of (ω_n, ς). [35] Following previous work, these two parameters were tailored to each data set by use of a visual curve fit to match the tail-off of the recorded signal as if it were a second-order function. [35] With proper scaling for known fluid parameters, a corrected time constant could then be extracted using the form of Eq. (3.46). This process of curve fitting to fill in the second-order model parameters of Eq. (3.45) is shown in Fig. 3.9, where the final reconstructed

second order signal is also shown:

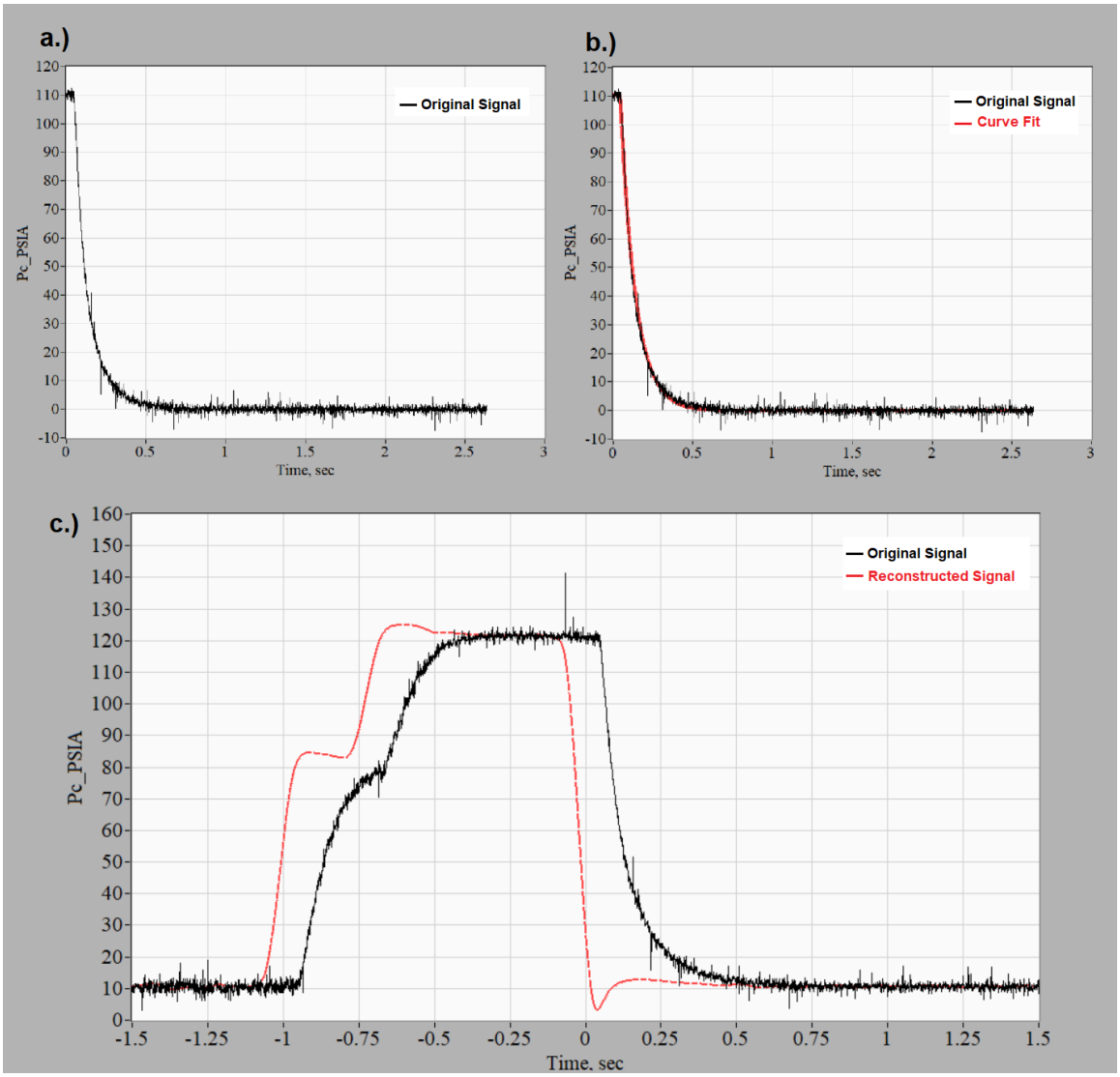

Figure 3.9. Curve fitting chamber pressure tail-off for signal reconstruction. *Clockwise from top, a.) Measured tail-off, b.) visually-adjusted curve fit to determine second order parameters, c.) Reconstruction of original pressure measurement using second-order model.*

Calculated time constants of the reconstructed signals are shorter and more closely match calculated theoretical motor time constants of Eq. (3.43). Furthermore, the large effect of steepening the slope of start-up and tail-off transients provided a much better approximation of the total mass flow, which is based off chamber pressure via Eq.

(3.15). Prior to the reconstruction, unrealistic O/F ratio values caused a large discrepancy in burnt fuel between calculated measurements and physical measurements of the fuel grain before and after burning. The reconstructed pressure signal brought the average fuel discrepancy from 2.17 grams down to 0.14 grams, an improvement of major significance considering burns consumed 4-6 grams of fuel. The improvement to the O/F ratio calculations led to the reconstruction being used on every test burn of this study; the time constant comparisons are tabulated in Chapter V. The time lag before deconstruction was visually determined for each data set, then contrasted with an easily calculated time lag constant, $\tau_{Tailoff}$, from the second order parameters:

$$\tau_{Tailoff} = \frac{2 * \varsigma}{\omega_n} \tag{3.52}$$

This definition of time constant, taken from Whitmore, Wilson and Eilers [34], can be shown to be identical to the specific formulation of Eq. (3.46). The simple Eq. (3.52) calculation was proved to be indicative of the physical time lag of the reconstructed signal, and in each case greatly reduced the time latency of the chamber pressure signal.

As to the cause of the latency, it is conjectured that good cleaning and thorough housekeeping during the tests could have potentially made the reconstruction unnecessary. The test assemblies had been in use for many months before the tests of this study, and a potential cause of latency could have been sooty particles blown into the transducer tubing and sensor volume. Enough particulates could have reduced the effective area of the pressure transducer tubing and subsequently greatly increased the response time of the transducer. This seems particularly likely given the fuel-rich behavior of the long motor case, and large amounts of sooty particulates were physically viewed in the plume during testing.

CHAPTER IV

EXPERIMENTAL SETUP

Previous USU hybrid motor data for conical bell nozzles existed, for several configurations, prior to the start of this testing campaign. One of these motors, dubbed micro-joe, was fitted into a commercial hobby rocketry case with an outer diameter of 1.5 inches with the intent of being sized for research into NanoSat propulsion. The manufacturer supplied dimensions of this aluminum Cesaroni® motor case is shown in Fig. 4.1. In this configuration previous testing resulted in motor performance data for a high expansion ratio cone nozzle of 8.5:1 in vacuum chamber tests; a low expansion ratio nozzle of 2:1 in vacuum chamber tests, and tests of a low expansion ratio nozzle of 2:1 at roughly 4800’ at the USU main campus in Logan, Utah. A 2:1 nozzle corresponds to the ideal design condition for these propellants at the Logan altitude, while in vacuum the lack of back pressure makes the design expansion ratio as high as feasibly achievable [30]. For contrast to the previous studies, 3 categories of tests needed to take place. First, a high expansion ratio test of an 8.5:1 nozzle had not been conducted at the relatively high pressure of USU’s altitude due to predicted performance loss from over-expansion. However, robustness in the over-expanded regime is one of the aerospike’s key areas of improvement over a bell nozzle. Therefore, it was desired to obtain over-expanded bell nozzle data for comparison. Next, to contrast with high expansion ratio data, similar aerospike testing needed to be conducted in both vacuum and at USU altitude. Not only would these tests be available for direct comparison to the bell nozzle tests, but also provide credence to the aerospike nozzle adapting over different pressure ratios. To accomplish these tests, two aerospike nozzles, a conical bell nozzle, and minor

integration hardware had to fabricated. Lack of vacuum chamber facilities necessitated conducting vacuum aerospike testing off-campus. Thanks to a cooperative agreement with Daniel P. Cavender of ER23 at NASA Marshall Spaceflight center, vacuum chamber facilities were made available, with much of the setup already in place.

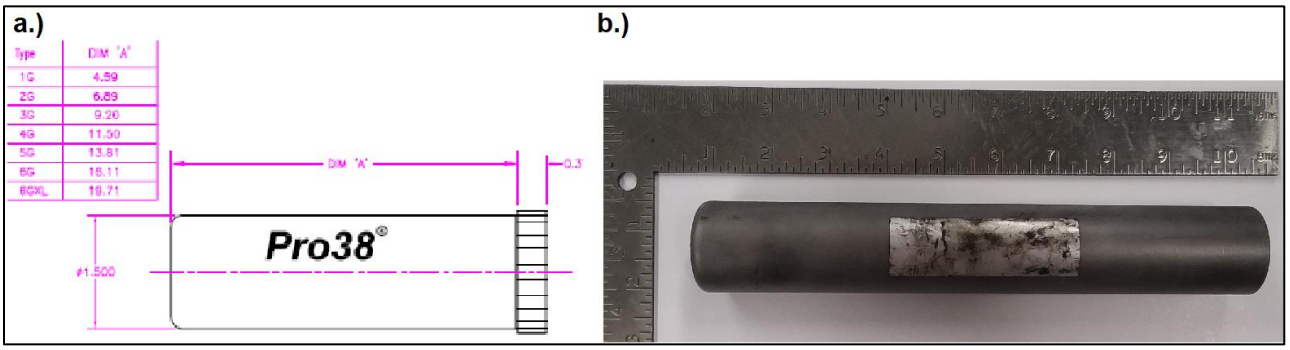

Figure 4.1. Product detail of Cesaroni Pro 38 motor case. [36] *a.) Manufacturer supplied Pro 38 motor case sizes schematic, b.) Physical motor case used, 9.2 inch "3G" variant.*

4.1 Nozzle Fabrication

Table 4.1: Current and Prior Test Nozzle Geometries.

Geometry of Tested Nozzles		
	8.5:1	**2:1**
Throat Diameter, in	11/64	11/64
Exit Diameter, in	1/2	0.2431
Aerospike Gap height, in	0.0055	N/A
Cone Exit Angle, ˚	14	5
Cone Nozzle Length, in	0.6580	0.7170
Aerospike Length, in	0.7600	N/A
Motor Case Diameter,in	1.5	1.5
Motor Case Length, in	9.2*	4.6

*One Exception- Burn 27 used the 4.6" Case

Table 4.1 presents a summary of critical geometry parameters for the nozzles tested in this study. For ease of construction, bell nozzles at USU are made as cone nozzles, with a simple linear expansion from throat to nozzle exit. This allows for

construction out of carbon graphite using a common shop lathe. Carbon graphite has been the nozzle material of choice for USU hybrid rocketry due to high thermal capacitance, relatively low cost, and sufficient structural robustness. Using the same process as previous USU studies [31], the conical nozzle was constructed to fit into an aluminum end piece, which bears the pressure load and attaches to the motor case with machined threads. The 8.5:1 high expansion ratio cone nozzle used in this study is shown in Fig. 4.2, and was built with a 14˚ nozzle exit angle.

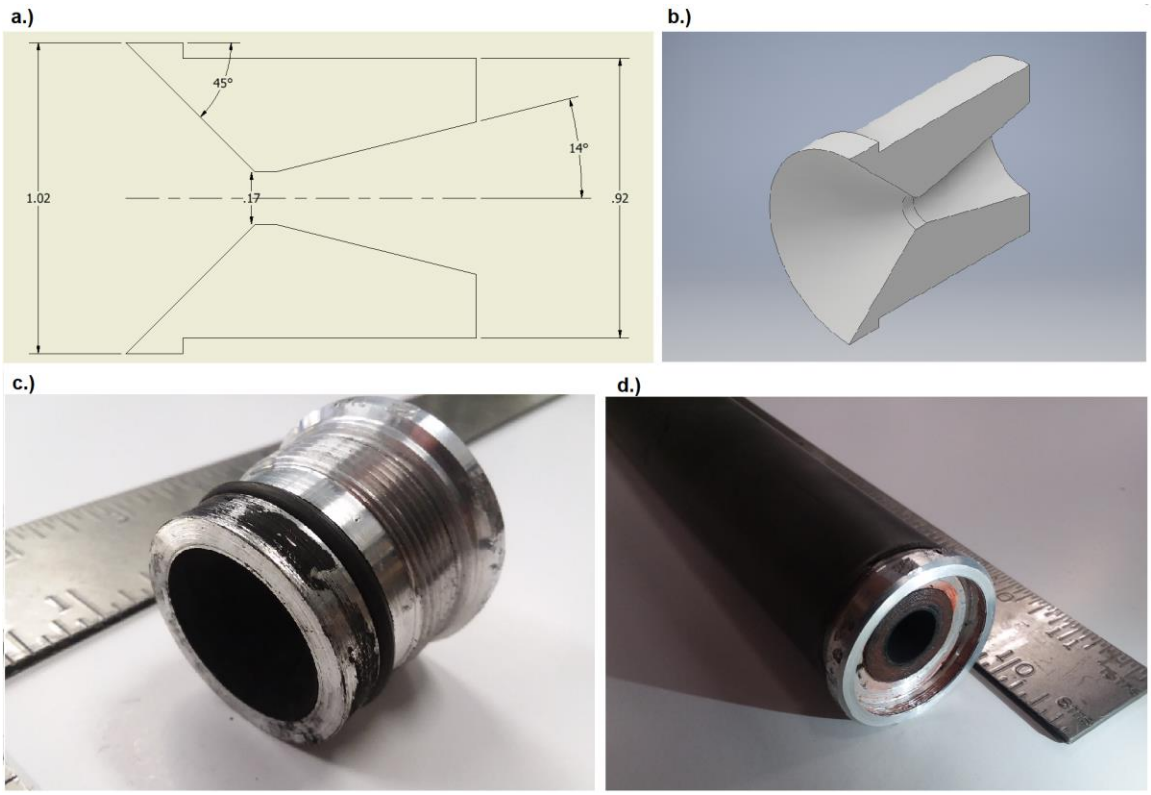

Figure 4.2. Fabricated cone nozzle geometry. *a.) 2D schematic showing cone angle, b.) Section view of carbon graphite cone nozzle, c.) Cone nozzle in aluminum end fixture, d.) Cone nozzle installed in motor case.*

A primary focus of this thesis was the inexpensive development of an aerospike nozzle to fit the 1.5 inch diameter motor case. 3D metal printing of an Inconel 718 aerospike was the first natural option to exhibit how modern manufacturing could create

an aerospike in ways not seen before. The M290 printer at NASA Marshall, however, had significant lead time before USU use, and scheduling constraints necessitated the construction of an aerospike by means of the CNC facilities at USU. Similar to the cone nozzle, the in-house CNC manufactured aerospike was machined from carbon graphite bar stock.

The design of the carbon aerospike needed to incorporate several simple but important features. The 4-axis CNC mill owned by the USU Mechanical & Aerospace Engineering department, operated by Terry Zollinger, is fully capable of carving precise curves, such as those needed for the spike contour. However, at the required sizing tolerances, manufacture of spike and cowl in one piece was impossible due to the required overhang at the nozzle throat. The cowl was machined from a separate ring of graphite to allow for machining of the all-important nozzle throat. The central spike is supported by three stainless steel pins, the placement of which sets the throat dimension in the longitudinal direction. The spike was machined from one piece of graphite bar stock. The profile of the drag-reducing Von Karman ogive on the upstream side of the central spike was of less importance to nozzle performance than the aerospike profile, so the spike was supported during machining by attachment to the raw bar stock on the Haack body side. After the profile had finished machining, this supporting attachment was broken off by hand, and then filed down to finish the Haack series profile. The spike was then placed in a 3D printed mold to hold it in place while holes were cut for the spike supports. The spike, pins and cowl were then all glued into place using RTV silicone adhesive. Similar to previous designs for the cone nozzles, the entire carbon assembly was then secured into a custom aluminum end piece with RTV. Figure 4.3 presents the

CAD model and physical components of this design.

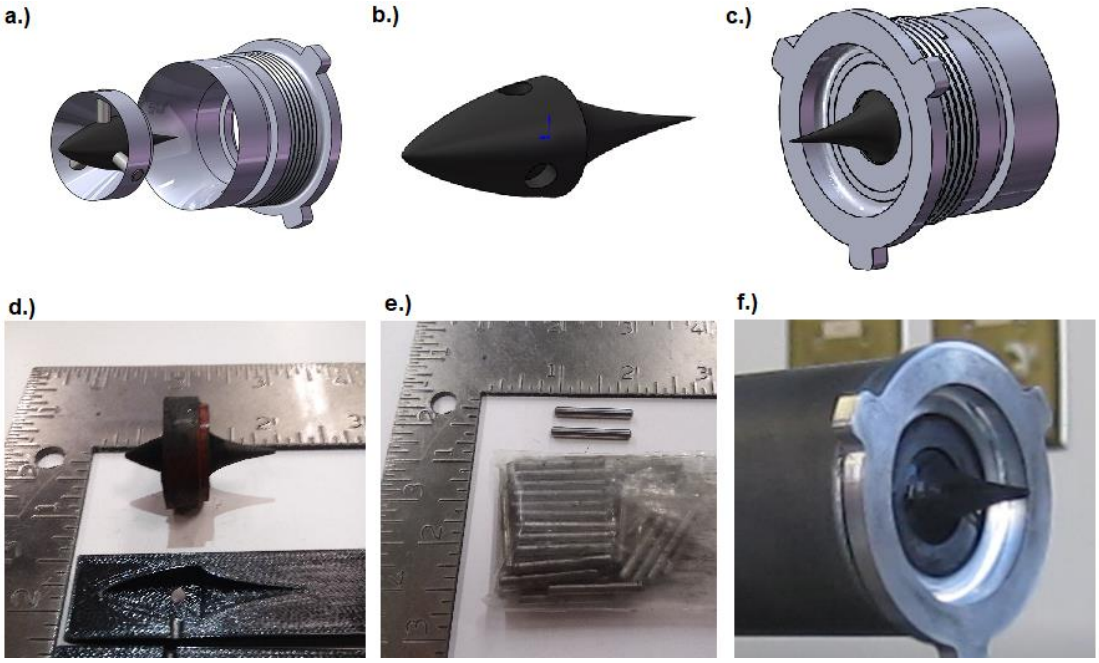

Figure 4.3. Design of carbon graphite aerospike. *a). Graphite spike assembly and aluminum end piece, b). CNC fabricated cantilevered spike contour, c). Full assembly CAD view, d). Graphite spike assembly., e). Stainless steel support arms, f). Picture of final nozzle assembly integration.*

While testing commenced of the carbon aerospike at the USU campus location, a spike of nearly identical dimensions was being 3D printed at NASA Marshall Space Flight Center. An initial one-piece design that could integrate into the same aluminum end piece was sent to NASA personnel, who then made minor changes to accommodate known build issues with the M290 printer. This primarily consisted of adding small support legs to ensure the aerospike did not collapse under its own weight while being printed. These supports were broken off after printing and smoothed by hand. The high tolerances of the M290 printer successfully fabricated the required aerospike geometry, which had no need for stainless steel supports and was secured into the aluminum end piece. The Inconel design, used for all vacuum testing in this study, initially had, for all practical purposes, an identical geometry to the carbon spike. The 3D printed aerospike is

shown in Fig. 4.4.

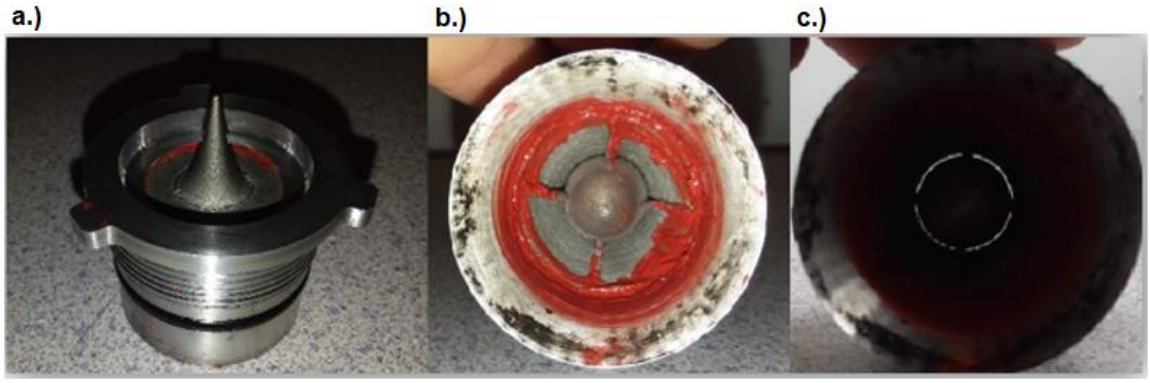

Figure 4.4. 3D printed one-piece Inconel aerospike. *a.) Printed aerospike, isometric view, b.) Printed aerospike, upstream cross-section, c.) Printed aerospike, upstream cross-section, illuminated throat area.*

4.2 Hybrid Motor Assembly

The Cesaroni motor case was the only motor case unused in the USU propulsion lab at the time of this study's testing, and at 9.2 inches in length was substantially longer than the 4.6 inch case used by Whitmore and Merkley [30]. Comparisons across different O/F ratios are possible through the calculations of section 3.2, yielding validity to the use of the 9.2 inch case. The ABS fuel grain design closely mimics previous successful designs. The USU patented arc-ignition system is implemented along a printed ABS spark cap, pictured in Fig. 4.5.

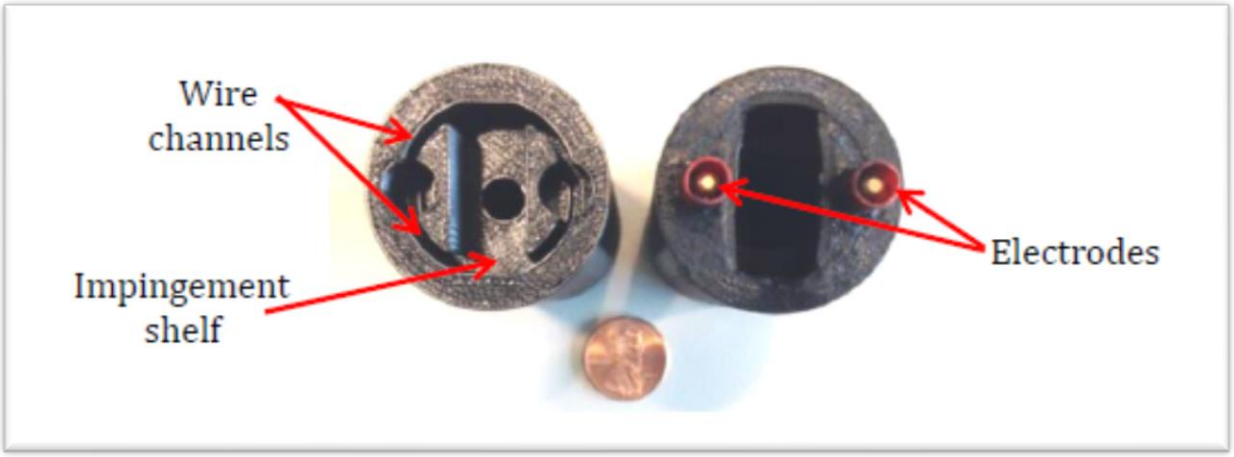

Figure 4.5. USU patented arc-ignition electrode design. [31]

In the additively manufactured spark cap architecture, two engrained wires are connected via commercial electrical components to the upstream injector hardware. The tips of the wires are separated along a roughly ¼ inch shelf, which provides the arcing surface, and has direct impingement from the oxidizer injection to ensure good mixing with sublimated fuel vapor. Over a burn lifetime, this fuel grain and spark cap are consumed, lasting a total of about 8 seconds in previous configurations [32]. Previous testing at this scale shows a required electrode configuration to supply a 1000 V difference at 8W to sustain vaporization [32]. The 8 inch fuel grain, made of extruded ABS bar stock with a machined cylindrical port starting at a 3/16 inch diameter is a topped by a ¾ inch 3D printed ABS spark cap architecture, making the fuel grain approximately 87% extruded ABS.

The injector cap, made of aluminum, is insulated against the electrodes so that the ignition spark does not conduct through the cap hardware. Unlike previous designs, the injector cap fabricated for this testing campaign also incorporated a ceramic shield, machined from Macor® machinable alumina, to help safeguard against ignition issues.

The injector cap must seal the upstream end of the motor case, but also provide passthroughs for oxidizer injection and a chamber pressure measurement. The ceramic shield therefore had several through-holes drilled into it, which precipitated thermal degradation over the 27 test burns. The injector cap dimensions and level of injector cap degradation at the conclusion of testing is shown in Fig. 4.6. Although the degradation did not adversely affect the oxidizer injection, it did perhaps negatively contribute to low combustion efficiency. The total USU ABS/GOX hybrid motor assembly, consisting of an ABS fuel grain, ABS spark cap, aluminum injector cap and the nozzle assembly is shown in Fig. 4.7.

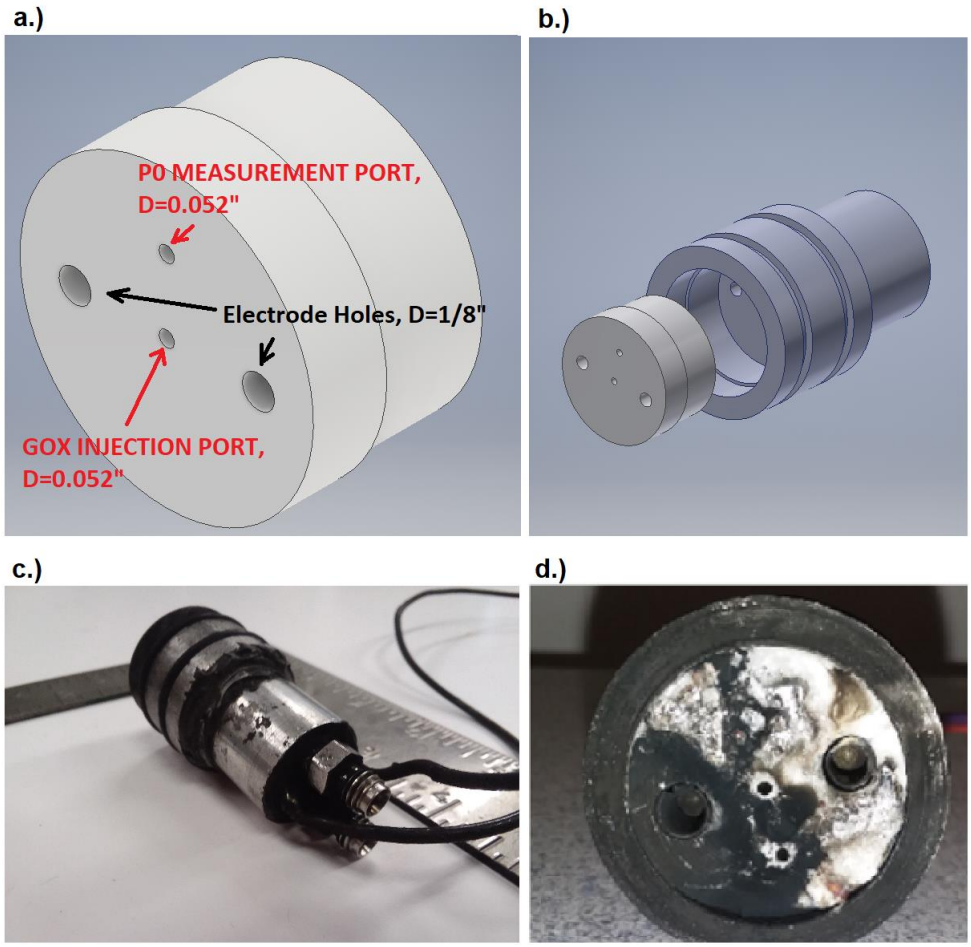

Figure 4.6. Oxidizer injector cap with ceramic insert. *a.) schematic of ceramic*

insert with through-ports, b.) detail of ceramic plug location, c.) completed injector cap assembly, d.) level of ceramic degradation after completion of test burns.

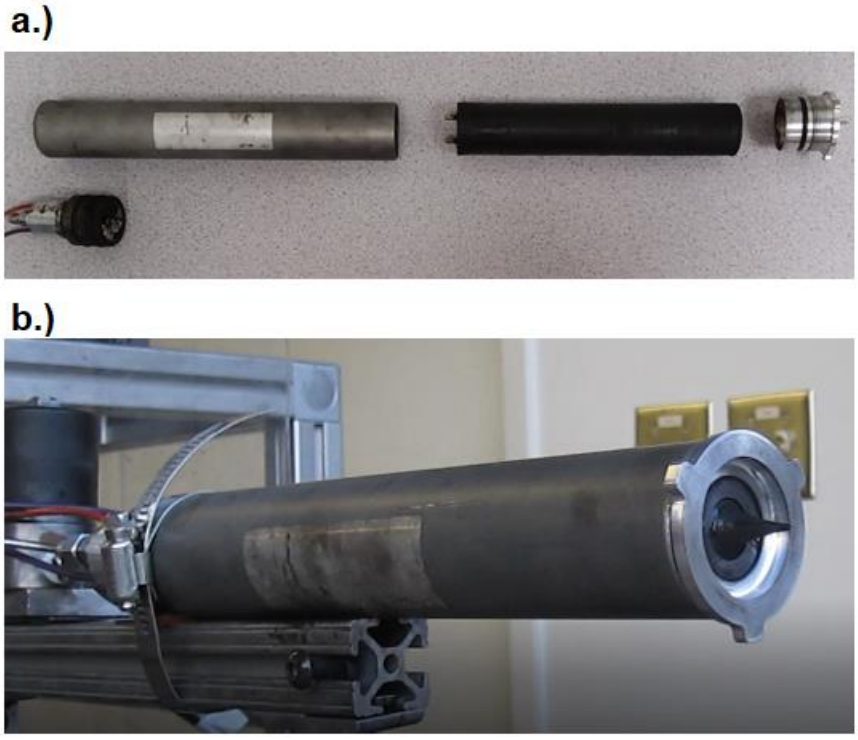

Figure 4.7. Hybrid motor components assembly. *a.) exploded view of motor assembly components, b.) complete motor assembly mounted on test cart.*

4.3 Hybrid Motor Test Facilities

To generate over-expanded and under-expanded data sets with the high expansion ratio nozzle of 8.5:1, testing was conducted in two locations with different background pressures. Testing occurred at the USU main campus in Logan, Utah where barometric pressure is on average around 12.28 psia, and at the vacuum chamber at NASA MSFC's Lab 104 of the In-Space Propulsion Department (ER23), which is able to generate pressures around 0.27 psia. The testing instrumentation and environment at the two locations took the same experimental measurements but differed in some of the physical equipment.

4.3.1 USU Hybrid Motor Test Facility

To generate thrust and I_{SP} data by the calculations outlined in Chapter III, pressure, temperature, and load cell measurements needed to made in a controlled manner. Previous research at USU by Whitmore and Merkley [30], and M. Bulcher [32], had designed a test cart for the micro-joe sized hybrid thruster. Figure 4.8 shows the piping and instrumentation diagram (P&ID) of this testing cart. Figures 4.9.1. through 4.9.3 present physical pictures of the test apparatus.

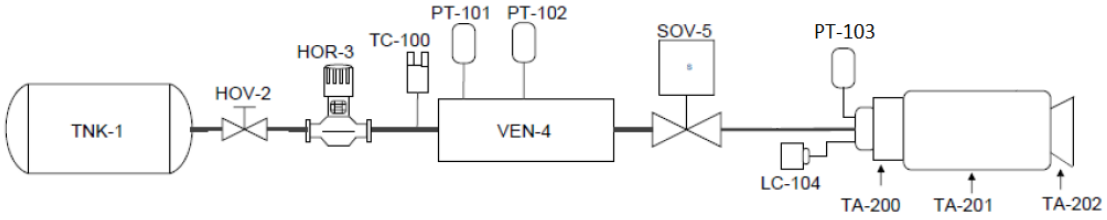

GOX Components	Functional Description
TNK-1	GOX supply tank (2000psi)
HOV-2	GOX supply on/off hand-operated valve
HOR-3	GOX hand-operated pressure reducing regulator
VEN-4	GOX Venturi flow meter
SOV-5	GOX solenoid run valve

Sensors	Functional Description
TC-100	Venturi inlet temperature
PT-101	Venturi inlet pressure
PT-102	Venturi differential pressure
PT-103	Combustion chamber pressure
LC-104	Thrust stand load cell

Test Article	Functional Description
TA-200	GOX injector cap
TA-201	Motor case
TA-202	Nozzle cap

Acronyms
- TNK: tank
- HOV: hand-operated valve
- HOR: hand-operated regulator
- VEN: Venturi flow meter
- SOV: solenoid valve
- TA: test article
- TC: thermocouple
- PT: pressure transducer
- LC: load cell

Figure 4.8. P&ID of the micro-joe demonstration test cart at USU. [32]

Table 4.2: USU Instrumentation List.

TEST CART INSTRUMENTS	
Chamber	Omega PX309-300GV
Venturi Inlet	Omega PX35D0-500GV
Venturi Throat	PX409-015DDUV
Load Cell	Omega LCCA 25 Lbf
Thermocouple	Type K

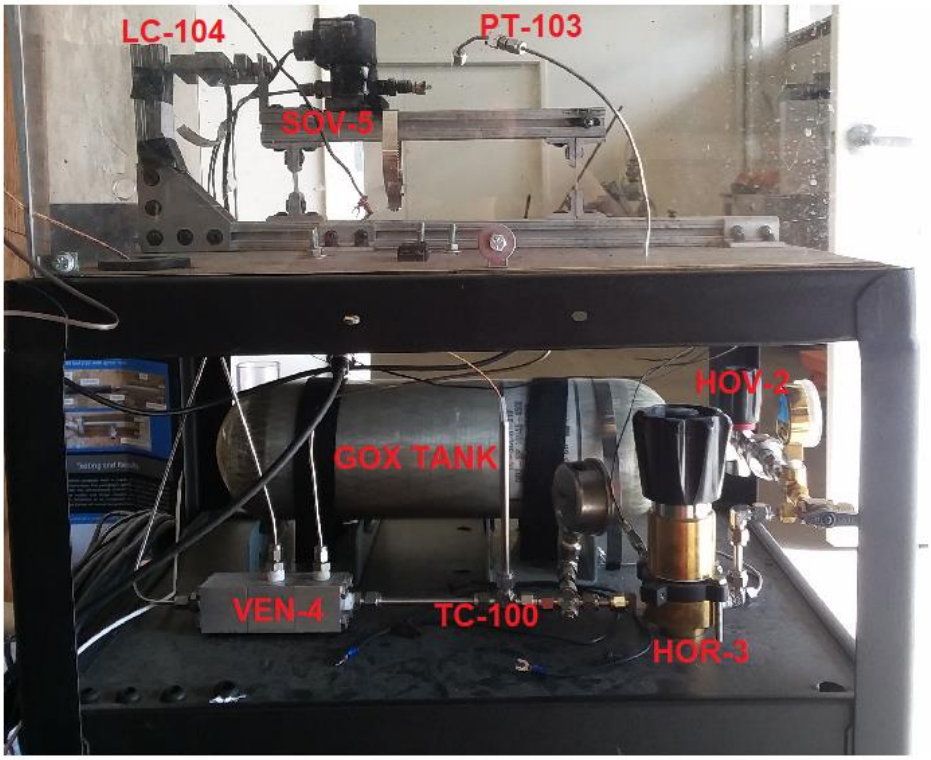

Figure 4.9.1. USU test cart hardware layout. [32]

Figure 4.9.2. Top view of USU circuitry pallet. [32]

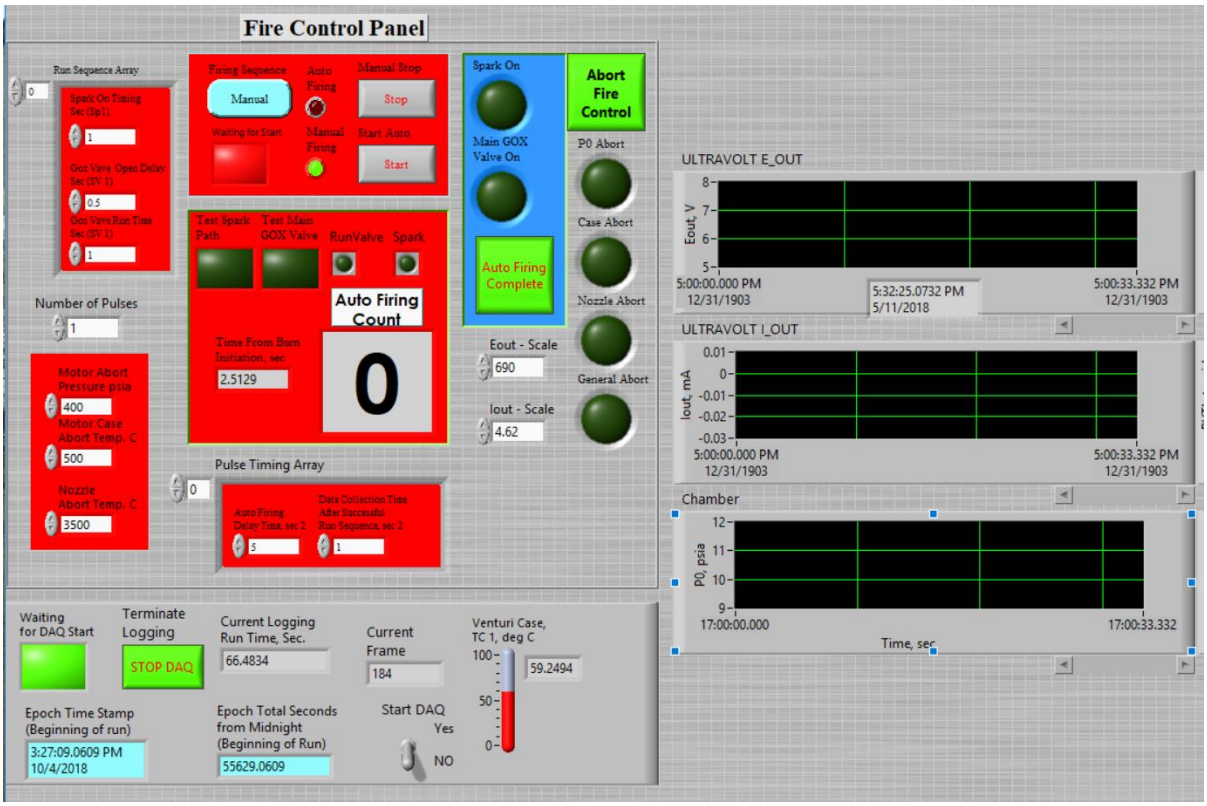

Figure 4.9.3. LabView Control Program Interface.

As can be seen in Fig. 4.9.1 above, GOX oxidizer is stored in a composite tank underneath the test deck. The tank pressure is monitored by visual dials prior to and after a pressure regulator, which takes down the pressure in the line to the test's required injection pressure. The GOX line then passes through a venturi flowmeter with an area ratio of 5 to obtain the oxidizer mass flow rate. Downstream of the venturi, the GOX flow is controlled by the main run valve, located on the test sled that is intended to capture all the thrust generated by the thruster. Pipe fittings connect the GOX line and chamber pressure transducer to the assembled thruster via the igniter cap, and the thruster assembly is then fastened in place.

Monitoring and control of the USU testing system is accomplished through NI Labview software. NI Data Acquisition Units, or DAQs, are an easy to integrate

commercial product line that contain internal circuitry and logic gates to create and receive analog and digital measurement signals. Two DAQs were used in the circuitry of the USU test cart. An NI 6002 DAQ was used to process analog signals from the venturi transducers and load cell. An NI 6009 DAQ was used to obtain the venturi thermocouple measurement, chamber pressure transducer measurement, and control the main run solenoid. Additionally, the NI 6009 triggered the arc-ignition system by providing the digital activation signal to an UltraVolt 1AA24-P30 high voltage power supply, which supplies the 1000 V electrical potential required for arc-ignition. The DAQs are connected via USB cables to the control computer, which can be any laptop that has the correct LabView Virtual Instrument(VI) program installed. Many different iterations of the control program have been utilized in the USU propulsion program over the years, and this study's requirements required no changes to the existing control program. After a successful test run, raw data is stored in a LabView output file, to be processed through the calculations of Chapter III at a later time.

4.3.2 NASA MSFC Hybrid Motor Test Facility

The experimental setup at NASA Marshall consisted of instrumentation to achieve the same measurements as those conducted at USU, along with those additionally needed to monitor the behavior of the vacuum chamber. The vacuum chamber had already been used for generating near vacuum data (~0.27 psia back pressure) for previous USU 8.5:1 high expansion ratio cone testing. The system was largely designed and built by Kevin Pedersen of ER23. Marshall's stricter requirements for using GOX facilitated enhanced safety features, such as pressure relief valves, in the NASA

instrumentation system. Functionally, the calibrated load cells, transducers, and thermocouples were all set up to provide the same measurements as the USU setup. All instrumentation wiring had to pass through the walls of the vacuum chamber to connect the data acquisition circuitry and computers to the test stand. Figure 4.10 shows the empty vacuum chamber loaned by ER23. Figure 4.11 shows the same chamber after a particulate-generating test burn.

Figure 4.10. Exterior of NASA MSFC ER23 vacuum chamber.

Figure 4.11. Interior of NASA MSFC ER23 vacuum chamber.

The vacuum chamber, used to produce near-space pressure levels, is about 4.5 ft^3 in volume. The chamber is evacuated by a rotary vacuum pump, and can be purged with 125 psia high purity air via HOV-ROV-11. The mini-test stand inside the vacuum chamber was designed to flex in the same way as the USU test stand, with load cell LC-404 placed to capture the majority of generated thrust. Although supporting piping differed outside the vacuum chamber, the chamber pressure measurement was made through the same port in the injector cap. Figure 4.12 shows a closer detail of the miniature test stand fitted inside the ER23 vacuum chamber.

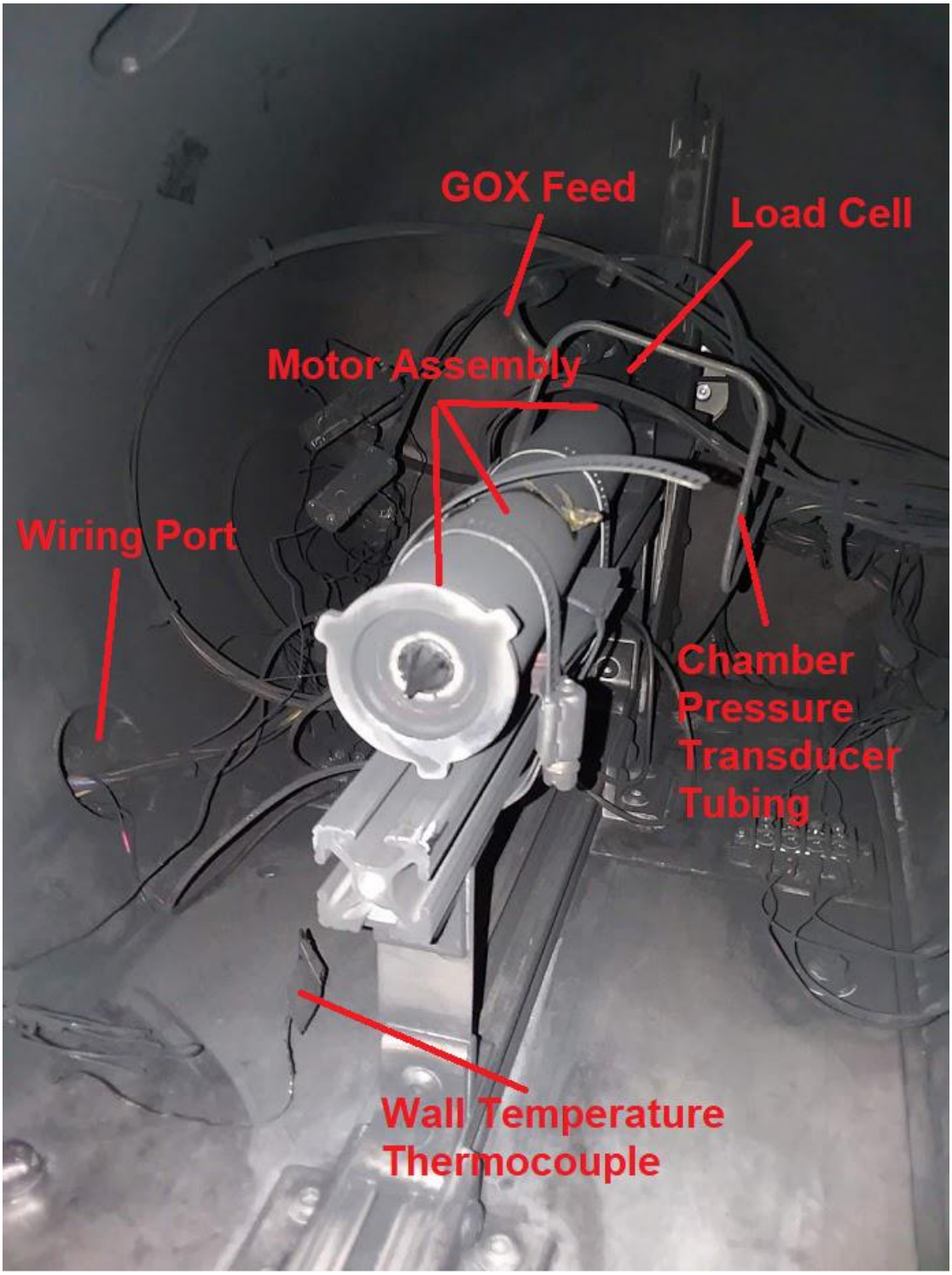

Figure 4.12. NASA MSFC miniature test stand.

Figure 4.13 provides details of the relatively complex vacuum chamber piping

systems, including the nitrogen pressurization system and oxidizer delivery system. The figure uses the same naming convention as Fig. 4.8, and shows the location of applicable instrumentation.

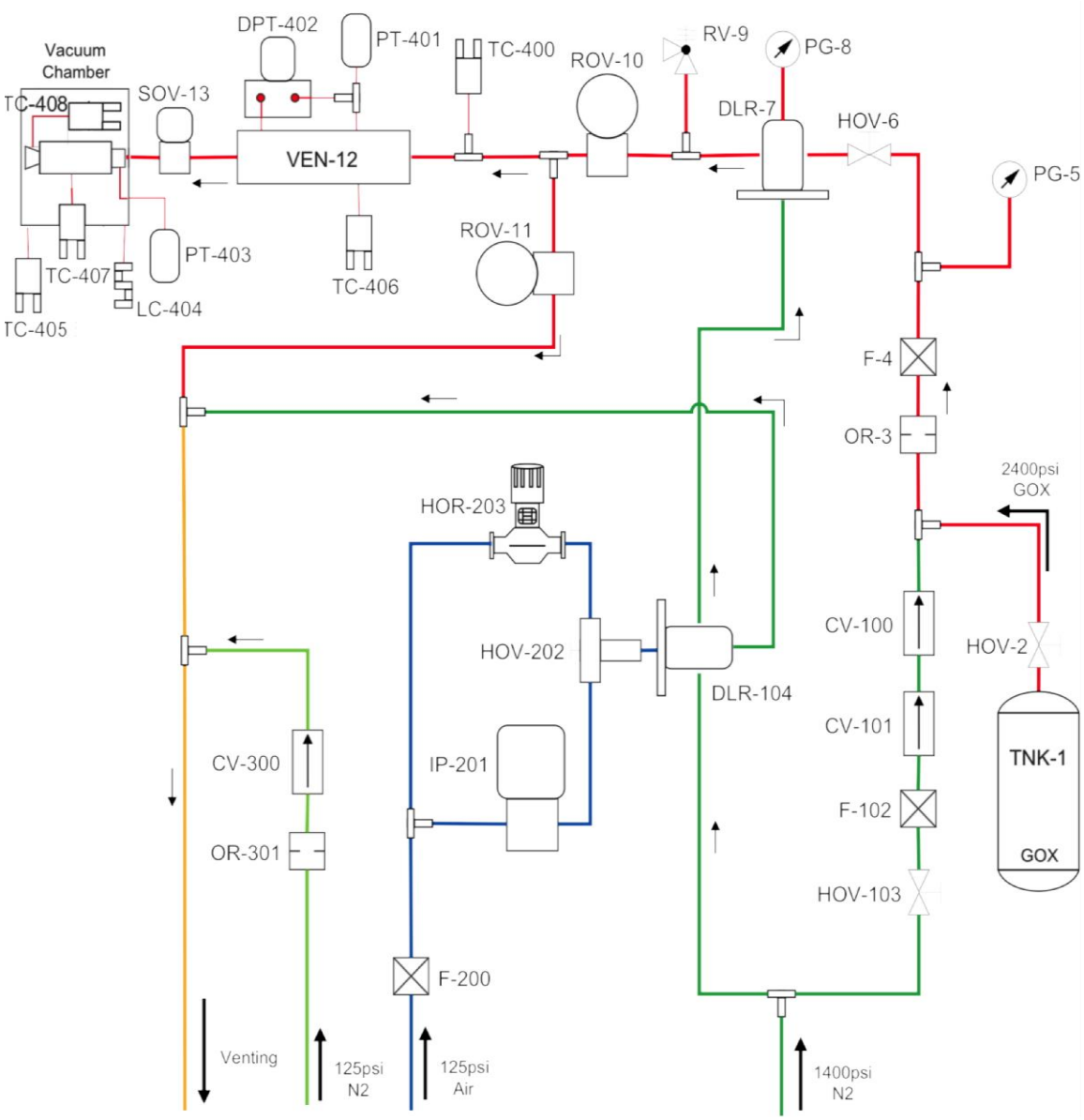

Figure 4.13. P&ID of NASA MSFC vacuum chamber system. [37]

Previous USU studies that utilized the ER23 vacuum chamber built the test stand,

supporting circuitry, instrumentation, and hardware integration to support ABS/GOX hybrid motor testing in this location. Aerospike testing only required a minor piping adjustment to incorporate the longer-than-previous motor case. A final report of test stand construction, compiled by Whitmore and Merkley in 2016 [37], described the fabricated test system in detail, and is summarized (and taken from) for the following descriptions.

As mentioned above, additional safety requirements necessitated a more complex oxidizer feed system. A separate inert pressurization system was used to regulate the oxidizer feed to the desired thruster injector pressure. The three-stage system consists of a low pressure (125 psig) air-feed that provides the dome-regulator a high-pressure (max 1400 psig) nitrogen gas (GN2) system, that in turn provides the dome control input for the GOX feed system regulator. The three-stage system is necessary to allow the regulated pressure to be controlled remotely with the vacuum chamber test cell blast-door closed. The facility 125 psig high purity air supply line was used for actuating the remote valves and is isolated from the GN2 propellant pressurization system. Regulators IP-201 and HR-203 supply the low-pressure air dome control for the second stage dome-loaded regulator DLR-104. Regulator DLR-104 supplies the high pressure GN2-dome control input to GOX dome-loaded regulator DLR-7. A GN2 purge line is teed into the GOX feed line and flow is initiated via HOV-103. Dual-redundant check valves CV-100 and CV-101, downstream of GN2 manual valve HOV-103, preclude the high-pressure GOX (max 2400 psig) flow from entering the GN2 intermediate-stage pressurization system. As a final safeguard, check-valve CV-300 prevents GN2 from entering the high purity air system [37].

Oxidizer delivery, regulated by the pressurization system, was monitored by a

venturi flow meter of the same type used at USU, with associated pressure transducers PT-401 and DPT-402. The GOX storage tank is isolated from the thruster with SOV-13, a remote operated solenoid valve, and hand valves HOV-6, and HOV-2. The chamber pressure transducer PT-403 is installed via 1/8 inch stainless line into the motor cap and measures the motor head-end combustion pressure. When the hand operated isolation valves (HOV-2, HOV-6) are opened, two additional remotely operated valves ROV-10 and SOV-13 isolate the GOX feed from the motor combustion chamber. The upstream pneumatic valve ROV-10 allows the system to be remotely pressurized prior to initiating the run-sequence via SOV-13 [37]. The remotely operated solenoid valve SOV-13, initiates the oxidizer flow into the thrust chamber and serves as the "run valve" for the system. The venturi pressure measurement via PT-401 is used to judge if the system is fully pressurized and ready for opening of the GOX run valve. The third-stage dome-loaded regulator DLR-7 sets the desired inlet pressure to the thruster injector. The output from DLR-7 is controlled by the dome-inputs from DLR-104 and the output difference between IP-201 and HOR-203. The firing-systems control software sets the commanded current input to IP-201. In accordance with NASA regulations, all piping experiencing GOX flow were precision cleaned. RV-9, a 500 psig pressure relief valve, is also installed on the GOX feed line as an additional safeguard [37].

Similar to the USU system, the piping systems were controlled via a mix of remotely operated hardware operated with a LabView interface, and some hand operated elements. Figure 4.14 and Figure 4.15 show the circuitry pallet used for the remote operated components, as well as data acquisition. However, location of the control computer required a wiring interface to a black wiring cabinet as well. Figures 4.16 and

4.17 show the added circuitry elements that allow final connection to the LabView control computers.

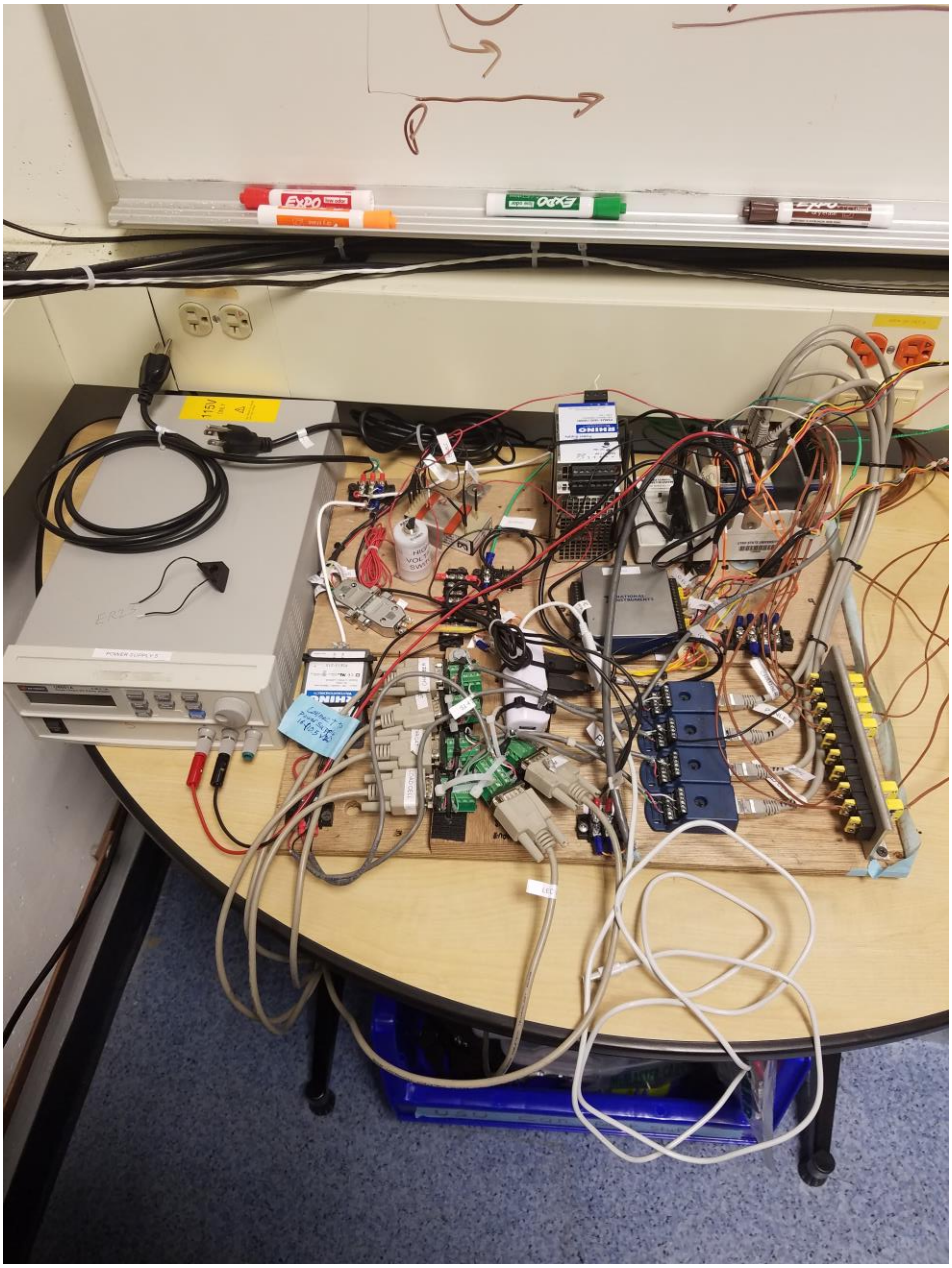

Figure 4.14. MSFC test circuitry pallet. [37]

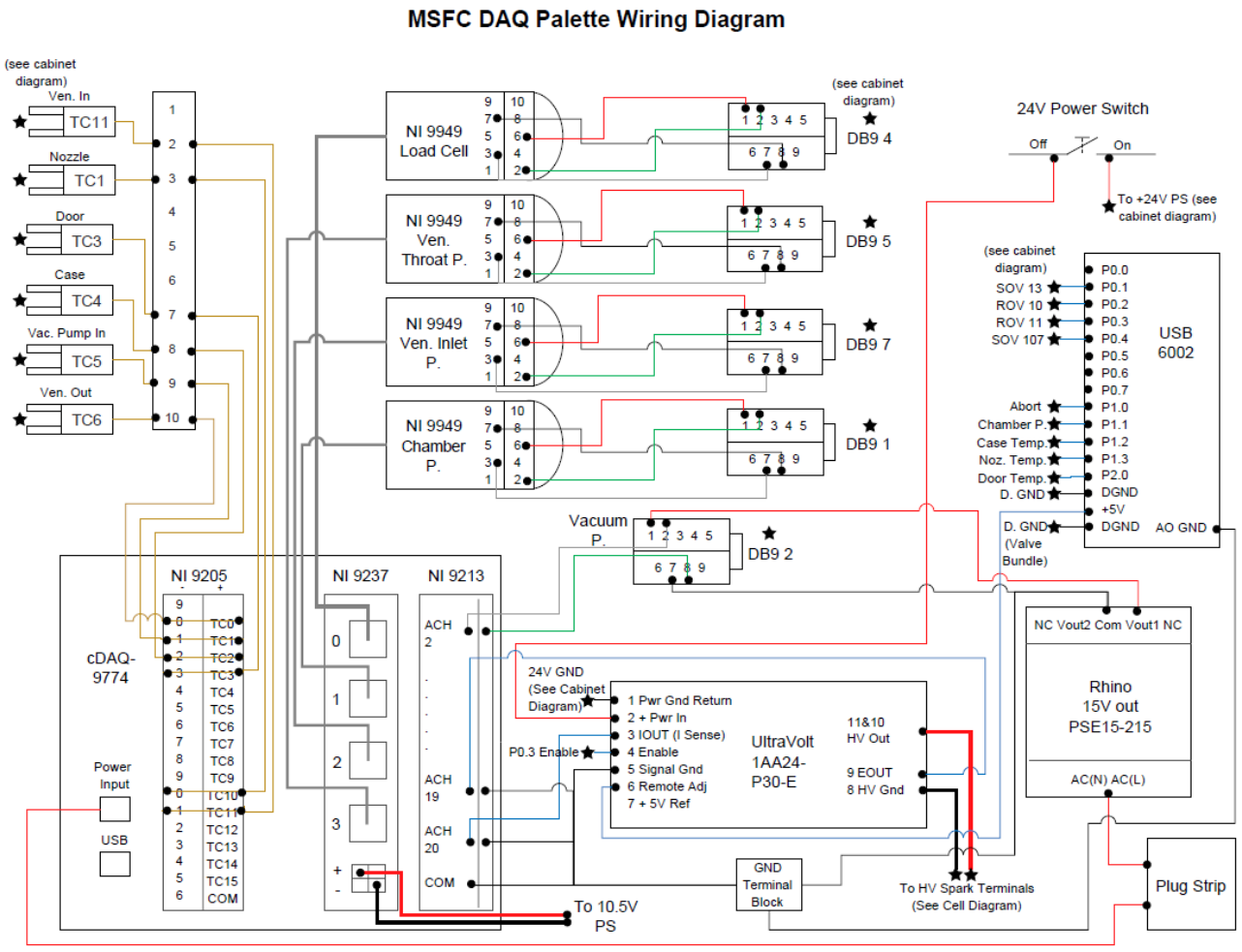

Figure 4.15. Associated pallet wiring diagram.

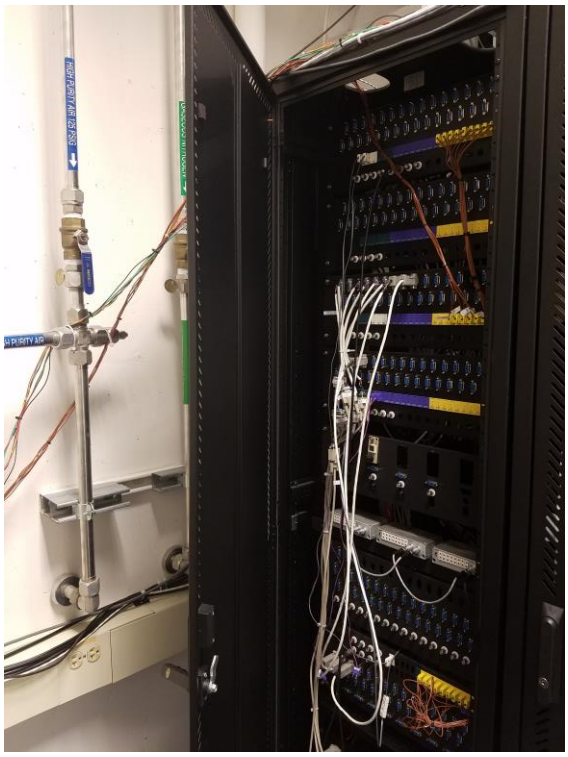

Figure 4.16. Black cabinet wiring board.

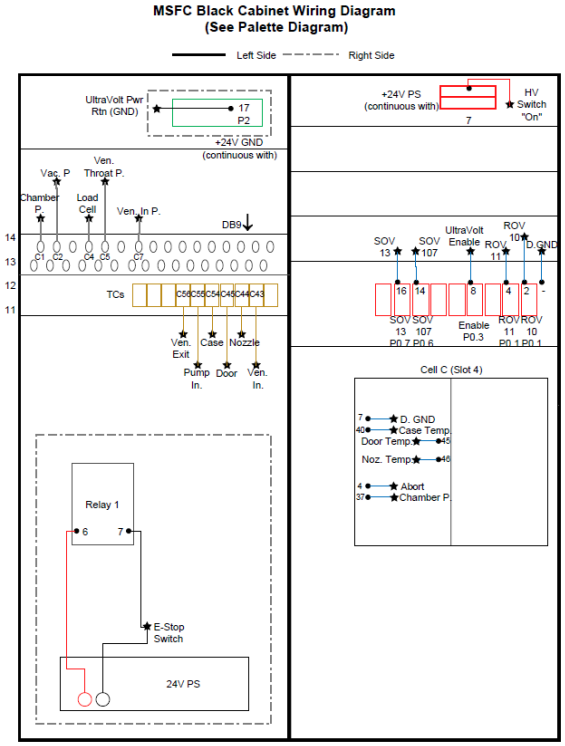

Figure 4.17. Black cabinet wiring diagram.

Needless to say, the above setup required a lengthier process than required at USU to setup the motor, depressurize the vacuum chamber, conduct a remote test, and re-pressurize before examining the test article. Visibility was very limited, through only a 3 inch viewing port, and testing was reliant on the real-time measurements of the LabView control VI. Once again to meet NASA requirements, the control VI was separated from the data acquisition VI, unlike the USU VI, and necessitated the use of two computers. Nearly identical to the interface seen in Fig. 4.9.3, once again no changes to the control software were needed to complete this testing campaign.

CHAPTER V

RESULTS

Utilizing the experimental test carts at USU and NASA Marshall, three distinct sets of test runs were conducted, each characterized by a different nozzle. With the inclusion previous USU results, these tests completed a desired testing matrix for the 1.5 inch diameter micro-joe test motor with a low-expansion ratio cone nozzle, high-expansion ratio cone nozzle, and high-expansion ratio aerospike nozzle at both Logan, Utah altitude (~4800') and vacuum conditions. To make sense of the small experimental sizes, a student-T distribution was calculated for all I_{SP} trends, to within a 95% confidence interval.

5.1 Over-Expanded Cone Nozzle Tests (USU Campus, Logan, Utah)

A total of 10 tests were conducted with the 8.5:1 expansion ratio conical nozzle at the USU testing location. With ambient pressure at around 12.28 psia, the nozzle was expected to be over-expanded. Thrust and I_{SP} were found using the method of section 3.3 with the addition of the normal shockwave model of section 5.5.1. Half the tests were conducted at an injector pressure of 305 psia, while the other five burns were conducted at a lower injector pressure of 228 psia. Due to the potential for premature thermal degradation in aerospike tests, these cone burns were also kept below a length of one second. This was sufficient time to see full, steady state combustion in the motor for all but one attempted test. Determination of long depressurization latencies led to the chamber pressure reconstruction being calculated for all the cone nozzle tests. The summary of the conical burns, which took place on May 10th and 11th, 2018, is shown in

Table 5.1, with a student-t distribution calculated to a 95% confidence interval. Table 5.2 shows the calculated performance parameters separately from sensed data. Several time constants were calculated for each burn to justify reconstruction of the chamber pressure, as summarized in Table 5.3.

Table 5.1. Summary of Logan Cone Nozzle Test Parameters.

BURN # (Grain #)	Initial Fuel Port Diameter, in. (Final)	Burn time, s	Injector Pf, psia	Chamber P0, psia	Total Mass flow, g/s	Fuel Mass Burned, g	Combustion Efficiency	Mean O/F Ratio	Shock Wave Location in Nozzle, %
1 (1)	0.301 (0.326)	0.90	305	122	7.7	3.30	0.99	0.9	81
2 (1)	0.326 (0.3725)	0.96	308	127.5	7.9	3.51	0.99	0.89	83
3 (1)	0.3725 (0.380)	0.75	309	126	8.15	1.63	0.96	0.94	81
4 (1)	0.380 (0.395)	0.68	308	122	8.5	1.56	0.96	0.82	81
5 (1)	0.395 (0.400)	0.85	229	100	7.0	1.8	0.99	0.54	76
6 (1)	0.400 (0.428)	0.92	225	97	5.8	2.17	0.98	1.1	76
7 (1)	0.428 (0.435)	0.90	229	96	6.5	1.73	0.99	0.71	76
8 (1)	0.435 (0.454)	0.76	228	96	6.4	1.54	0.94	0.94	77
10 (1)	0.463 (0.480)	0.95	309	135	9.1	2.84	0.99	0.65	85
High Pressure MEAN: (Std. Dev.)	**N/A**	**0.85 (0.117)**	**307.8 (1.470)**	**126.5 (4.775)**	**3.77 (0.426)**	**(0. 2.57 824)**	**0.98 (0.015)**	**0.84 (0.103)**	**82 (1.600)**
High Pressure Student-T (95%)	**N/A**	**0.85 ±0.087**	**307.8 ±1.130**	**126.5 ±3.670**	**3.77 ±0.379**	**2.57 ±0.633**	**0.98 ±0.011**	**0.84 ±0.079**	**82 ±1.230**
Low Pressure MEAN: (Std. Dev.)	**N/A**	**0.8575 (0.062)**	**227.75 (1.639)**	**97.25 (1.639)**	**2.93 (0.379)**	**1.81 (0.229)**	**0.98 (0.021)**	**0.8225 (0.214)**	**76 (1.230)**
Low Pressure Student-T (95%)	**N/A**	**0.8575 ±0.048**	**227.75 ±1.260**	**97.25 ±1.260**	**2.93 ±0.328**	**1.81 ±0.176**	**0.98 ±0.016**	**0.8225 ±0.165**	**76 ±0.333**

Table 5.2. Performance Parameters for Logan Cone Nozzle Tests.

BURN # (Grain #)	Load Cell Thrust, N	Steady State ISP, seconds	Bell Nozzle Corrected ISP, seconds
1 (1)	14.1	189.275	192.213
2 (1)	14.5	190.6135	192.824
3 (1)	14.8	183.025	187.218
4 (1)	14.8	181.4	183.6815
5 (1)	10.7	158.8	160.96
6 (1)	10.5	185.7	188.0015
7 (1)	10.7	163.8	167.9
8 (1)	10.3	158.3	162.5435
10 (1)	15.2	188.2	171.1
High Pressure MEAN: (Std. Dev)	**14.7 (0.366)**	**182.1 (3.622)**	**185.4 (7.903)**
High Pressure Student-T (95%)	**14.7 ±0.281**	**182.1 ±2.784**	**185.4 ±6.074**
Low Pressure MEAN: (Std. Dev)	**10.5 (0.166)**	**166.7 (11.207)**	**169.9 (10.790)**
Low Pressure Student-T (95%)	**10.5 ±0.127**	**166.7 ±8.614**	**169.9 ±8.294**

Table 5.3. Time Lag Comparison for Logan Cone Nozzle Tests.

BURN # (Grain #)	$\tau_{combustor}$, seconds	τ_{Sensor}, seconds	Time Lag, seconds (Pre-reconstruction)	$\tau_{Tailoff}$, seconds (Post-reconstruction)
1 (1)	0.000960648	8.72E-05	0.425	0.0972222
2 (1)	0.00124237	8.36E-05	0.415	0.0972222
3 (1)	0.000988186	8.19E-05	0.525	0.0947368
4 (1)	0.0014939	7.87E-05	0.525	0.0884354
5 (1)	0.00165011	9.37E-05	0.500	0.1
6 (1)	0.00158453	0.000115244	0.525	0.1
7 (1)	0.0017854	1.03E-04	0.520	0.1
8 (1)	0.0019319	1.03E-04	0.590	0.1
10 (1)	0.00220065	7.24E-05	0.560	0.0978723
MEAN:	**0.001557568**	**9.22342E-05**	**0.512**	**0.09754889**

Burn 9 failed to properly ignite quick enough to develop full combustion, and so was purposely left off of the above tables. A clear dichotomy existed in the results between

the two test groups, half at high venturi inlet pressure of 305 psi and half at a lower pressure of 235 psi. This dichotomy was predicted and expected due to larger choking mass flow levels at higher injector pressure. All comparisons and averages were thus calculated across the pressure groups, which unfortunately effectively reduced the experimental sample sizes. Following the calculations of section 3.3, predicted thrust was matched to the load cell data by uniting mean O/F predictions to the pressure data, and altering the location of a normal shockwave until thrust values matched the load cell output. After applying the nozzle discharge correction, predicted bell nozzle performance outperformed the cone nozzle by an average factor of 102%, matching well with expectations from literature [3].

Chamber pressure reconstruction managed to push $\tau_{Tailoff}$ to within a factor of 10 of expected combustion chamber depressurization time, $\tau_{combustor}$, a marked improvement over pre-reconstruction time lag. The time delay inherent to the sensor, τ_{Sensor}, is expected to be nearly instantaneous for the conditions of these burns, the use of pressure reconstruction was warranted in attempting to more closely match predicted values for $\tau_{combustor}$.

The comparatively long motor configuration produced low O/F ratio burns. Even the greatest mean O/F burn (burn 6 with O/F = 1.1) was far below the desired stoichiometric point of 1.6. Consistent with the updated Marxman model of Whitmore and Merkley [30], the motor exhibited a negative O/F shift. The motor's length ensured combustion started with an O/F below the stoichiometric point, and would end up even more fuel-rich by the end of the burn. This low O/F had several effects, notably lowering combustion flame temperature, and producing a large percentage of sooty particulates in

the rocket plume. The fuel-rich behavior can be seen in the burn slideshow of Fig. 5.1.1.-5.1.2

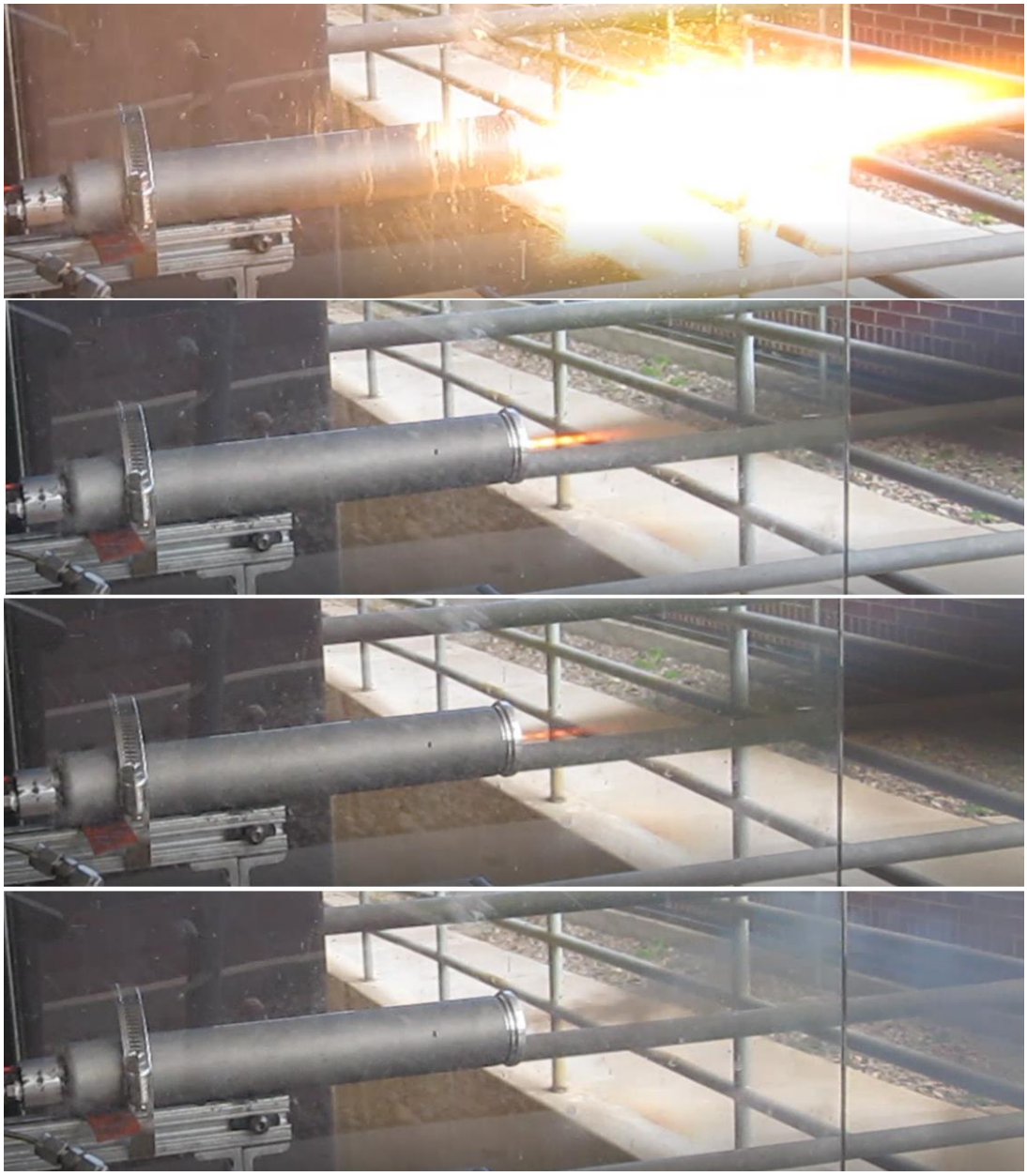

Figure 5.1.1. Cone nozzle time lapse, burn 1, *From top to bottom, a.) GOX ignition, b.) Steady state flow, shock diamonds formed, c.) End of steady state flow, plume noticeably fuel rich, d.) Motor Cutoff.*

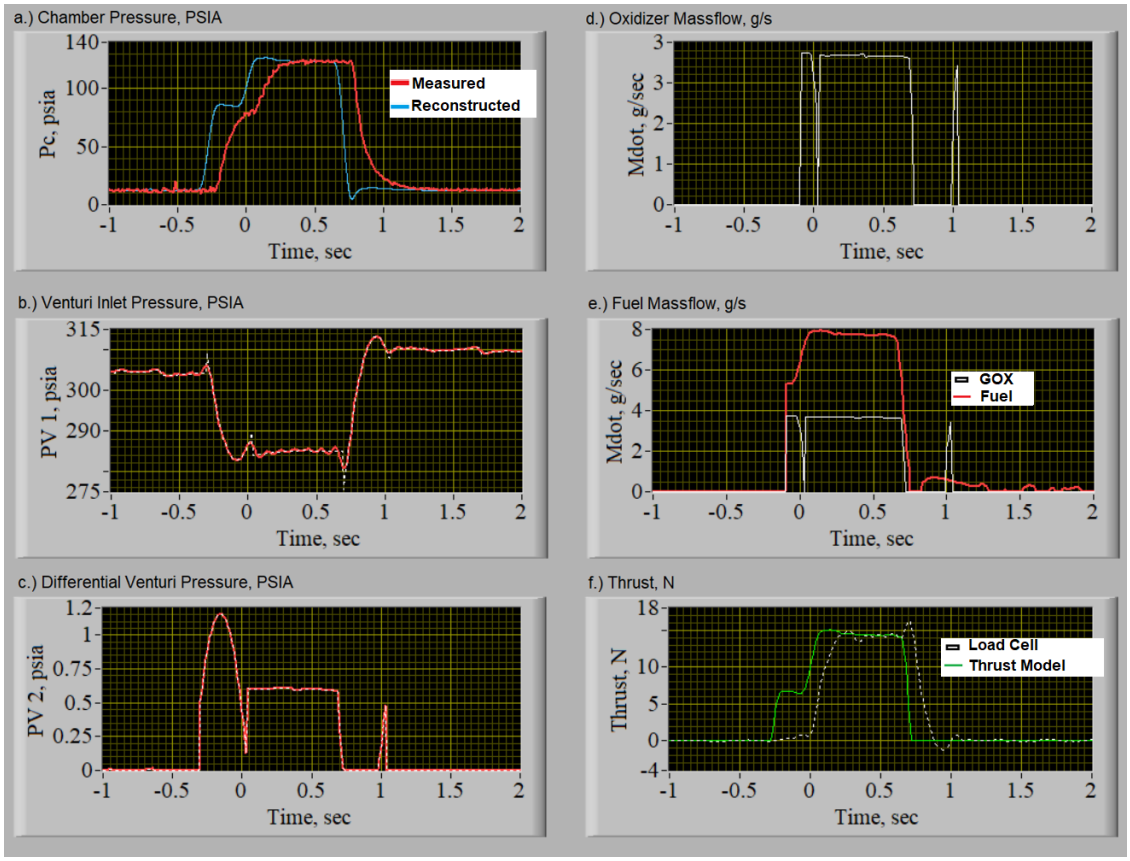

Figure 5.1.2. Cone nozzle time lapse, burn 1, *Corresponding Data.*

The cone nozzle burns showed noticeably poor I_{SP} performance, with previous configurations of the motor reporting significantly higher I_{SP}. This was largely due to the motor operating at low O/F ratio. When I_{SP} was plotted against mean O/F, as seen in Fig. 5.2, the motor is shown to have performed as expected, trending towards better performance towards the stoichiometric point. However, in comparison to previous USU testing at lower expansion ratios, the formation of over-expanded shockwaves altered performance. The existence of the shockwave was confirmed by rectifying the thrust recorded by the load cell with the shockwave model until good agreement was reached, and by visual indication of over-expanded shock diamonds in the flow. Clearly visible in the steady-state panels of Fig. 5.1.1, the train of formed shockwaves matches textbook

descriptions and model calculations indicate they would occur about ¾ of the way down the nozzle.

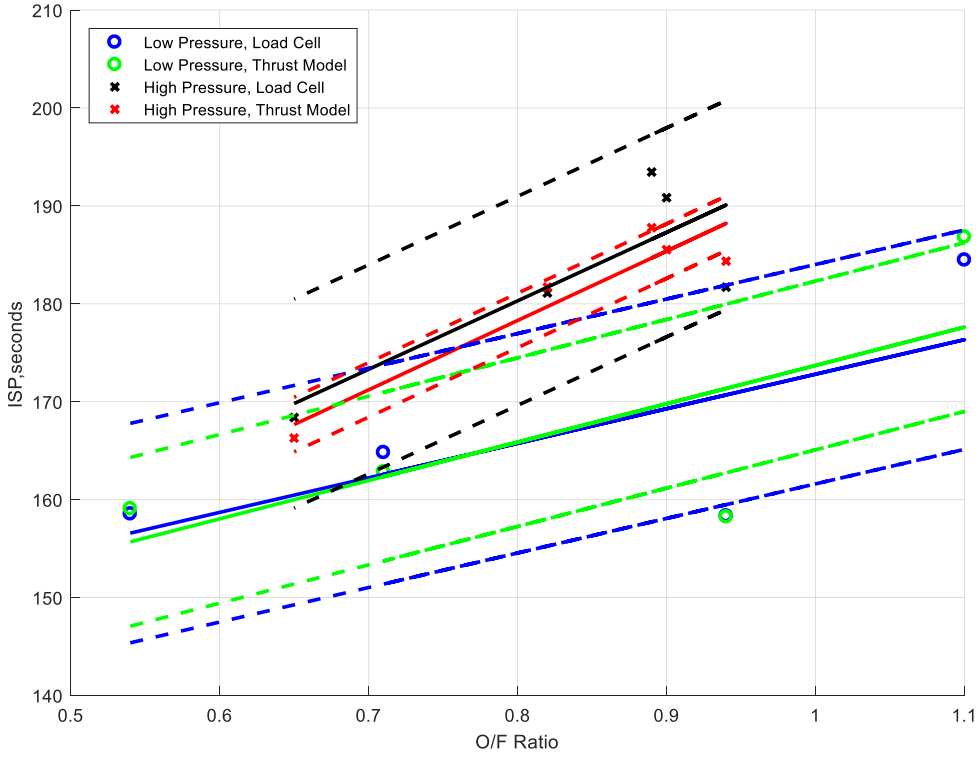

Figure 5.2. Cone nozzle specific impulse performance.

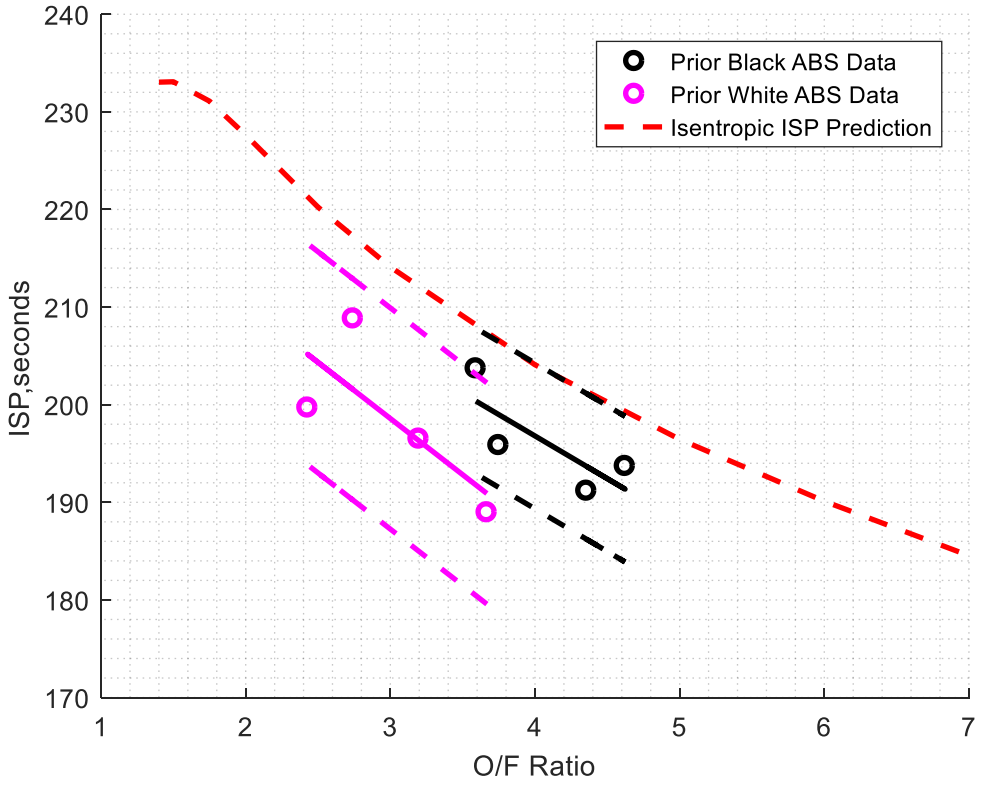

Figure 5.3. Comparative cone nozzle performance from previous studies. [29]

Previous low expansion ratio data from previous burns contrasts the low performance seen in Fig. 5.2 with the 8.5:1 cone nozzle. The 2:1 expansion ratio data produced by Whitmore and Peterson [29], shown above in Fig. 5.3, shows the expected trend towards superior performance closer to the stoichiometric point. This previous data lies upon the expected performance curve for the motor, following closely to an isentropic expansion calculation at the same chamber pressure. The cone data of this study appears to actually possess enhanced thrust and I_{SP} performance, in opposition to expected lower performance from over-expansion. This is seen in Fig 5.4. in an enhanced deviance between the cone burn data and an isentropic nozzle ideally expanded with no shockwaves.

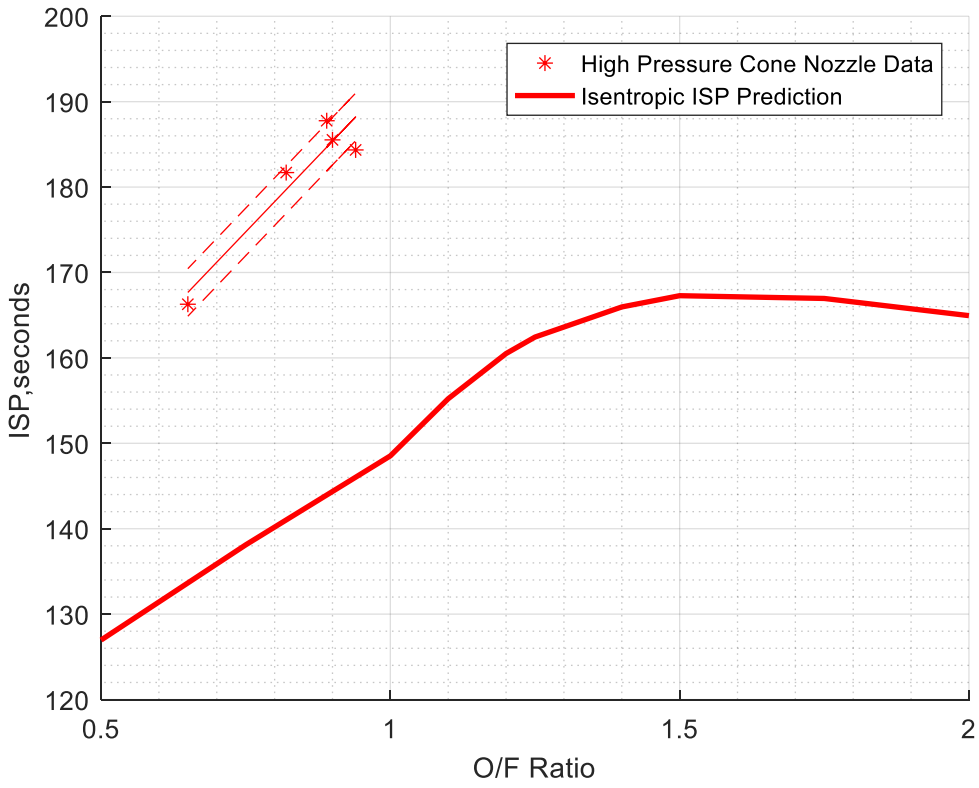

Figure 5.4. Unexpectedly enhanced over-expanded cone nozzle performance.

Pressure increase over a shockwave provides a possible explanation. In larger nozzles, flow separation occurs at a shockwave point due to a complex interaction with the boundary layer formed near the nozzle walls [1]. However, in a nozzle less than ¾ inch long, the boundary layer does not have the longitudinal space to form with any strength. Additionally, in general, cone nozzles are more resistant to flow separation than corresponding bell nozzles [3]. Without flow separation, a large percentage of nozzle performance losses no longer occur. Although momentum thrust is adversely affected by the presence of a shockwave, shockwaves have a large pressure increase across them, shown along a nozzle profile in Fig. 5.5. Increased pressure across the shockwave can result in a net gain in thrust by increasing pressure thrust.

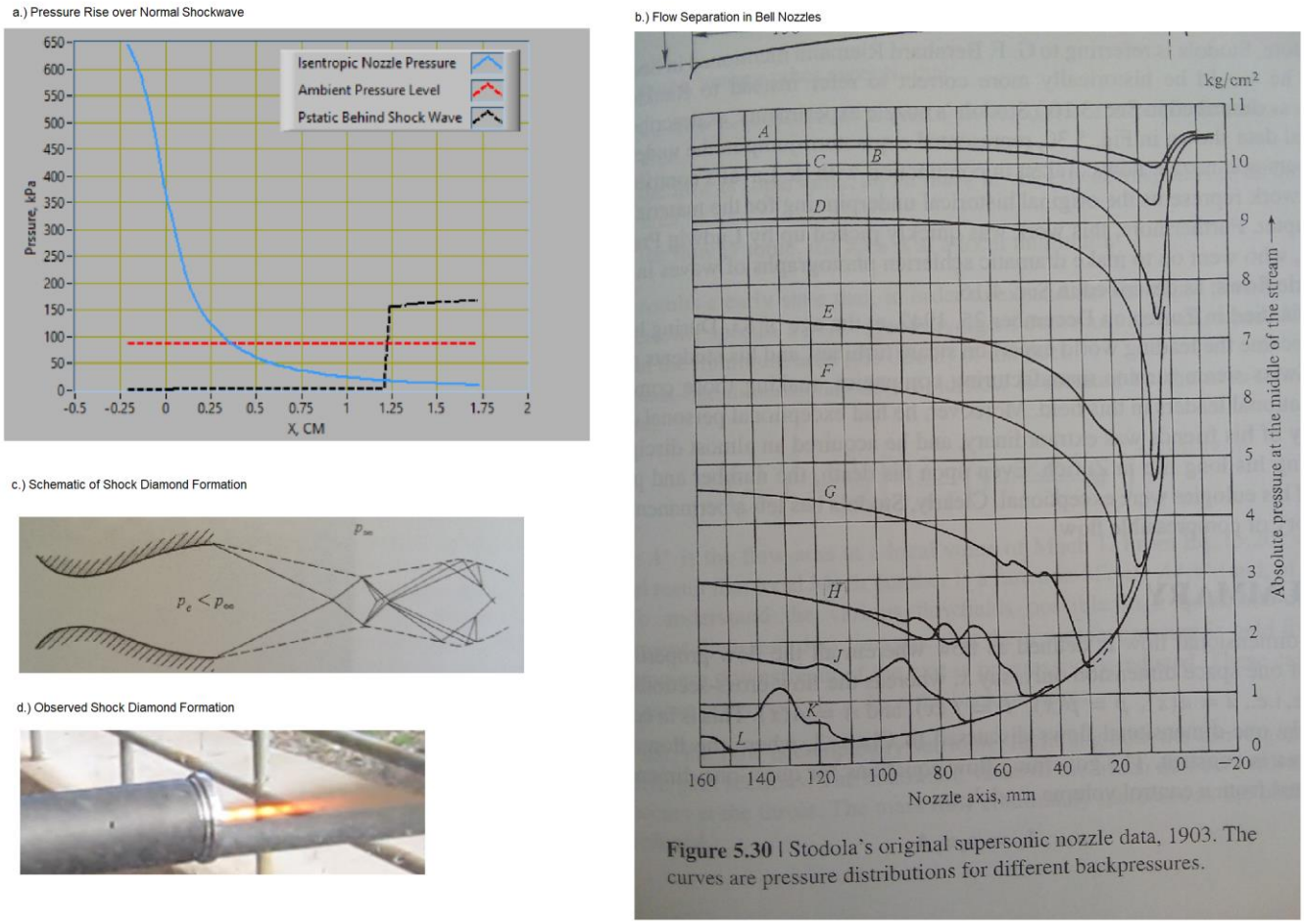

Figure 5.5. Shock wave behavior in bell nozzles. [1] *a.) Calculated static pressure rise over a normal shockwave, b.) Textbook figure describing nozzle flow separation, c.) Textbook schematic of shock diamond formation, d.) Hot fire test shock diamonds.*

Although no noticeable erosion took place in this nozzle, when scaled larger the thermal effects of an ingested shockwave can quickly become severe. The regular formation of a normal shockwave in this cone nozzle indicates that bell nozzles of the same 8.5:1 expansion ratio have reduced utility at this altitude and ambient pressure.

5.2 Over-Expanded Graphite Aerospike Tests (USU Campus, Logan, Utah)

A total of 10 tests were conducted with the 8.5:1 expansion ratio carbon graphite

aerospike machined at USU. A data corruption failure prevented the inclusion of burn 20 on the following results tables. Matching the geometry parameters of the cone nozzle, the aerospike was expected to operate in the over-expanded regime, forming a train of weak oblique shockwaves. The 10 burns were set to the same pressure levels as the cone burns, although exact precision was difficult to achieve due to regulator drift in HOR-3. The summary of the carbon aerospike burns, which took place between May 11th and 14th, 2018, is shown in Table 5.4, with a student-t distribution calculated to a 95% confidence interval. Table 5.5 presents the calculated performance parameters. Several time constants were calculated for each burn to justify reconstruction of the chamber pressure, as summarized in Table 5.6.

TABLE 5.4. Summary of Logan Aerospike Nozzle Test Parameters.

BURN # (Grain #)	Initial Fuel Port Diameter, in. (Final)	Burn time, s	Injector Pf, psia	Chamber P0, psia	Total Mass flow, g/s	Fuel Mass Burned, g	Combustion Efficiency	Mean O/F Ratio
11 (2)	0.311 (0.326)	0.8	310	123	4	3.34	0.91	1.19
12 (2)	0.326 (0.404)	0.94	310	136	4	4.26	0.88	0.865
13 (2)	0.404 (0.466)	0.95	317	135	4	4.22	0.88	1
14 (2)	0.466 (0.501)	0.87	308	132	4	3.38	0.87	1.25
15 (1)	0.501 (0.511)	0.91	307	132	4	3.14	0.91	1.2
16 (1)	0.511 (0.539)	0.85	233	105	3	3.63	0.86	0.78
17 (3)	0.231 (0.256)	0.79	235	98	3	2.62	0.82	1.2
18 (3)	0.256 (0.339)	0.87	243	99	3	3.13	0.95	0.85
19 (3)	0.339 (0.392)	1.08	235	99	3	3.64	0.83	0.68
High Pressure	**N/A**	**0.894 (0.055)**	**310.4 (3.498)**	**131.6 (4.587)**	**4 (0)**	**3.668 (0.474)**	**0.89 (0.017)**	**1.101 (0.145)**

MEAN: (Std. Dev.)								
High Pressure Student-T (95%)	**N/A**	**0.894 ±0.041**	**310.4 ±2.689**	**131.6 ±3.526**	**4 ±0**	**3.668 ±0.365**	**0.89 ±0.013**	**1.101 ±0.111**
Low Pressure MEAN: (Std. Dev.)	**N/A**	**0.898 (0.109)**	**236.5 (3.841)**	**100.25 (2.772)**	**3 (0)**	**3.255 (0.421)**	**0.87 (0.051)**	**0.878 (0.195)**
Low Pressure Student-T (95%)	**N/A**	**0.898 ±0.084**	**236.5 ±2.952**	**100.25 ±2.131**	**3 ±0**	**3.255 ±0.323**	**0.87 ±0.039**	**0.878 ±0.150**

Table 5.5. Performance Parameters for Logan Aerospike Nozzle Tests.

BURN # (Grain #)	**Load Cell Thrust, N**	**Steady State ISP, seconds**
11 (2)	13.3	161
12 (2)	14.0	150.5
13 (2)	14.0	160.5
14 (2)	13.8	160.95
15 (1)	12.8	154.0755
16 (1)	9.8	124
17 (3)	9.3	135.286
18 (3)	9.5	144.061
19 (3)	9.8	131.5
High Pressure MEAN: (Std. Dev.)	**13.6 (0.466)**	**157.4 (4.332)**
High Pressure Student-T (95%)	**13.6 ±0.359**	**157.4 ±3.330**
Low Pressure MEAN: (Std. Dev.)	**9.6 (0.212)**	**133.7 (7.224)**
Low Pressure Student-T (95%)	**9.6 ±0.163**	**133.7 ±5.553**

Table 5.6. Time Lag Comparison for Logan Aerospike Nozzle Tests.

BURN # (Grain #)	$\tau_{combustor}$, **seconds**	τ_{Sensor}, **seconds**	**Time Lag, seconds**	$\tau_{Tailoff}$, **seconds**

			(Pre-reconstruction)	(Post-reconstruction)
11 (2)	0.00106646	8.48E-05	0.60	0.093458
12 (2)	0.00146176	7.61E-05	0.60	0.111111
13 (2)	0.00182355	7.91E-05	0.68	0.096774
14 (2)	0.00221765	8.43E-05	0.70	0.108434
15 (1)	0.00239122	8.03E-05	0.70	0.096774
16 (1)	0.00259586	9.62E-05	0.70	0.102941
17 (3)	0.000550773	0.000117216	0.70	0.102941
18 (3)	0.00105435	9.84E-05	0.80	0.102941
19 (3)	0.00151587	9.54E-05	0.80	0.102941
MEAN:	**0.001610671**	**9.13512E-05**	**0.70**	**0.102126**

Similar to the conical burns, a clear separation existed between the high injector pressure and low injector pressure burns. Visual observation of a chain of oblique shockwaves confirmed over-expanded behavior, and prevented application of the aerospike thrust model of section 3.4. Thrust and I_{SP} calculations were therefore completely based on load cells measurements. Overall, the aerospike trended as expected on the O/F curve, and matched closely to isentropic I_{SP} predictions. Fig. 5.6.1-5.6.2 shows a burn slideshow of a representative carbon aerospike burn. Fig. 5.7 shows the I_{SP} results for the high pressure and low pressure test groups, and Fig. 5.8 shows the high pressure I_{SP} compared to the conical burns.

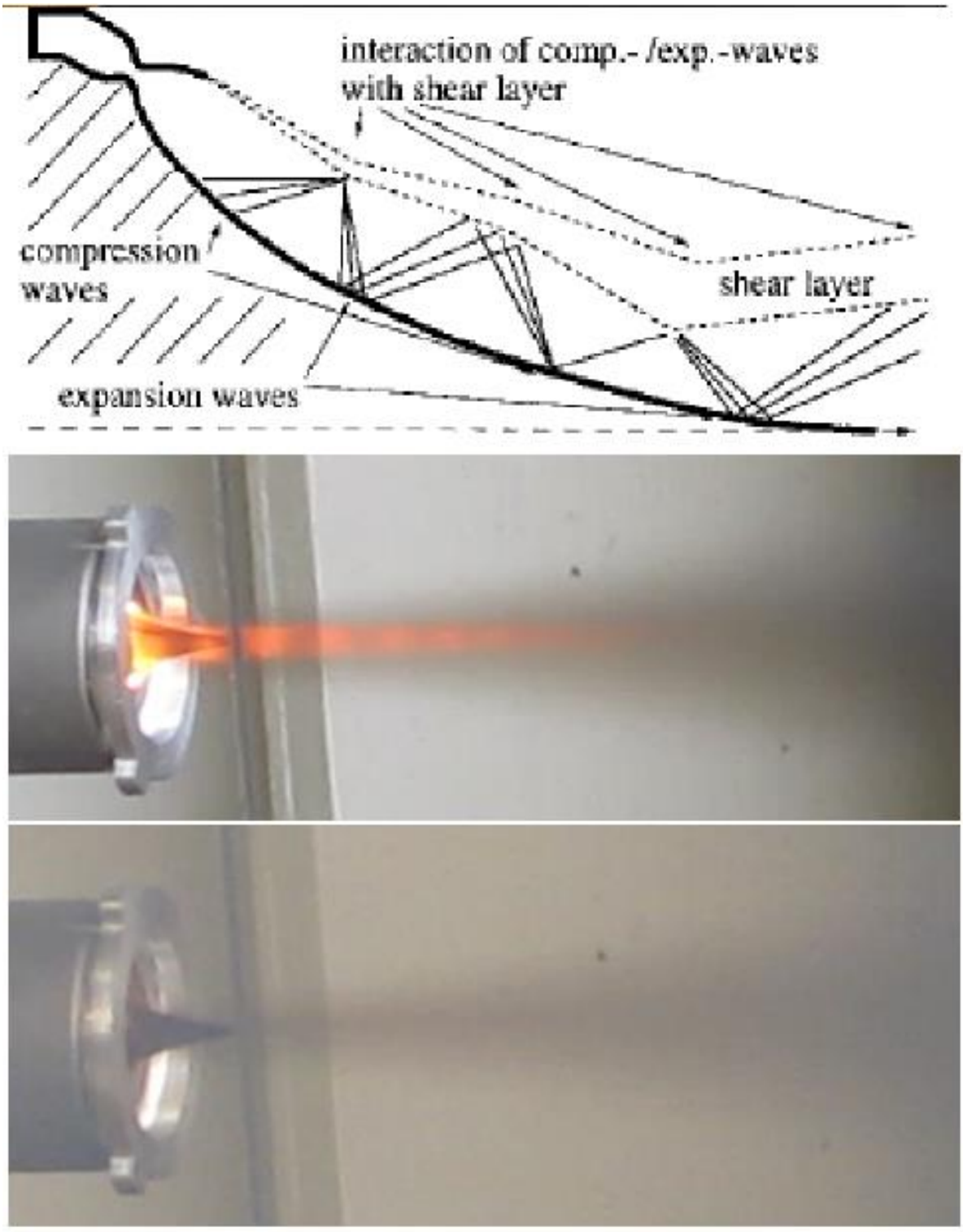

Figure 5.6.1. Carbon aerospike time lapse, burn 11. [3]**,** *From top to bottom, a.) Schematic of over-expanded aerospike shock train, b.) Over-expanded steady state flow, c.) Motor cut-off, fuel-rich plume still visible.*

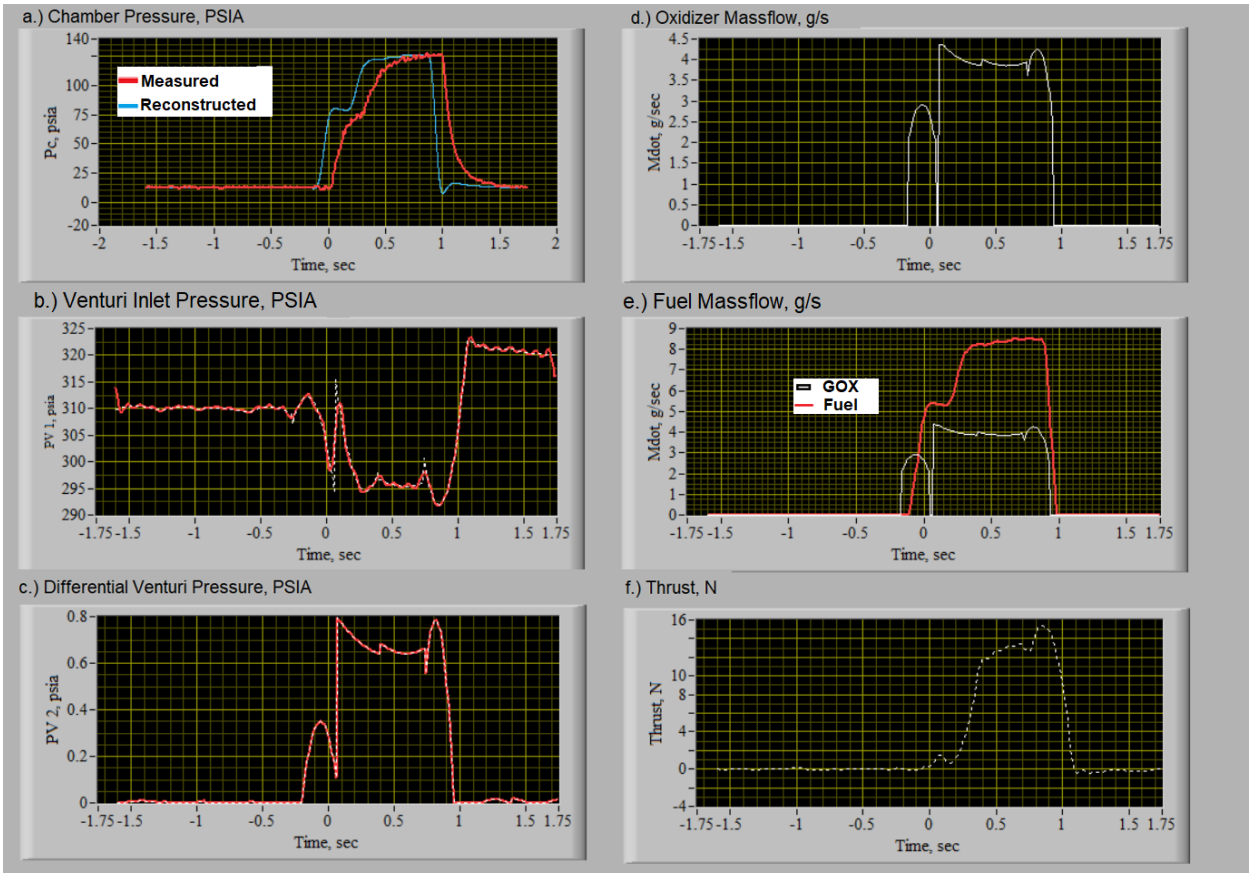

Figure 5.6.2. Carbon aerospike time lapse, burn 11, *Corresponding Data*

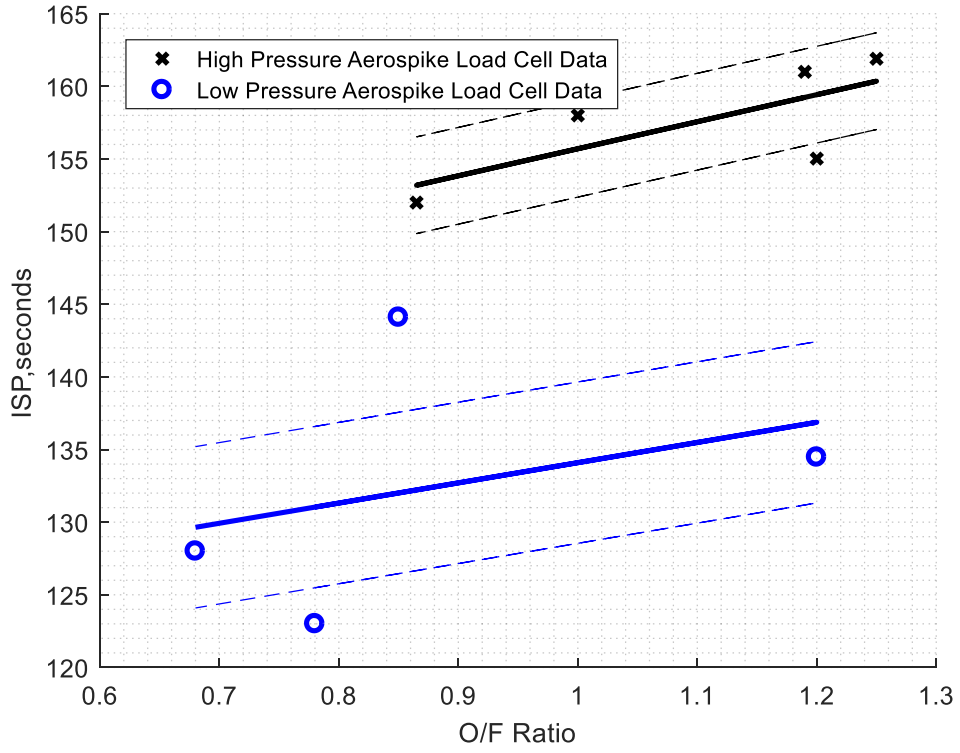

Figure 5.7. Carbon aerospike specific impulse performance.

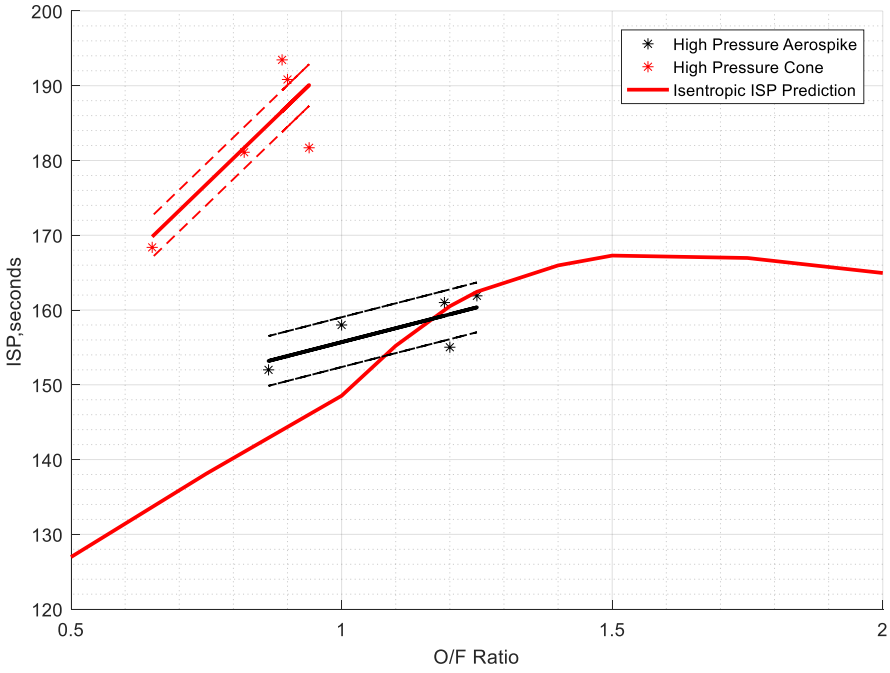

Figure 5.8. Over-expanded performance comparison between cone and aerospike tests.

Fig. 5.8 indicates that better I_{SP} performance was generated by the cone nozzle when compared to the aerospike, contrary to expectations from literature. However, previous studies were using larger nozzles, which correspondingly suffered more from flow separation than the ½" exit area cone nozzle used here. Fig. 5.8 also shows that the carbon aerospike performed much as it should have, and was a fully functioning nozzle despite being quite over-expanded. Previous work indicates that the over-expanded train of shockwaves present on an aerospike are far less thermally damaging than the strong normal shocks generated in a cone nozzle. Although neither the cone or aerospike nozzles showed damage along the nozzle contour, it is highly likely that longer burn times would have seen degradation in the conical nozzle.

Due to the thin geometry of the aerospike nozzle throat, degradation was difficult to track. Physical measurements were attempted, but did not possess low enough tolerances in the measurement error to be particularly useful. Even a small percentage change in the nozzle throat could have significantly reduced performance, but is difficult to approximate and so the effective reduction in expansion ratio was left off of the above charts. The final state of the carbon spike is shown in Fig. 5.9; with an intact spike contour but possibly degraded throat.

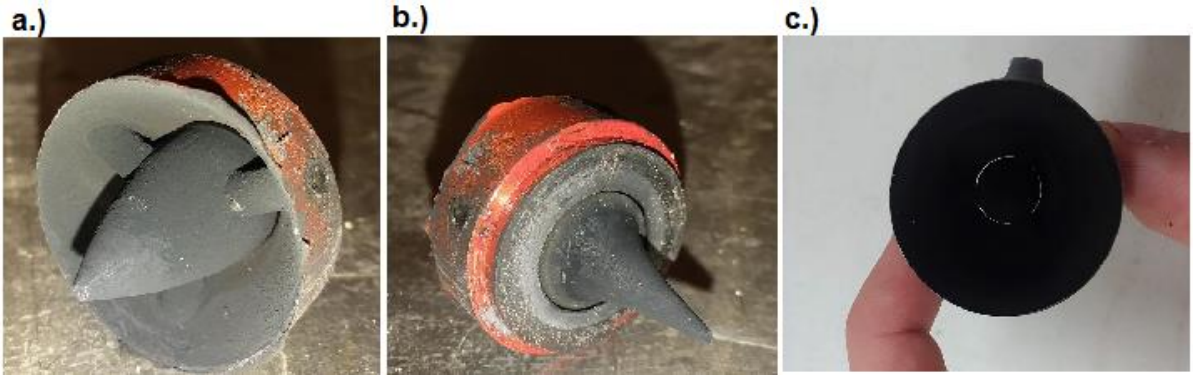

Figure 5.9. Final intact condition of carbon aerospike. *a.) Post-testing Haack profile, b.) Post-testing spike profile, c.) Post-testing nozzle throat.*

5.3 Under-Expanded Additively Manufactured Inconel Aerospike Tests (ER23, NASA MSFC, Huntsville, Alabama)

A total of 7 tests were conducted with the 8.5:1 expansion ratio 3D printed Inconel 718 aerospike. Although geometry parameters matched the other cone and aerospike nozzle, the printed nozzle's supporting struts were of smaller size in comparison to the carbon aerospike. At vacuum pressures of around 0.28 psi, the 8.5 expansion ratio was highly under-expanded. The aerospike thrust model of section 3.4 is applicable to under-expanded flow, and was used to reinforce the load cell readings. The load cell reading suffered from accelerated heating, as the small volume of the vacuum chamber reflected and retained radiative heat at a far larger rate. The load cell would heat mid burn, adding a hysteresis effect to the measurement. Fig. 5.10 shows the heat-skewed load cell measurement of burn 22, where the force measurement fails to return to the baseline pre-burn zero force reading. As such, greater stock was put into the chamber pressure measurement predicting thrust through the aerospike model, and reported values are taken from calculated model predictions.

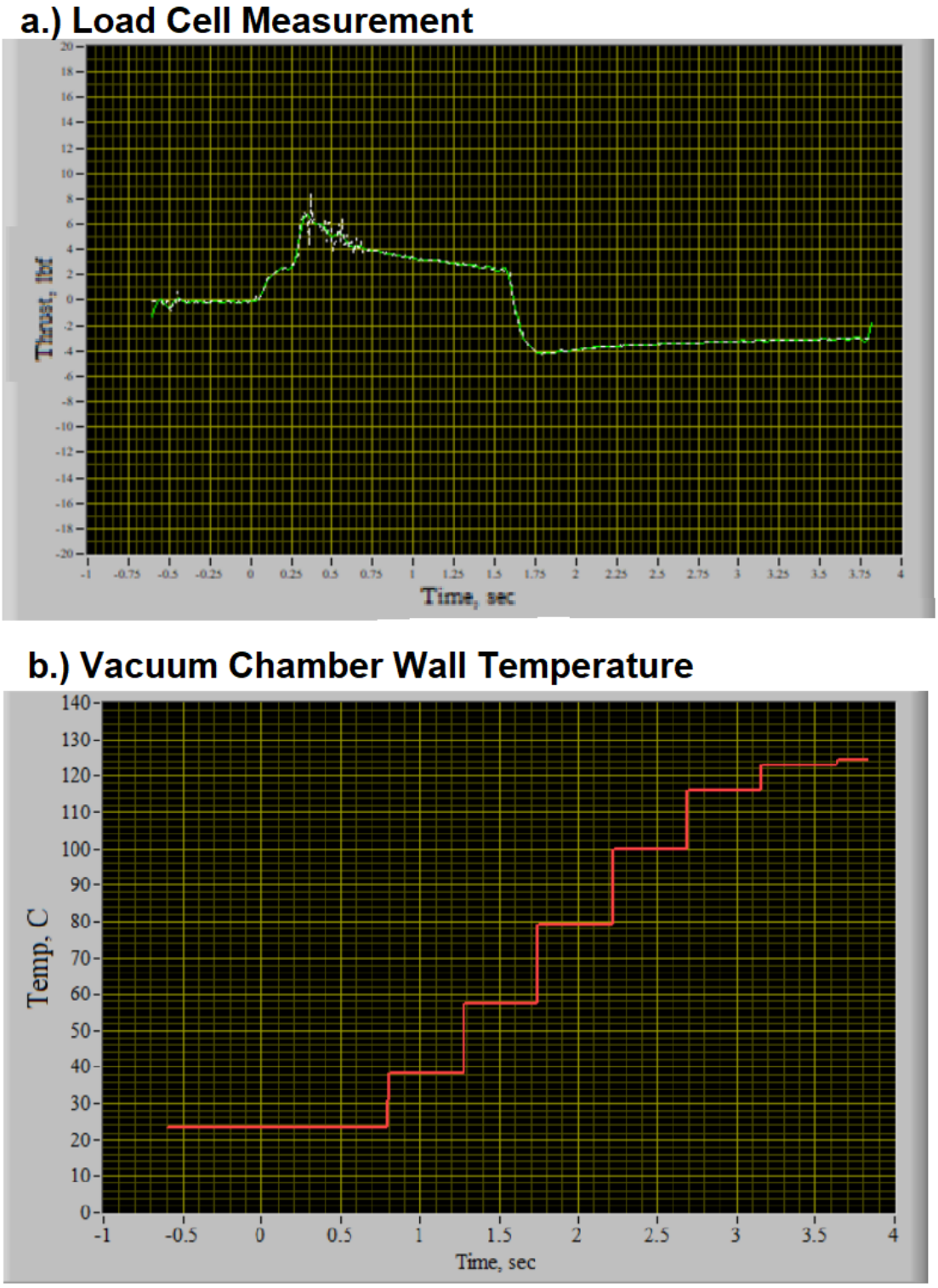

Figure 5.10. Thermal skewing of load cell measurement. *a.) Load cell measurement, thermally skewed over the course of 1.5 s test burn, b.) accompanying nearby thermocouple measurements.*

The vacuum chamber test facility necessitated several other changes to the test proceedings and analysis. Venturi inlet regulator creep induced a wider spread in venturi inlet pressure in comparison to the Logan burns; averages were therefore calculated over the entire set. Exact knowledge of the chamber pressure sensor geometry was not obtained during testing; unfortunately, this prevented later calculation of the sensor time lag, $\boldsymbol{\tau_{Sensor}}$. For consistency, and due to the similarity of the pneumatic tubing setup at NASA MSFC, the chamber pressure reconstruction was applied to these burns as well. To ensure steady state data, burn length was extended to 1.5 seconds after the first burn. The summary of the Inconel aerospike burns, which took place between August 6-8, 2018, is shown in Table 5.7, with a student-t distribution calculated to a 95% confidence interval. Table 5.8 shows the calculated performance parameters.

TABLE 5.7. Summary of Vacuum Aerospike Nozzle Test Parameters.

BURN # (Grain #)	Initial Fuel Port Diameter, in. (Final)	Burn time, s	Injector Pf, psia	Chamber P0, psia	Total Mass flow, g/s	Fuel Mass Burned, g	Combustion Efficiency	Mean O/F Ratio
21 (3)	0.466 (0.518)	0.81	300	235	6.00	2.4	0.99	1.45
22 (3)	0.518 (0.550)	1.70	250	146	5.75	4.5	0.99	2.40
23 (3)	0.550 (0.578)	1.56	250	166	5.75	4.95	0.95	1.40
24 (4)	0.345 (0.378)	1.57	227	165	5.00	4.45	0.99	1.20
25 (4)	0.378 (0.418)	1.53	225	136	5.50	4.38	0.86	1.68
26 (4)	0.418 (0.45)	1.60	223	208	4.00	4.87	0.99	0.40
MEAN: (Std. Dev.)	**N/A**	**1.47 (0.296)**	**245 (26.705)**	**176 (34.704)**	**5.33 (0.672)**	**4.26 (0.858)**	**0.97 (0.048)**	**1.42 (0.59)**
Student-T (95%)	**N/A**	**1.47 ±0.311**	**245 ±28.029**	**176 ±36.425**	**5.33 ±0.705**	**4.26 ±0.900**	**0.97 ±0.050**	**1.42 ±0.624**

Table 5.8. Performance Parameters for Vacuum Aerospike Nozzle Tests.

BURN # (Grain #)	Aerospike Model Thrust, N	Steady State ISP, seconds
21 (3)	42.0	321.1
22 (3)	26.5	307.2
23 (3)	30.0	304.0
24 (4)	29	311.8
25 (4)	25	274.0
26 (4)	35	247.1
MEAN: (Std. Dev.)	**31.3 (5.742)**	**294.2 (25.576)**
Student-T (95%)	**31.3 ±6.028**	**294.2 ±26.845**

Thermal degradation was initially noticed on burn 26, with complete thermal failure of the Inconel aerospike occurring on burn 27. This failure event is shown in Fig 5.11, and was potentially induced, or further induced, by a fundamental hardware change between burns 26 and 27. Wishing to drive O/F ratio higher to a leaner configuration, the motor case was swapped to a motor case half the longitudinal length of the original. Inspection of Eq. (3.7) illuminates this rationale, as motor length, L, is one of the easiest parameters to change on the fly. Most of the NASA burns, specifically burns 21-25, had exhibited lean behavior, but burn 26 had a low O/F ratio of 0.4. The experiment to drive the O/F ratio back to a leaner configuration was successful, but flame temperature also rises with proximity to stoichiometric combustion. Longer burn times were likely already weakening the Inconel aerospike, with stagnation erosion beginning to appear as early as burn 25. The aerospike ultimately failed at one of the support structures, a point of flow stagnation and proportionally small shear area.

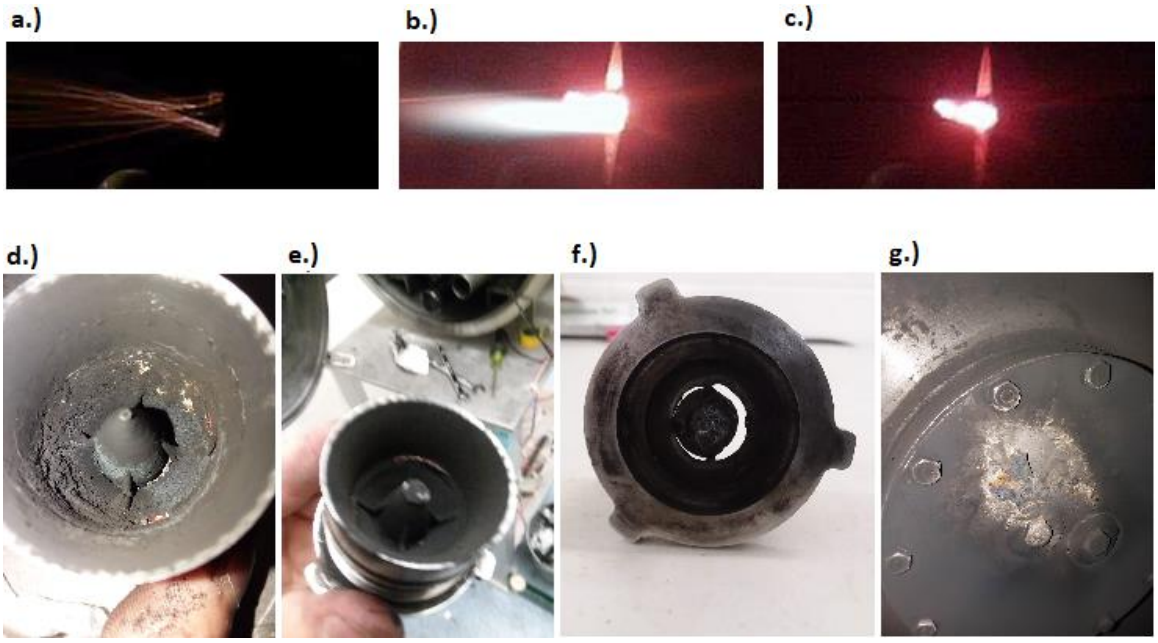

Figure 5.11. Thermal failure of Inconel aerospike. *a.) Burn 27 motor start-up, b.) Failure of support arm releases flow on one side, c.) Nozzle remnant glows white-hot even after motor cut-off, d.) State of nozzle after burn 25, e.) State of nozzle after burn 26, f.) State of nozzle after burn 27, g.) Molten Inconel residue on vacuum chamber wall.*

Prior to degradation, however, the vacuum aerospike tests were encouraging. High I_{SP} performance was reported from the aerospike thrust model. The load cell measurements were on average higher than the corresponding model predictions, but was suffering from thermal hysteresis and so was not considered completely valid. Load cell measurements were therefore used only as a feasibility check on the model predictions. Fig. 5.12 shows a sample data set from the Inconel aerospike burn 21, showcasing the reliability of the thrust model prediction over the skewed load cell measurement. Fig. 5.13 shows the I_{SP} comparison between load cell values and thrust model predictions, which have a wider deviance than the USU test data results.

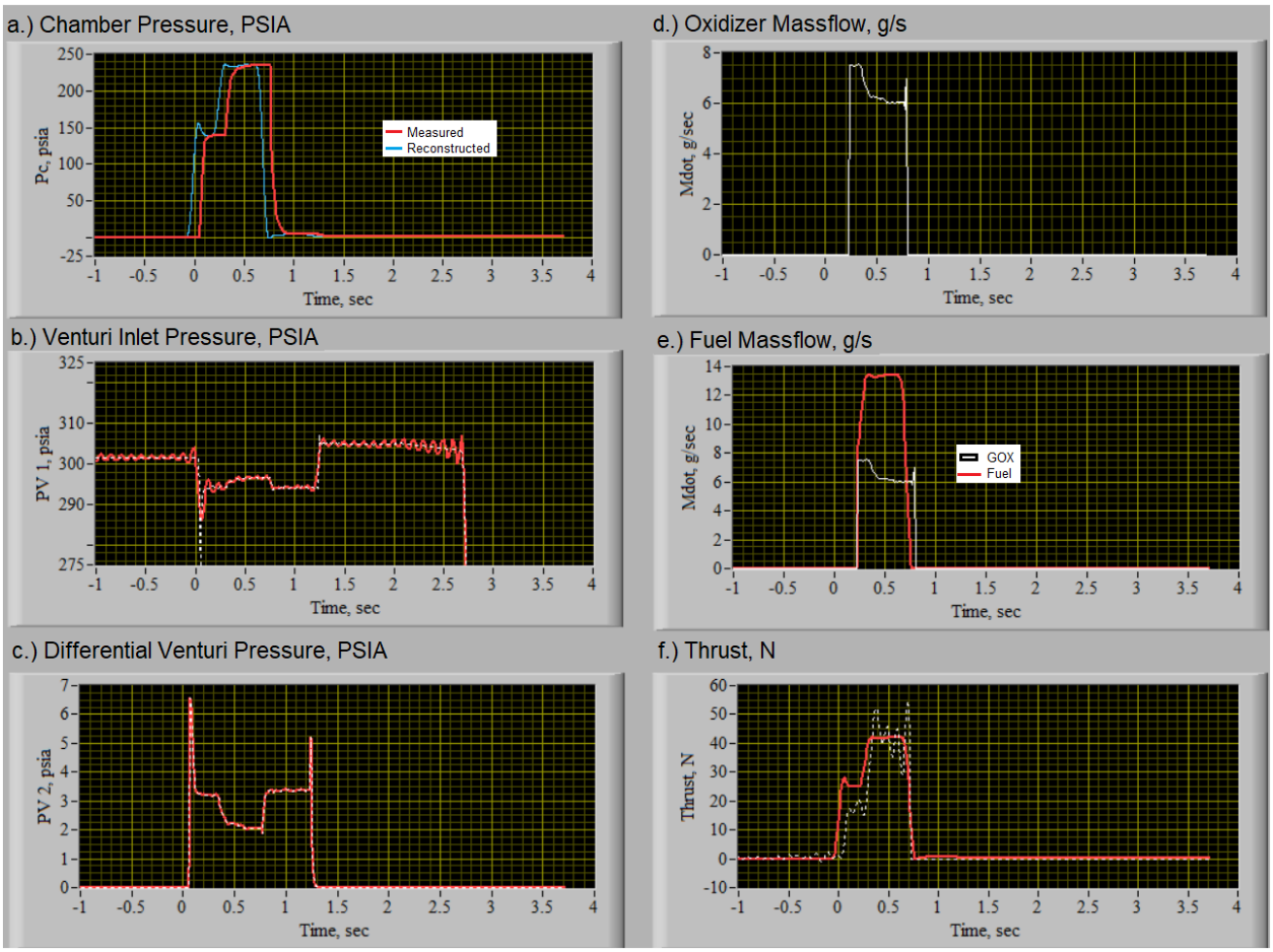

Figure 5.12. Burn 21 test data.

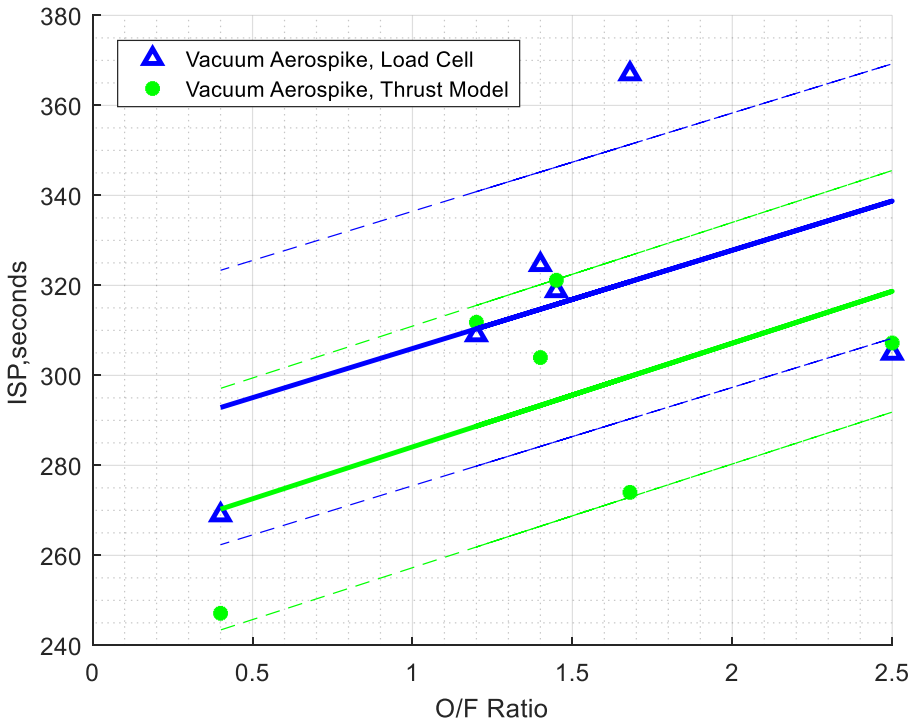

Figure 5.13. Inconel aerospike specific impulse performance.

Previous vacuum data for the propellants was available for comparison, and had shown a marked improvement by increasing expansion ratio, as seen in Fig. 5.14: [31]

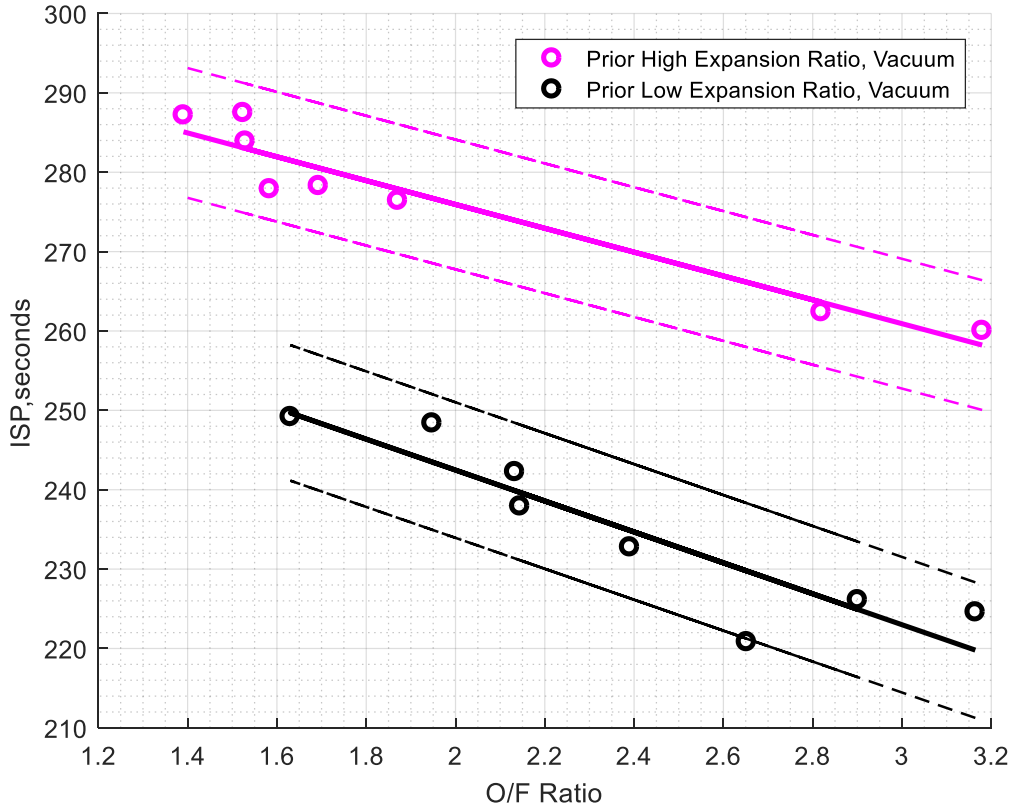

Figure 5.14. Comparison vacuum data from previous studies. [31]

Having been burned in lean configuration, the data sets of Fig. 5.14 show higher I_{SP} at smaller O/F ratios in an expected trend. Being in vacuum, the higher expansion ratio nozzle performs better than the 2:1 low expansion nozzle optimized for the back pressure of Logan, UT. When compared to the aerospike, however, the previous high expansion conical burns follow an I_{SP} curve lower than the aerospike results. Figure 5.15 shows this comparison, and with the exception of burn 25, lie on an I_{SP} curve roughly 15 seconds above the I_{SP} of the cone nozzle of the same geometry. The correction to full bell contour, a factor of about 102% from the Logan tests and from literature, is not sufficient to make up for this I_{SP} discrepancy. The aerospike nozzle provided an automatic adjustment in the vacuum conditions, enlarging the effective expansion ratio by natural

widening of the fluid boundary.

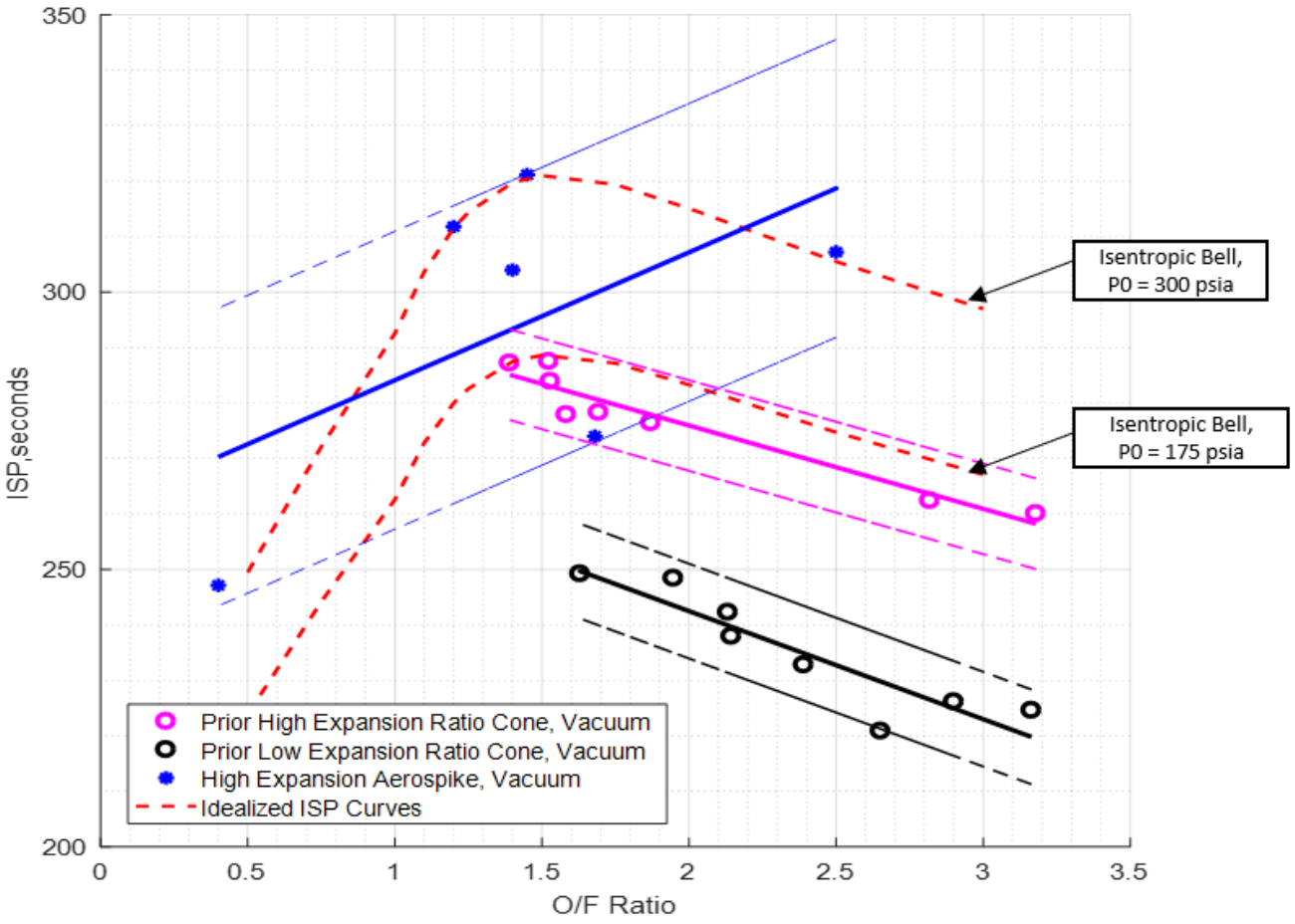

Figure 5.15. Under-expanded performance comparison between cone and aerospike vacuum tests.

CHAPTER VI
CONCLUSIONS AND FUTURE WORK

Aerospike nozzles, an old design from the 1960's, have been revisited at a small scale where the benefits of modern 3D-printing technology can be brought to bear. A need exists for small, cheap, and reliable propulsion systems to propel small satellites below the NanoSat size of 10kg. In particular, the rise in popularity of CubeSats is flooding orbits with small spacecraft, many of which rely on reaction wheels for limited maneuvering capabilities. Chemical rockets, used to propel many existing spacecraft, see proportionally large gains from small gains in nozzle performance. Aerospike nozzles provide two major advantages of interest over existing state-of-the-art bell nozzles. First, they have superior over-expanded performance that does not lead to normal shockwaves that plague bell nozzles. Second, for in-space vacuum conditions, aerospikes have the potential to be lighter and shorter than bell nozzles with corresponding throat area, exit area, and expansion ratio. Previous aerospike testing in literature was performed at a larger scale using conventional fabrication methods. Widespread aerospike hot fire data is limited due to low technological readiness; additionally, thermal degradation of aerospike nozzle throats remains a primary issue of concern that limits their utility. USU's ABS/GOX hybrid rocket research facilities provided a ready platform to integrate and test the proposed small aerospike nozzles, which were designed into an existing small-satellite sized system.

Two 8.5:1 expansion ratio aerospike nozzles were tested during the course of this thesis testing. To demonstrate the aerospike's enhanced performance abilities in both the over-expanded and under-expanded pressure regimes of nozzle flow, the aerospikes were tested against corresponding cone nozzles of the same geometric parameters. Cone

nozzles perform to within 98% of state-of-the-art bell nozzle performance, and previous studies at USU provided comparison vacuum data [31]. In order to completely contrast the aerospike results, an 8.5:1 expansion ratio cone nozzle was fabricated and tested at the USU main Logan, UT campus. Coupled with the aerospike testing, this testing completed a testing matrix that contrasted similar geometry cone and aerospike nozzles at both under-expanded and over-expanded pressure regimes. A cooperative agreement with NASA Marshall Space Flight Center allowed printing of a 1-piece aerospike nozzle out of Inconel 718 superalloy. Over-expanded aerospike testing was done using a multi-piece carbon graphite design using more conventional CNC machining at USU while the Inconel design was printing. The additively manufactured Inconel spike was expected to be more thermally resistant, but had minor changes added to ease printing manufacture that potentially weakened the structure by shrinking support columns that stagnate nozzle flow. The aerospike nozzle tests were theoretically hypothesized to exhibit superior I_{SP} performance at both pressure conditions, with hopefully negligible thermal degradation.

Results were interestingly mixed for the aerospike testing. In the comparatively high back pressure environment of Logan, UT at ~12.4 psia, the bell nozzle exceeded the comparative carbon aerospike in terms of raw I_{SP} performance when plotted against O/F ratio. However, cone nozzles can see a thrust increase at small size in the presence of shockwaves. Normal shocks are associated with a large rise in static pressure, which in larger nozzles leads to flow separation via complex interaction with formed nozzle boundary layers along the nozzle's walls. Small nozzles do not have the physical length required to form substantial boundary layers, including the cone nozzles of this study which were less than ¾ inches long. The increased I_{SP} of the cone nozzle is therefore

attributed to the formation of over-expanded shockwaves, which matched expectations from literature and were confirmed by application of a normal shock model and visual shock diamond indications [1].

While the over-expanded aerospike burns at USU did not exceed the I_{SP} performance of the corresponding cone nozzle burns, they did exhibit good performance that trended well with established isentropic nozzle expansion models. Visual indication of a weak oblique shock train further confirmed the aerospike was performing as it was supposed to. Both carbon nozzles (cone and aerospike) survived ~10 seconds of test burn time with minimal thermal degradation. Presence of the normal shockwave in the cone nozzle indicates thermal degradation could likely affect cone nozzles of this expansion ratio at Logan, UT back pressure levels, especially when scaled larger.

Under-expanded in-vacuum aerospike testing at NASA MSFC, utilizing the additively manufactured Inconel aerospike, saw superior I_{SP} performance. Results indicate an average increase in I_{SP} of around 10-15 seconds is possible by switching from a bell nozzle to a similarly designed aerospike nozzle, which could potentially translate to significant fuel weight and volume savings. However, the experimental sample size was prematurely cut short due to thermal destruction of the Inconel aerospike, exacerbated by an hardware change halfway through testing. Thermal degradation had already been witnessed in the preceding burn so it is conjectured that the Inconel aerospike would have failed in the near future regardless. The mechanism of failure was by shearing of a cantilevered support arm, a point of stagnation that was comparatively smaller than the intact carbon aerospike tested at USU.

Despite shortcomings, the aerospike results are promising in I_{SP} performance and

provide physical evidence of their famed ability to compensate with altitude. Over-expanded testing saw the aerospike form a chain of oblique shocks that kept performance close to idealized nozzle expansion. In vacuum, where optimal expansion ratio becomes infinite, the aerospike acted like a nozzle of far larger expansion ratio than had physically been constructed, with an associated gain in I_{SP} preliminarily assessed to be ~6%. Survival of the carbon aerospike over a cumulative burn time of over 8 seconds indicates survival over mission lifetime may be feasible, particularly in application where short, 1 second, pulses are applicable. 3D printing enables quick design and integration of new nozzles, and with sufficient research could be easily engineered into existing chemical propulsion systems at a small scale. The M290 printer proved fully capable of producing the tiny tolerances required by the aerospike nozzle throat without closures.

Several interesting avenues for future research have opened up over the course of this research. First, further data to increase experimental sample sizes at this scale of 0.5 inches exit diameter is needed to reinforce the initial claims of this data. Experimental tests to determine the true thermal limits of this size of aerospike nozzle throat by testing to destruction in order to prove their practical application. Production of several identical-within-tolerance test articles is easier than ever with 3D metal printing, a technology being driven daily to tighter and tighter tolerances by enormous industry demand.

Several of the materials choices used for this study were driven by necessity rather than optimization, and provide a natural point of improvement for future work. First, tungsten printing capability has increased dramatically in the last few years and with the highest known melting point of metals is a logical choice for aerospike manufacture. A printed tungsten aerospike, incorporating the lessons learned with small

support structures from this study's Inconel aerospike, could in practice become much more resilient to thermal degradation. Additionally, the thermal problems of this study were further exacerbated by the use of ABS/GOX propellants, which under stoichiometric conditions possesses a flame temperature of nearly 3800 K, which burns significantly hotter than several other common propellants. [29] Hydrazine, one of the most commonly utilized liquid monopropellants, has a significantly cooler flame temperature of ~1100 K, and an additively manufactured aerospike nozzle could be significantly more robust when integrated into a system utilizing other propellants. [3]

Development of a higher fidelity thermal model, potentially utilizing CFD techniques as others have done in literature, to predict thermal failure also seems like a natural course of action. Ultimately, more experimental data could realistically bring the aerospike out of the realm of novelty into real-world feasibility.

As a noteworthy aside, the pressure deconvolution method of Whitmore and Fox [35], was validated by the time constant studies of this testing campaign. It is highly recommended that future testing at USU at least be aware of the time latency issue encountered by this study when using similar instrumentation. Thorough cleaning of transducer line filters and off transducer volumes themselves could prevent soot buildup, presumably reducing the pressure latency. Discrepancies in measured fuel mass to hybrid model predictions, along with observed long motor tail-offs in chamber pressure measurements, can be a tip off to apply the deconvolution reconstruction to chamber pressure transducer measurements.

BIBLIOGRAPHY

[1] J. D. Anderson, Modern Compressible Flow, 3rd Edition, New York: The McGraw Hill Companies, Inc., 2003.

[2] W. Williamson, "Why is hydrogen and oxygen to water exothermic if it requires energy to start?," Quora, 9 December 2016. [Online]. Available: https://www.quora.com/Why-is-hydrogen-and-oxygen-to-water-exothermic-if-it-requires-energy-to-start.

[3] S. Whitmore, "Lecture Note Web Page," Utah State University MAE, August 2018. [Online]. Available: http://mae-nas.eng.usu.edu/SAW_NOTES_2018.html.

[4] G. P. Sutton and O. Biblarz, Rocket Propulsion Elements, 7th ed., New York: Wiley, 2001.

[5] N. T. Staff, "Space Transportation System HAER No.TX-116," NASA.

[6] K. Davidian, "The Aerospike Nozzle and Frequently Asked Questions List," NASA X-33 Project, December 1997. [Online].

[7] S. D. Eilers, "Development of the Multiple Use Plug Hybrid for Nanosats (Muphyn) Miniature Thruster," *All Graduate Theses and Dissertations,* vol. Paper 1726, 2013.

[8] T. Ladeinde and H. and Chen, "Performance Comparison of a Full-Length and a Truncated Aerospike Nozzle," *46th AIAA/ASME/SAE/ASEE Joint Propulsion Conference & Exhibit,* 2010.

[9] T. Biu, J. R. C. Murray, S. C. A. Bartel and M. Dennet, "Flight Research of an Aerospike Nozzle Using High Power Solid Rockets," *41st AIAA/ASME/SAE/ASEE Joint Propulsion Conference & Exhibit,* 2005.

[10] S. A. Whitmore, B. L. Chamberlain, I. W. Armstrong, S. Matthias and S. A. Fehlberg, "Consumable Spacecraft Structure with Integrated, 3-D Printed Acrylonitrile Butadiene Styrene (ABS) Thrusters," *53rd AIAA/ASME/SAE/ASEE Joint Propulsion Conference & Exhibit,* 2017.

[11] H. Lewis, B. Schwarz and S. a. S. H. George, "An Assessment of CubeSat Collision Risk," *65th International Astronautical Congress,* 2014.

[12] F. M. White, Viscous Fluid Flow, New York, New York: McGraw-Hill, Inc, 1991.

[13] B. Boen, "X-33 Advanced Technology Demonstrator," 12 April 2008. [Online]. Available: https://www.nasa.gov/centers/marshall/news/background/facts/x33.html.

[14] W. e. al., "Aerospike nozzle contour design and performance validation," *Acta Astronautica,* vol. 64, pp. 1264-1275, 2009.

[15] C. C. Lee and D. D. Thompson, "FORTRAN Program for Plug Nozzle Design," NASA TM X-53019, Huntsville, Alabama, 1964.

[16] G. Angelino, "Approximate method for Plug Nozzle Design," *AIAA Journal 2,* no. (10), 1964.

[17] E. Besnard and J. Garvey, "Aerospike engines for nanosat and small launch vehicles," *Space Conference and Exhibit,* 2004.

[18] M. T. M. S. T. T. K. K. a. H. T. Hiroshi Sakamoto, "An experimental study on a 14 kN linear aerospike-nozzle combustor," in *35th AIAA/ASME/SAE/ASEE Joint Propulsion Conference and Exhibit*, Los Angeles, California, 1999.

[19] S. Verma, "Performance Characteristics of an Annular Conical Aerospike Nozzle with Freestream Effect," *Journal of Propulsion and Power,* 2009.

[20] G. Swathi, C. S. Sandeep, M. Snigdha, G. Sravanthi and D. Govardhan, "Three Dimensional Computational Flow Simulation of Truncated Aerospike Nozzle Considering Different Plug Lengths," *Indian Journal of Science and Technology,* 2017.

[21] J. Ruf and P. McConnaughey, "The Plume Physics Behind Aerospike Nozzle Compensation and Slipstream Effect," *33rd AIAA/ASME/SAE/ASEE Joint Propulsion Conference & Exhibit,* 1997.

[22] T.-S. Wang, "Analysis of Linear Aersopike Plume-Induced X-33 Base-Heating Environment," *Journal of Spacecraft and Rockets,* vol. 36, no. No. 6, 1999.

[23] M. Karia, M. A. Popat and K. Sangani, "Selective Laser Melting of Inconel Super Alloy- A Review," *AIP Conference Proceedings,* 2017.

[24] EOS, "Datasheet EOS M290," EOS, September 2017. [Online]. Available: https://www.eos.info/eos-m290.

[25] J. S. M. N. J. Cesarano, "Robocasting, 3D printing of ceramics," Robocasting LLC, 2018. [Online]. Available: https://robocasting.com/index.php/about.

[26] D. Sher, "Purdue University's Zucrow Lab develops vibrating nozzle 3D printing process for highly viscous materials," 3D Printing Media Network, 14 June 2018. [Online]. Available: https://www.3dprintingmedia.network/purdue-university-highly-viscous-materials/.

[27] Corning, inc., "Macor Machinable Glass Ceramic for Industrial Applications," Corning, inc., 2018. [Online]. Available: https://www.corning.com/worldwide/en/products/advanced-optics/product-materials/specialty-glass-and-glass-ceramics/glass-ceramics/macor.html.

[28] J. H. Marshall, "Thrust Augmented Nozzle for a Hybrid Rocket with a Helical Fuel Port," Utah State University, Logan, Utah, 2017.

[29] Z. W. P. S. D. E. Stephen A. Whitmore, "Comparing Hydroxyl Terminated Polybutadiene and Acrylonitrile Butadiene Styrene as Hybrid Rocket Fuels," *Journal of Propulsion and Power,* vol. 29, no. 3, 2013.

[30] S. L. M. Stephen A. Whitmore, "Effects of Radiation Heating on Additively Printed Hybrid Fuel Grain O/F Shift," *AIAA/SAE/ASEE Joint Propulsion Conference,* 2016.

[31] S. L. Merkley, "Effects of Radiation Heating on Additively Printed Hybrid Fuel Grain Oxidizer-To-Fuel Ratio Shift," Utah State University, Logan, Utah, 2016.

[32] M. A. Bulcher, "Experimental Investigation of a Green Hybrid Thruster Using a ately Enriched Compressed Air as the Oxidizer," Utah State University, Logan, Utah, 2018.

[33] G. A. C. Sr., "The Descriptive Geometry of Nose Cones," 1996.

[34] M. D. W. S. D. E. Stephen A. Whitmore, "Novel Technique for Reconstructing High-Frequency Transient Rocket Chamber-Pressure Measurements," *Journal of Spacecraft and Rockets,* vol. 47, no. 3, 2010.

[35] S. A. W. a. B. Fox, "Improved Accuracy, Second-Order Response Model for Pressure Sensing Systems," *Journal of Aircraft,* vol. 46, no. 2, 2009.

[36] "Cesaroni Pro 38," Cesaroni Technology Inc., 2012. [Online]. Available: http://www.pro38.com/products/pro38/hardware_pro38.php.

[37] S. M. Stephen Whitmore, "Vacuum Test Measurements of Novel Green-Propellant Thruster for Small Spacecraft," USU, Logan, UT, 2016.